PASJ: Publ. Astron. Soc. Japan **60**, 1077–1131, 2008 October 25

Statistical Properties of Stellar H_2O Masers — Results of Three-Year Single-Dish Observations with the VERA Iriki Telescope

Motonobu SHINTANI,[1] Hiroshi IMAI,[1,2] Kazuma ANDO,[1] Kouichiro NAKASHIMA,[1] Tomoya HIROTA,[3] Noritomo INOMATA,[1] Takayuki KAI,[1,2] Seiji KAMENO,[1,2] Masachika KIJIMA,[3,5] Hideyuki KOBAYASHI,[3,5] Mina KUROKI,[1] Toshihisa MAEDA,[1] Kenta MARUYAMA,[1] Naoko MATSUMOTO,[1] Takeshi MIYAJI,[3] Takumi NAGAYAMA,[1] Riiko NAGAYOSHI,[2] Kayoko NAKAMURA,[1] Akiharu NAKAGAWA,[2] Daichi NAMIKAWA,[1] Toshihiro OMODAKA,[1,2] Tomoaki OYAMA,[3] Seiichiro SAKAKIBARA,[1] Rie SHIMIZU,[1] Kasumi SORA,[1] Miyuki TSUSHIMA,[1] Kosuke UEDA,[1] Yuya UEDA,[2] and Kazuyoshi YAMASHITA[3,5]

[1]*Graduate School of Science and Engineering, Kagoshima University, 1-21-35 Korimoto, Kagoshima 890-0065*
[2]*Department of Physics, Faculty of Science, Kagoshima University, 1-21-35 Korimoto, Kagoshima 890-0065*
[3]*Mizusawa VERA Observatory, National Astronomical Observatory of Japan, 2-12 Hoshigaoka, Mizusawa-Ku, Oshu-shi, Iwate 023-0861*
[4]*Space VLBI Project, National Astronomical Observatory of Japan, 2-21-1 Osawa, Mitaka, Tokyo 181-8588*
[5]*Graduate University for Advanced Studies, 2-21-1 Osawa, Mitaka, Tokyo 181-8588*
(HI) hiroimai@sci.kagoshima-u.ac.jp

(Received 2008 February 19; accepted 2008 May 10)

Abstract

We report on the results of monitoring observations of 242 stellar H_2O masers, which have been made with the Iriki 20 m telescope of the VLBI Exploration of Radio Astrometry (VERA) from 2003 July to 2006 November. The present paper mainly focuses on 85 stellar H_2O masers that have been tightly observed with a time spacing of typically 1–2 months. In particular, 46 masers out of them have been recognized concerning their periodic flux variation and have light-curve data of stellar visual light. Thus, the present paper shows some statistical views of the observed time variability properties of stellar H_2O masers. We found a good correlation between a time delay of the variation in the H_2O maser flux with respect to that in the stellar visual light and the stellar pulsation period. The corresponding phase lags are mildly scattered, but are mainly concentrated in the range, $0.7 \leq \Delta\phi \leq 1.5$. We also measured line-of-sight velocity drifts of the individual spectral peaks of H_2O maser emission, which indicate radial acceleration of mass-loss outflows from the evolved stars. We discuss possible pulsation-driven shock waves that are enhanced near the stellar surface, and are propagating outwards in the circumstellar envelope.

Key words: masers — stars: late type — stars: mass loss — stars: variables: other

1. Introduction

H_2O masers are seen in star-forming regions and around evolved stars (e.g., Reid & Moran 1981; Elitzur 1992a). Especially in the latter case, most of them are associated with the asymptotic giant branch (AGB) stars with copious mass loss ($\dot{M} \gtrsim 10^{-8} M_\odot\,\mathrm{yr}^{-1}$, e.g., Bowers & Johnston 1994), some of them also with the post-AGB stars in which their copious mass loss has just finished (e.g., Miranda et al. 2001). Such evolved stars have thick circumstellar envelopes (CSEs), and the spatio-kinematical structures of the outward flows in the CSEs have been elucidated through radio interferometric observations of H_2O masers (e.g., Chapman & Cohen 1986; Bowers et al. 1993; Bowers & Johnston 1994; Yates & Cohen 1994; Richards & Yates 1998; Bains et al. 2003). Even for a limited number of stellar H_2O maser sources, very long baseline interferometry (VLBI) observations with higher angular resolution can identify individual maser gas clumps, or maser features. Their relative proper motions have been measured, allowing us to elucidate the three-dimensional spatio-kinematical structures of the CSE flows (e.g., Marvel 1997; Ishitsuka et al. 2001; Imai et al. 2003). Except for a small number of extreme cases with highly collimated, fast stellar jets (e.g., Imai et al. 2002) or with bipolar flows seen in supergiants (e.g., Richards et al. 1996), the CSEs traced by H_2O maser emission exhibit roughly spherical expansion with velocity amplitudes in the range of 5–20 km s^{-1}. The velocity amplitudes are larger than those of SiO masers located closer to the central stars (e.g., Diamond & Kemball 2003), and slightly smaller than those of 1612 MHz OH masers located at the outer regions of CSEs (e.g., Chapman & Cohen 1986; Richards & Yates 1998; Sjouwerman et al. 2000). These suggest that the CSE flows are radially accelerated outwards in the H_2O maser regions (e.g., Bains et al. 2003).

Such AGB stars with H_2O masers are also long-period variable stars, such as Mira and semiregular variables. A periodic behavior of the CSEs is also well seen in the wide range of distances from the central stars, which is traced by all of the SiO, H_2O, and OH masers, and has been reported mainly in single-dish observations (e.g., Hjalmarson & Olofsson 1979; Lane 1982; Herman & Habing 1985; Nyman & Olofsson 1986; van Langevelde et al. 1990; Le Bertre 1993; Berulis et al. 1994; Mendoza-Torres et al. 1997; Berulis et al. 1998; Lekht et al. 1999; Alcolea et al. 1999; Esipov et al. 1999; Pashchenko & Rudnitskii 1999; Rudnitskii et al. 1999; Etoka et al. 2001; Pardo et al. 2004; Pashchenko & Rudnitskiĭ 2004; Rudnitskij

et al. 2000; Rudnitskiĭ & Pashchenko 2005; Lekht et al. 2005). Note that the periodic variation in H_2O masers is expected to be attributed to a periodic variation of the density and the velocity field of the CSE, not to that of the infrared stellar luminosity, as seen in the OH maser variation (see review of Elitzur 1992b). Shock waves driven by stellar pulsation may be enhanced by radiative pressure on circumstellar dust formed at the outer side of the "molecular atmosphere" around the central star. Some theoretical studies suggest the existence of such shock waves propagating through the H_2O maser region in the CSE, but such theoretical models have been made for mainly CSEs of carbon-rich stars, and not those of oxygen-rich stars that harbor a much larger fraction of H_2O maser sources (e.g., Höfner et al. 1995, 1998). Monitoring observations of stellar H_2O masers may provide some constraints on the theoretical models of shock waves in CSEs of oxygen-rich Miras and semiregular variables. In particular, the time and phase lags of periodic flux variation between an H_2O maser and optical/infrared stellar emission should provide a great opportunity to estimate travel times of shock waves from the stellar surface. The detection of acceleration (or deceleration) motions of individual H_2O maser features should also provide a good opportunity to directly measure the shock-wave propagation. The *apparent* acceleration motions have been found in H_2O maser spectral peaks as drifts of their line-of-sight velocities (e.g., Imai et al. 1997b; Lekht et al. 1999). VLBI observations by Imai et al. (2003) toward RT Vir detected an acceleration motion of an H_2O maser feature in its proper motion, implying the passage of such a shock wave in the CSE.

Statistical analysis of the maser kinematics may be one of the good approaches for finding a general property of the CSEs, in which the H_2O maser kinematics are complicated due to turbulence. Some characteristics of the CSEs may be found as deviations from a cluster of data points attributed to the CSE turbulence. Although it is difficult to distinguish H_2O maser emission into individual maser features or maser gas clumps in single-dish observations, they can collect the necessary sample of acceleration detections and the phase lags mentioned above in stellar H_2O masers.

Here, we report on single-dish monitoring observations of a large sample of stellar H_2O masers using the Iriki 20 m telescope of the VLBI Exploration of Radio Astrometry (VERA). VERA is a VLBI array dedicated for high-precision astrometry of H_2O and SiO masers, and aims to measure annual parallaxes and secular motions of these masers. Because they are highly variable, the maser flux densities of the targeted sources should be monitored for planning suitable schedules of astrometric observations with VERA. There already exist several monitoring observations of stellar H_2O masers spanning longer than 10 years, as cited above, while our observation program has a larger sample of stellar H_2O masers with a monitor span of three years.

Section 2 describes in detail the sample selection and the single-dish monitoring observations. Section 3 presents the statistical properties of the observed H_2O masers. Section 4 mainly discusses shock waves in the CSEs based on the phase lags of the H_2O maser variability, and velocity drifts of the spectral peaks in the H_2O maser emission.

2. Observations

2.1. Sample Selection

At first we selected stellar H_2O masers cited from the Arcetri H_2O maser source catalogue (Comoretto et al. 1990; Brand et al. 1994; Valdettaro et al. 2001) and the list of stellar H_2O masers observed with the Kashima 34 m telescope of the Kashima Space Research Center (KSRC) in the Communications Research Laboratory (CRL) (Takaba et al. 1994, 2001). They are identified as stellar sources in the IRAS Point Source Catalog (e.g., van der Veen & Habing 1988). We have selected and observed 242 stellar H_2O masers, which have either flux densities bright enough for VERA astrometry (> 10 Jy) or good candidates for position and fringe-phase reference continuum emission sources within $2.^\circ2$. They are listed in table 1. In the early stage of the monitoring observations, we have focused on finding maser sources that are constantly detectable. Finally, 85 masers have been observed at a sufficient number of epochs to make the flux variability analysis shown in the present paper. They are listed in table 2.

2.2. Single-Dish Observations

We have observed the stellar H_2O 6_{16}–5_{23} maser lines at a rest frequency of 22.235080 GHz since 2003 July using the 20 m VERA Iriki telescope. On- and off-source spectra at positions separated by $10'$ were obtained every ~ 2 min. The received signals are digitized and filtered using the VERA digital filter unit (Iguchi et al. 2005) in a base band channel with a band width of 16 MHz or 32 MHz, corresponding to a radial velocity coverage of 216 km s^{-1} or 432 km s^{-1}. These data were correlated, then Fourier transformation was made to the correlated data to obtain the total-power spectra of the maser emission with a velocity channel spacing of 0.21 km s^{-1}. The conversion factor from the antenna temperature to the flux density is about 20 Jy K^{-1}. Most of the maser spectra have rms noises, $\sigma \leq 0.05$ K, in integration time of 10–30 min. Because corrections of the antenna temperatures for the optical depths and the antenna gain variation were not applied in the present data, the scales of the antenna temperatures have relative uncertainties in the range of 5–20%.

2.3. Analysis of H_2O Maser Spectra

To obtain time-integrated maser spectra, we performed data calibration using the NewStar Package developed in Nobeyama Radio Observatory. A raw spectrum was obtained by subtracting an on-source spectrum from an off-source spectrum. The raw spectra were integrated to obtain a maser spectrum with lower noise, as mentioned above. A polynomial function was used to find a spectral baseline, which was subtracted from the integrated spectrum.

Using our original software, we derived parameters of individual peaks in the maser spectra; a local-standard-of-rest (LSR) velocity at the temperature peak, an antenna temperature at the temperature peak, and a velocity width (FWHM) of the Gaussian emission profile, through automatically finding the spectral peaks and performing Gaussian fitting to the identified peaks. Each peak was identified as a component that has at least three successive velocity channels with maser emission detected above a specific signal-to-noise ratio ($T_A \geq 5\sigma$). We

Table 1. Stellar H_2O maser sources observed with the VERA Iriki 20 m telescope.

IRAS name	Alternative designation	RA(J2000) h m s	Dec(J2000) ° ′ ″	H_2O^*
00007+5524	Y Cas	00 03 21.5	+55 40 52.1	Y
00050−2546	SY Scl	00 07 36.3	−25 29 39.0	Y
00340+6251	TY Cas	00 36 59.4	+63 08 02.0	Y
00428+6854	V524 Cas	00 45 57.4	+69 10 59.0	Y
01037+1219	WX Psc	01 06 26.0	+12 35 53.4	Y
01037+1219	...	01 06 26.9	+12 34 44.0	Y
01085+3022	IRC +30021	01 11 16.0	+30 38 06.0	N
01217+6049	BT Cas	01 24 59.9	+61 04 39.7	N
01304+6211	V669 Cas	01 33 48.8	+62 26 59.0	N
01556+4511	V370 And	01 58 41.8	+45 26 16.0	N
02143+4404	W And	02 17 33.0	+44 18 17.8	N
02168−0312	*o* Cet	02 19 20.8	−02 58 36.8	Y
02192+5821	S Per	02 22 51.7	+58 35 11.4	Y
02251+5102	RR Per	02 28 28.7	+51 16 20.2	N
02316+6455	V656 Cas	02 35 44.7	+65 08 58.7	N
02339+3402	R Tri	02 37 02.2	+34 15 50.0	N
02404+2150	YY Ari	02 43 16.7	+22 03 34.0	Y
02395+6244	...	02 43 29.1	+62 56 59.0	Y
02420+1206	RU Ari	02 44 45.0	+12 19 03.0	Y
03030+5532	IO Per	03 06 51.3	+55 43 39.0	N
03597+1115	NML Tau	03 53 28.9	+11 24 22.3	Y
04064+3321	V394 Per	04 09 37.0	+33 29 38.0	N
04094−2515	W Eri	04 11 31.0	−25 08 02.3	Y
04255+1003	R Tau	04 28 18.0	+10 09 44.7	Y
04280+2722	V779 Tau	04 31 7.3	+27 29 26.0	Y
04355+0814	RX Tau	04 38 12.8	+08 19 32.0	Y
04396+0647	BZ Tau	04 42 21.4	+06 52 39.0	Y
04575+1251	...	05 00 23.8	+12 56 06.0	N
04566+5606	TX Cam	05 00 51.1	+56 10 54.0	N
05027−2158	T Lep	05 04 50.8	−21 54 16.0	Y
05073+5248	NV Aur	05 11 19.4	+52 52 33.6	Y
05151+6312	BW Cam	05 19 48.9	+63 15 59.0	Y
05365−1404	RW Lep	05 38 52.7	−14 02 26.0	Y
05368+2841	AW Aur	05 40 00.7	+28 42 48.8	N
05388+3200	U Aur	05 42 09.1	+32 02 24.3	N
05411+6957	BX Cam	05 46 44.0	+69 58 25.0	N
05443+2707	AW Tau	05 47 27.5	+27 07 34.0	Y
05466+2316	...	05 49 41.8	+23 17 04.0	N
05506+2414	AFGL 5171	05 53 44.8	+24 14 45.0	Y
05528+2010	U Ori	05 55 49.2	+20 10 30.7	Y
05559+7430	V Cam	06 02 32.7	+74 30 27.0	N
06300+6058	AP Lyn	06 34 33.5	+60 56 29.0	Y
06346+1444	UU Gem	06 37 28.2	+14 42 16.9	N
06349+0121	SY Mon	06 37 31.3	−01 23 43.6	N
06363+5954	U Lyn	06 40 46.5	+59 52 01.6	Y
06500+0829	GX Mon	06 52 45.4	+08 25 20.0	Y
07051+6601	IRC +70074	07 10 05.8	+65 56 24.9	N
07209−2540	VY CMa	07 22 58.3	−25 46 00.3	Y
07232−0544	TT Mon	07 25 40.5	−05 51 02.0	N
07304−2032	Z Pup	07 32 38.0	−20 39 29.2	Y
07308+3037	OZ Gem	07 33 58.4	+30 30 34.0	N
07399−1435	QX Pup	07 42 16.8	−14 42 51.0	Y
07400+2334	S Gem	07 43 02.5	+23 26 57.0	Y
07542+2127	XY Gem	07 57 09.2	+21 19 10.0	N
07585−1242	U Pup	08 00 50.6	−12 50 31.0	N
08138+1152	R Cnc	08 16 33.8	+11 43 34.6	Y
09069+2527	W Cnc	09 09 52.6	+25 14 53.8	Y
09235−2347	LP Hya	09 25 50.9	−24 00 37.9	N
09331−1428	X Hya	09 35 30.3	−14 41 28.6	Y
09429−2148	IRC −20197	09 45 15.2	−22 01 44.7	N
09425+3444	R LMi	09 45 34.5	+34 30 27.0	Y
09448+1139	R Leo	09 47 33.9	+11 25 48.0	N
10411+6902	R UMa	10 44 38.4	+68 46 37.0	Y
10521+7208	VX UMa	10 55 40.2	+71 52 13.0	Y
10580−1803	R Crt	11 00 33.9	−18 19 29.6	Y
11252+1525	AF Leo	11 27 52.8	+15 08 49.0	Y

Table 1. (Continued)

IRAS name	Alternative designation	RA(J2000) h m s	Dec(J2000) ° ′ ″	H_2O^*
11462−2628	IRC −30182	11 48 44.9	−26 45 29.0	Y
11501−0719	S Crt	11 52 45.1	−07 35 48.0	Y
11577−0954	SV Vir	12 00 20.9	−10 11 07.0	Y
12016+1903	R Com	12 04 15.2	+18 47 00.0	Y
12341+5945	T UMa	12 36 23.5	+59 29 12.0	Y
12366+5845	RS UMa	12 38 57.8	+58 29 01.0	Y
12449+3838	U CVn	12 47 19.8	+38 22 31.0	Y
13001+0527	RT Vir	13 02 38.0	+05 11 08.4	Y
13068−0927	IRC −10278	13 09 31.6	−09 43 27.0	N
13172+4547	V CVn	13 19 27.9	+45 31 40.0	Y
13269−2301	R Hya	13 29 42.8	−23 16 52.9	N
13303−0656	S Vir	13 32 60.0	−07 11 47.0	N
13462−2807	W Hya	13 49 02.0	−28 22 03.5	Y
14040+1343	Z Boo	14 06 29.4	+13 29 02.0	N
14086−2839	RU Hya	14 11 34.3	−28 58 07.4	Y
14106−2940	LT Hya	14 13 32.8	−29 54 17.0	N
14219+2555	RX Boo	14 24 11.5	+25 42 15.0	Y
14247+0454	RS Vir	14 27 16.4	+04 40 44.0	Y
14349+2657	R Boo	14 37 11.8	+26 44 11.0	N
15060+0947	FV Boo	15 08 25.7	+09 36 17.0	Y
15090−0549	Y Lib	15 11 41.3	−06 00 35.0	Y
15193+3132	S CrB	15 21 24.0	+31 22 02.6	Y
15193+1429	S Ser	15 21 40.6	+14 18 30.0	Y
15214−2244	RS Lib	15 24 19.8	−22 54 39.7	N
15255+1944	WX Ser	15 27 47.1	+19 33 44.5	Y
15262+0400	...	15 28 43.8	+03 49 43.0	Y
15298+0348	WW Ser	15 32 24.6	+03 38 26.0	Y
15528−1242	SW Lib	15 55 33.4	−12 51 05.0	N
15576−1212	FS Lib	16 00 23.3	−12 20 55.0	Y
16081+2511	RU Her	16 10 14.5	+25 04 14.4	N
16235+1900	U Her	16 25 47.5	+18 53 33.0	Y
16260+3454	V697 Her	16 27 51.0	+34 48 07.0	N
16306+7223	R UMi	16 29 57.8	+72 16 49.1	Y
16325+6651	R Dra	16 32 40.3	+66 45 15.0	Y
16503+0529	RX Oph	16 52 47.7	+05 24 29.0	N
16523+0745	V970 Oph	16 54 46.4	+07 40 27.0	N
17050+1714	VY Her	17 07 17.5	+17 10 21.0	N
17119+0859	V2108 Oph	17 14 19.3	+08 56 02.0	Y
17123+1107	V438 Oph	17 14 39.9	+11 04 08.0	N
17229−0301	AH Oph	17 25 35.7	−03 03 57.0	Y
17230+0113	...	17 25 36.4	+01 11 04.0	N
17256+0504	V2296 Oph	17 28 07.8	+05 02 18.0	Y
17329+5359	SY Dra	17 33 55.7	+53 57 32.8	N
17338+0051	...	17 36 26.5	+00 49 34.0	N
17482−2824	...	17 51 26.8	−28 25 37.0	N
17501−2656	V4201 Sgr	17 53 18.5	−26 56 36.0	Y
17528+1144	...	17 55 13.6	+11 43 46.0	N
17541+1110	RT Oph	17 56 31.9	+11 10 10.0	N
17579+2335	...	18 00 03.8	+23 35 36.0	Y
17594+0826	...	18 01 49.6	+08 27 01.0	N
18009−2019	V4120 Sgr	18 03 56.5	−20 19 01.3	N
18039−0813	IRC −10395	18 06 42.7	−08 13 13.0	N
18050−2213	VX Sgr	18 08 04.1	−22 13 26.6	Y
18069+0911	V2302 Oph	18 09 19.0	+09 12 18.0	N
18076+3445	...	18 09 24.5	+34 46 22.0	N
18164−1631	...	18 19 14.7	−16 30 06.0	Y
18170+0353	...	18 19 33.3	+03 54 48.0	N
18176−1848	OH 12.8−1.9	18 20 31.5	−18 44 23.0	N
18203+0723	...	18 22 43.7	+07 24 54.0	N
18204−1344	IRC −10414	18 23 17.8	−13 42 48.5	Y
18223+1217	...	18 24 37.3	+12 19 18.0	N
18231+0855	...	18 25 33.8	+08 56 48.0	N
18254−1118	...	18 28 13.2	−11 16 08.0	N
18262+0934	...	18 28 36.6	+09 36 47.0	N
18270+0326	V2571 Oph	18 29 34.4	+03 28 12.0	N
18307−1159	...	18 33 34.2	−11 56 48.0	N

Table 1. (Continued)

IRAS name	Alternative designation	RA(J2000) h m s	Dec(J2000) ° ′ ″	H_2O*
18347+1113	V640 Oph	18 37 08.7	+11 16 15.0	N
18349+1023	V1111 Oph	18 37 20.7	+10 25 38.0	Y
18348−0526	V437 Sct	18 37 32.5	−05 23 59.4	N
18359+0847	X Oph	18 38 21.0	+08 50 02.0	N
18375+0510	...	18 39 59.8	+05 13 12.0	N
18387−0423	IRC +00363	18 41 25.3	−04 20 32.1	Y
18398+1035	V665 Oph	18 42 10.0	+10 38 54.0	N
18413+1354	V837 Her	18 43 34.5	+13 57 34.0	Y
18420+1137	...	18 44 24.6	+11 40 10.0	N
18436+4334	RW Lyr	18 45 19.9	+43 38 07.0	Y
18432−0149	V1360 Aql	18 45 53.2	−01 46 46.0	N
18441+2216	...	18 46 12.9	+22 20 08.0	N
18450−0148	W 43(OH)	18 47 42.1	−01 45 10.0	Y
18494−0130	V1364 Aql	18 52 01.9	−01 26 38.0	N
18498−0017	V1365 Aql	18 52 22.1	−00 14 06.0	N
18512+2029	...	18 53 26.6	+20 33 29.0	N
18560+0638	V1366 Aql	18 58 30.1	+06 42 57.6	N
18569+1722	...	18 59 10.8	+17 27 01.0	N
19039+0809	R Aql	19 06 22.2	+08 13 48.8	Y
19059−2219	V3880 Sgr	19 08 56.0	−22 14 21.0	Y
19087+0323	...	19 11 17.0	+03 28 22.0	N
19107+4113	RU Lyr	19 12 18.7	+41 18 04.0	N
19116+1511	...	19 13 58.3	+15 16 55.0	N
19134+2131	...	19 15 34.8	+21 36 32.0	Y
19161+2343	...	19 18 14.6	+23 49 26.0	Y
19160+0755	...	19 18 26.9	+08 00 35.0	N
19192+0922	...	19 21 36.6	+09 27 56.0	N
19243+7135	YZ Dra	19 23 45.5	+71 41 14.0	Y
19255+2123	K3 35	19 27 43.4	+21 30 03.0	Y
19256+0254	...	19 28 08.1	+03 00 24.0	N
19265+3116	...	19 28 31.0	+31 22 23.0	Y
19288+2923	...	19 30 50.3	+29 29 57.0	N
19303+1553	...	19 32 35.8	+15 59 38.0	N
19312+1950	...	19 33 24.3	+19 56 55.0	Y
19334−0033	V1319 Aql	19 36 03.5	−00 26 50.0	N
19344+0016	...	19 36 59.3	+00 23 08.0	N
19356+1136	RT Aql	19 37 57.2	+11 43 09.0	Y
19386+1513	V1433 Aql	19 40 55.2	+15 20 19.0	N
19387+1527	...	19 41 03.0	+15 34 15.0	N
19422+3506	...	19 44 06.9	+35 14 07.0	N
19462+2232	...	19 48 25.7	+22 39 55.0	N
19467+2213	...	19 48 52.4	+22 21 16.0	N
19474−0744	GY Aql	19 50 06.3	−07 36 52.6	N
19486+3247	χ Cyg	19 50 33.9	+32 54 50.6	N
19488+1346	...	19 51 09.3	+13 54 35.0	N
19493+2905	...	19 51 21.4	+29 12 59.0	N
19490+1049	...	19 51 24.7	+10 57 22.0	N
19495+0835	...	19 51 57.9	+08 42 56.0	N
19499+2141	...	19 52 07.9	+21 49 30.0	N
19511+3935	...	19 52 51.8	+39 43 24.0	N
19508+2659	...	19 52 57.6	+27 07 42.0	N
19520+2759	...	19 54 05.4	+28 07 37.0	N
19536+3237	V468 Cyg	19 55 37.9	+32 45 34.0	N
19550−0201	RR Aql	19 57 36.1	−01 53 10.8	Y
19566+3423	...	19 58 31.9	+34 31 32.0	N

Table 1. (Continued)

IRAS name	Alternative designation	RA(J2000) h m s	Dec(J2000) ° ′ ″	H_2O*
20000+4954	Z Cyg	20 01 27.1	+50 02 34.0	N
20047+1248	SY Aql	20 07 05.5	+12 57 01.0	Y
20052+0554	V1416 Aql	20 07 43.3	+06 03 13.0	N
20077−0625	V1300 Aql	20 10 27.9	−06 16 13.6	N
20097+1107	...	20 12 09.0	+11 16 50.0	N
20113+4917	AC Cyg	20 12 49.5	+49 27 00.0	N
20123+0429	...	20 14 50.1	+04 38 56.0	Y
20137+2838	...	20 15 47.3	+28 47 52.0	N
20171+2732	...	20 19 10.9	+27 42 10.0	N
20194+1707	UW Del	20 21 44.5	+17 17 25.0	Y
20246+2813	...	20 26 45.8	+28 23 53.0	N
20246+1456	WX Del	20 26 56.8	+15 06 02.0	N
20267+2105	...	20 28 57.0	+21 15 35.0	Y
20305+6246	BF Cep	20 31 27.8	+62 56 44.6	N
20350+5954	V778 Cyg	20 36 07.7	+60 05 25.0	Y
20403+3143	...	20 42 20.4	+31 54 29.0	N
...	NML Cyg	20 46 25.5	+40 06 59.6	Y
20440+0412	BR Del	20 46 33.3	+04 23 38.0	Y
20443+0215	V Aqr	20 46 49.7	+02 26 15.0	N
20460+3253	...	20 48 03.6	+33 05 02.0	Y
20482+3325	...	20 50 18.2	+33 36 32.0	N
20529+3013	UX Cyg	20 55 05.5	+30 24 52.1	Y
20547+0247	U Equ	20 57 16.3	+02 58 46.0	N
21088+6817	T Cep	21 09 31.9	+68 29 27.6	N
21120+0736	...	21 14 29.2	+07 48 33.0	Y
21174+1747	...	21 19 45.2	+18 00 33.0	Y
21286+1055	UU Peg	21 31 03.8	+11 09 33.0	Y
21306+5540	...	21 32 11.5	+55 53 55.0	N
21306+5540	...	21 32 13.0	+55 52 56.0	Y
21381+5000	V645 Cyg	21 39 58.3	+50 14 20.0	Y
21426+1228	TU Peg	21 45 04.6	+12 41 55.1	N
22017+2806	TW Peg	22 03 57.2	+28 21 04.0	N
22035+3506	SV Peg	22 05 42.0	+35 20 55.0	N
22134+5834	...	22 15 07.6	+58 49 10.0	Y
22177+5936	...	22 19 27.6	+59 51 21.0	N
22177+5936	OH 104.9+2.4	22 19 29.3	+59 51 37.6	N
22277+4534	IRC +50434	22 29 53.6	+45 50 10.0	N
22305+5803	...	22 32 24.3	+58 18 58.0	N
22402+1045	MP Peg	22 42 46.8	+11 00 51.0	N
22480+6002	IRC +60370	22 49 59.2	+60 17 55.0	Y
22516+0838	KZ Peg	22 54 11.2	+08 54 09.0	Y
22556+5833	V627 Cas	22 57 43.3	+58 49 34.9	N
23004+5642	...	23 02 31.6	+56 57 23.0	Y
23041+1016	R Peg	23 06 38.9	+10 32 38.0	Y
23173+2600	W Peg	23 19 49.9	+26 16 44.0	N
23176+4658	EU And	23 20 01.9	+47 14 26.0	Y
23182+3920	RY And	23 20 37.1	+39 37 14.0	Y
23212+3927	BU And	23 23 39.8	+39 43 40.0	N
23312+0601	IRC +10537	23 33 46.9	+06 17 57.0	N
23412−1533	R Aqr	23 43 49.5	−15 17 04.2	N
23416+6130	PZ Cas	23 44 05.4	+61 47 39.0	Y
23425+4338	EY And	23 45 02.3	+43 55 26.2	N
23496+6131	V657 Cas	23 52 04.8	+61 48 12.0	N
23528+4821	RS And	23 55 21.8	+48 38 18.0	N
23558+5106	R Cas	23 58 25.7	+51 23 18.0	Y

*H_2O maser detection. Y: detection, N: negative detection.

also obtained velocity-integrated flux densities from the spectral channel data with maser emission.

Several plots of individual H_2O maser sources are presented in figures 7 and 8 of appendix 1.

3. Results

3.1. Correlation between Maser and Optical Light Curves

In order to investigate the correlation of H_2O maser emission with optical stellar emission, optical light curve data provided by the American Association of Variable Star Observers

Table 2. Stellar H_2O masers selected for flux variablity analysis.

Plot ID	IRAS name	Alternative designation	Variable* type	P^* (d)	AAVSO[2] data?
1 ...	00007+5524	Y Cas	Mira	413.48	Y
2 ...	00050−2546	SY Scl	Mira	411	F
3 ...	00428+6854	V524 Cas	Mira	...	N
4 ...	01037+1219	WX Psc	Mira	660	N
5 ...	02168−0312	*o* Cet	Mira	331.96	Y
6 ...	02192+5821	S Per	SRc	822	Y
7 ...	02404+2150	YY Ari	unknown	...	N
8 ...	02420+1206	RU Ari	Mira	353.5	F
9 ...	03597+1115	NML Tau	Mira	470	Y
10 ...	04255+1003	R Tau	Mira	320.9	Y
11 ...	04280+2722	V779 Tau	SRb	...	N
12 ...	04355+0814	RX Tau	Mira	331.8	Y
13 ...	04396+0647	BZ Tau	SR?	400	N
14 ...	05027−2158	T Lep	Mira	368.13	Y
15 ...	05151+6312	BW Cam	Mira	...	N
16 ...	05365−1404	RW Lep	SRa	149.9	N
17 ...	05443+2707	AW Tau	Mira	654.4	F
18 ...	05528+2010	U Ori	Mira	368.3	Y
19 ...	06300+6058	AP Lyn	Mira	...	N
20 ...	06363+5954	U Lyn	Mira	433.6	Y
21 ...	06500+0829	GX Mon	Mira	527	N
22 ...	07209−2540	VY CMa	Lc	...	Y
23 ...	07304−2032	Z Pup	Mira	508.6	Y
24 ...	07399−1435	QX Pup	unknown	684	N
25 ...	07400+2334	S Gem	Mira	293.23	Y
26 ...	08138+1152	R Cnc	Mira	361.6	Y
27 ...	09069+2527	W Cnc	Mira	393.22	Y
28 ...	09331−1428	X Hya	Mira	301.1	Y
29 ...	09425+3444	R LMi	Mira	372.19	Y
30 ...	10411+6902	R UMa	Mira	301.62	Y
31 ...	10521+7208	VX UMa	Mira	215.2	Y
32 ...	10580−1803	R Crt	SRb	160	F
33 ...	11252+1525	AF Leo	SRb	107	F
34 ...	11501−0719	S Crt	SRb	155	N
35 ...	11577−0954	SV Vir	Mira	295.33	Y
36 ...	12341+5945	T UMa	Mira	256.6	Y
37 ...	12449+3838	U CVn	Mira	345.65	Y
38 ...	13001+0527	RT Vir	SRb	155	Y
39 ...	13462−2807	W Hya	SRa	361	Y
40 ...	14086−2839	RU Hya	Mira	331.5	Y
41 ...	14219+2555	RX Boo	SRb	340	Y
42 ...	14247+0454	RS Vir	Mira	353.95	Y
43 ...	15060+0947	FV Boo	unknown	...	N
44 ...	15090−0549	Y Lib	Mira	275.7	Y
45 ...	15193+3132	S CrB	Mira	360.26	Y
46 ...	15193+1429	S Ser	Mira	371.84	Y
47 ...	15255+1944	WX Ser	Mira	425.1	F
48 ...	15298+0348	WW Ser	Mira	365.8	Y
49 ...	15576−1212	FS Lib	Mira	415	N
50 ...	16235+1900	U Her	Mira	406.1	Y
51 ...	16306+7223	R UMi	SRa	325.7	Y
52 ...	16325+6651	R Dra	Mira	245.6	Y
53 ...	17119+0859	V2108 Oph	SR	...	F
54 ...	17229−0301	AH Oph	Mira	353.2	N
55 ...	17256+0504	V2296 Oph	Mira	...	N
56 ...	17501−2656	V4201 Sgr	SR/Mira	...	N
57 ...	18050−2213	VX Sgr	SRc	732	Y
58 ...	18164−1631	...	unknown	...	N
59 ...	18204−1344	IRC −10414	unknown	...	N
60 ...	18349+1023	V1111 Oph	Mira	...	N
61 ...	18413+1354	V837 Her	Mira	...	N
62 ...	18436+4334	RW Lyr	Mira	503.75	Y
63 ...	19039+0809	R Aql	Mira	284.2	Y
64 ...	19059−2219	V3880 Sgr	Mira	510	N
65 ...	19243+7135	YZ Dra	Mira	347.6	Y
66 ...	19312+1950	...	unknown	...	N
67 ...	19356+1136	RT Aql	Mira	327.11	Y
68 ...	19550−0201	RR Aql	Mira	394.78	Y
69 ...	20047+1248	SY Aql	Mira	355.92	Y
70 ...	20194+1707	UW Del	unknown	...	N
71 ...	20350+5954	V778 Cyg	Lb	...	F
72 ...	...	NML Cyg	unknown	...	N
73 ...	20440+0412	BR Del	Mira	336.55	Y
74 ...	20529+3013	UX Cyg	Mira	565	Y
75 ...	21120+0736	...	unknown	...	N
76 ...	21286+1055	UU Peg	Mira	456.5	F
77 ...	22134+5834	...	unknown	...	N
78 ...	22480+6002	IRC +60370	Mira	...	N
79 ...	22516+0838	KZ Peg	Mira	...	N
80 ...	23004+5642	...	unknown	...	N
81 ...	23041+1016	R Peg	Mira	378.1	Y
82 ...	23176+4658	EU And	SR	...	F
83 ...	23182+3920	RY And	Mira	393.4	Y
84 ...	23416+6130	PZ Cas	SRc	925	Y
85 ...	23558+5106	R Cas	Mira	430.46	Y

* Type and period of the optical light curve are cited from Benson et al. (1990) and GCVS Kholopov et al. (1985).

† Y/N: With/without optical data provided by AAVSO. F: Few data points in the AAVSO data.

(AAVSO) were used. The optical data are available for 56 out of the 85 masers that are available for the time series analysis. Table 2 lists the 56 sources along with the magnitude variation types and periods cited from Benson et al. (1990) and the General Catalog of Variable Stars (GCVS: Kholopov et al. 1985, 1992).

The photometric magnitude and the velocity-integrated flux of the H_2O masers were fitted to sine functions, respectively, described as follows:

$$m_{\rm light} = \frac{\Delta m_{\rm light}}{2} \sin \frac{2\pi(t - \Delta t_{\rm light})}{P} + \bar{m}_{\rm light} \quad (1)$$

and

$$F_{\rm H_2O} = \frac{\Delta F_{\rm H_2O}}{2} \sin \frac{2\pi(t - \Delta t_{\rm H_2O})}{P} + \bar{F}_{\rm H_2O}, \quad (2)$$

where $\Delta m_{\rm light}$ and $\Delta F_{\rm H_2O}$ are the peak-to-peak amplitudes of the optical magnitude variations and the H_2O maser flux, respectively, P the period of the optical magnitude variation estimated in the GCVS, $\Delta t_{\rm light}$ and $\Delta t_{\rm H_2O}$ the zero-phase time lags of the optical magnitude and the H_2O maser flux variations, respectively, with respect to the date reference JD 2453000; $\bar{F}_{\rm H_2O}$ and $\bar{m}_{\rm light}$ are the means of the maser fluxes and the optical magnitudes, respectively. Although an optical magnitude is a logarithm of the optical flux density, a comparison between the maser flux density and the optical magnitude is still valid as long as only the phase lag is discussed. The variation amplitudes of the maser flux densities, or their correlations with those of the optical magnitudes are not discussed in the present paper, because the amplitude changes from one periodic cycle to another, and more careful and quantitative analysis methods for such variable amplitudes have to be developed.

Table 3. Parameters of the fitted sinusoidal functions.*

IRAS name	Alternative designation	AAVSO optical data			Note‡
		$\Delta m_{\rm light}$ (mag)	$\Delta t_{\rm light}$† (d)	$\bar{m}_{\rm light}$ (mag)	
		VERA Iriki H_2O maser data			Note‡
		$\Delta F_{\rm H_2O}$ (K)	$\Delta t_{\rm H_2O}$† (d)	$\bar{F}_{\rm H_2O}$ (K)	
00007+5524	Y Cas	4.27± 0.12	140.52 ± 1.54	12.80± 0.05	...
		2.11± 0.66	156.9 ± 23.1	1.13± 0.26	...
02168−0312	*o* Cet	4.72± 0.04	117.36 ± 0.49	6.91± 0.02	...
		1.49± 0.61	160.7 ± 27.4	0.84± 0.31	...
02192+5821	S Per	1.43± 0.04	665.12 ± 2.66	10.71± 0.01	...
		0.90± 0.90	792.5 ±107.0	6.07± 0.32	Bad
03597+1115	NML Tau	4.25± 0.30	350.85 ± 3.37	15.68± 0.13	...
		2.62± 0.40	398.5 ± 10.9	1.50± 0.14	...
04255+1003	R Tau	5.34± 0.10	279.71 ± 0.69	11.21± 0.04	...
		12.35± 4.69	209.7 ± 23.0	4.29± 1.61	...
04355+0814	RX Tau	4.05± 0.08	196.79 ± 1.35	12.32± 0.04	...
		4.51± 1.71	201.3 ± 20.7	1.61± 0.68	...
05027−2158	T Lep	4.77± 0.14	256.67 ± 1.32	10.86± 0.06	...
		4.45± 0.91	301.5 ± 10.0	2.86± 0.29	...
05528+2010	U Ori	6.40± 0.06	312.49 ± 0.42	10.23± 0.03	...
		3.91± 0.78	118.9 ± 10.7	2.93± 0.27	...
06363+5954	U Lyn	4.05± 0.15	268.71 ± 2.31	12.39± 0.05	...
		0.10± 0.11	43.7 ± 85.0	0.27± 0.05	Bad
07209−2540	VY CMa	...	...	...	Bad
		...	...	...	Bad
07304−2032	Z Pup	7.25± 0.41	270.99 ± 3.28	12.63± 0.16	...
		2.15± 0.37	341.7 ± 13.4	1.01± 0.14	...
07400+2334	S Gem	5.04± 0.10	165.99 ± 0.94	12.09± 0.04	...
		0.90± 0.13	207.8 ± 6.9	0.80± 0.05	...
08138+1152	R Cnc	3.99± 0.05	186.98 ± 1.04	9.39± 0.02	...
		1.24± 0.36	227.1 ± 19.4	0.71± 0.15	...
09069+2527	W Cnc	5.12± 0.17	224.46 ± 3.09	11.80± 0.09	...
		0.66± 0.34	335.7 ± 24.0	0.34± 0.14	...
09331−1428	X Hya	3.98± 0.11	36.46 ± 1.11	10.83± 0.04	...
		2.09± 0.55	142.9 ± 10.5	1.40± 0.18	...
09425+3444	R LMi	4.45± 0.06	256.39 ± 0.89	10.82± 0.02	...
		0.15± 0.08	5.5 ±366.69	0.37± 0.03	...
10411+6902	R UMa	5.52± 0.03	65.70 ± 0.28	10.59± 0.01	...
		5.92± 0.35	152.7 ± 3.4	3.90± 0.14	...
10521+7208	VX UMa	3.84± 0.24	26.82 ± 4.94	12.79± 0.12	...
		0.41± 0.10	54.1 ± 15.0	0.47± 0.04	...
11577−0954	SV Vir	5.27± 0.38	45.76 ± 3.15	12.09± 0.16	...
		0.45± 0.11	159.9 ± 9.1	0.26± 0.04	...
12341+5945	T UMa	5.26± 0.04	2.28 ± 0.27	10.30± 0.01	...
		1.18± 0.19	159.9 ± 6.2	0.93± 0.07	§
12449+3838	U CVn	5.60± 0.19	128.83 ± 1.42	13.19± 0.08	...
		0.41± 0.13	241.6 ± 20.2	0.99± 0.05	...
13001+0527	RT Vir	0.43± 0.10	141.83 ± 6.03	8.82± 0.04	Bad
		2.79± 6.33	143.1 ± 59.1	20.47± 2.29	Bad
13462−2807	W Hya	1.93± 0.08	223.09 ± 2.07	7.92± 0.03	...
		38.54± 7.53	292.5 ± 11.2	20.43± 2.67	...
14086−2839	RU Hya	5.40± 0.27	329.72 ± 3.22	11.25± 0.13	...
		2.57± 0.58	65.9 ± 13.2	1.21± 0.20	...
14219+2555	RX Boo	0.27± 0.04	259.97 ± 6.48	8.08± 0.01	Bad
		0.83± 0.71	152.9 ± 42.0	1.72± 0.24	Bad

Table 3. (Continued)

IRAS name	Alternative designation	AAVSO optical data $\Delta m_{\rm light}$ (mag)	$\Delta t_{\rm light}$ † (d)	$\bar{m}_{\rm light}$ (mag)	Note‡
		VERA Iriki H_2O maser data ΔF_{H_2O} (K)	Δt_{H_2O} † (d)	$\bar{F}_{H_2O}$ (K)	Note‡
14247+0454	RS Vir	6.72± 0.17	115.61 ± 1.23	11.70± 0.08	...
		2.83± 0.51	165.8 ± 9.9	2.15± 0.18	...
15090−0549	Y Lib	5.62± 0.11	98.66 ± 0.78	11.45± 0.04	...
		0.87± 0.36	119.5 ± 19.3	1.45± 0.13	...
15193+3132	S CrB	5.95± 0.05	231.98 ± 0.53	9.94± 0.02	...
		3.78± 0.62	289.9 ± 8.4	2.10± 0.21	...
15193+1429	S Ser	4.89± 0.12	157.31 ± 1.78	11.52± 0.06	...
		3.29± 1.45	108.1 ± 20.5	2.19± 0.45	Bad
15298+0348	WW Ser	3.68± 0.22	356.16 ± 2.86	11.98± 0.09	...
		1.51± 0.73	403.6 ± 18.6	0.49± 0.28	...
16235+1900	U Her	4.50± 0.11	10.65 ± 1.24	9.72± 0.04	...
		1.95± 0.86	136.2 ± 26.7	1.99± 0.29	...
16306+7223	R UMi	0.98± 0.03	58.01 ± 1.67	9.79± 0.01	...
		0.14± 0.44	15.6 ±310.1	0.76± 0.15	Bad
16325+6651	R Dra	5.13± 0.04	88.48 ± 0.31	10.20± 0.02	...
		0.68± 0.20	176.6 ± 12.8	0.66± 0.08	...
18050−2213	VX Sgr	2.92± 0.11	689.24 ± 4.78	10.63± 0.04	...
		41.23±80.24	595.6 ± 85.1	21.32±16.96	Bad
18436+4334	RW Lyr	4.56± 0.16	424.08 ± 2.42	14.07± 0.06	...
		0.24± 0.26	445.4 ± 72.3	0.40± 0.09	...
19039+0809	R Aql	3.21± 0.03	105.90 ± 0.46	8.55± 0.01	...
		20.37± 5.59	157.2 ± 11.1	9.04± 1.91	...
19243+7135	YZ Dra	4.70± 0.44	103.88 ± 4.43	13.06± 0.19	...
		7.03± 2.16	150.6 ± 16.3	2.89± 0.76	...
19356+1136	RT Aql	4.79± 0.08	63.03 ± 1.06	11.66± 0.04	...
		1.78± 0.98	154.8 ± 25.0	2.69± 0.32	...
19550−0201	RR Aql	7.09± 0.34	183.96 ± 1.52	12.72± 0.15	...
		14.76± 4.74	270.6 ± 20.0	7.07± 1.76	...
20047+1248	SY Aql	4.95± 0.20	268.40 ± 2.34	12.72± 0.08	...
		4.38± 0.32	9.0 ± 4.8	3.26± 0.13	...
20440+0412	BR Del	4.30± 0.41	7.35 ± 3.54	13.16± 0.12	...
		1.24± 0.55	34.8 ± 6.8	−0.05± 0.25	...
20529+3013	UX Cyg	7.59± 0.64	389.70 ± 4.88	14.47± 0.25	...
		0.70± 0.22	444.1 ± 23.4	0.47± 0.08	...
23041+1016	R Peg	5.07± 0.05	267.94 ± 0.68	10.67± 0.02	...
		0.54± 0.11	328.7 ± 12.4	0.67± 0.04	...
23182+3920	RY And	4.52± 0.27	343.46 ± 4.73	12.73± 0.13	...
		1.10± 0.49	312.5 ± 29.5	1.14± 0.17	Bad
23416+6130	PZ Cas	0.40± 0.13	508.06 ± 49.73	8.98± 0.05	Bad
		0.91± 0.22	656.0 ± 41.6	1.71± 0.08	...
23558+5106	R Cas	5.15± 0.05	20.60 ± 0.74	8.97± 0.02	...
		0.93± 0.49	55.4 ± 24.0	0.29± 0.15	...

* The periods of H_2O maser flux and optical magnitude variations are assumed to be equal to those cited from AAVSO.
† Time offset at the optical magnitude or H_2O maser flux maxisimum with respect to the date JD2453000.
‡ "Bad" denotes bad fitting.
§ The period ($p = 256.60$d) was reestimated using the AAVSO data.

Table 4. Phase lags between H_2O maser flux and optical maginitude variations and expansion velocities of the circumstellar envelopes.

IRAS name	Alternative designation	Δt (d)	$\Delta\phi$	V_{exp} (km s^{-1})	V_{sys}* (km s^{-1})	Note
00007+5524	Y Cas	16.4± 24.7	0.04±0.06	23.3	2	$\Delta\phi = 0.2$–0.4 (Rudnitskiĭ & Pashchenko 2005)
00050−2546	SY Scl	...	...	1.8	23	
00428+6854	V524 Cas	...	...	9.8	−27	
01037+1219	WX Psc	...	...	14.3	9†	
02168−0312	*o* Cet	43.3± 27.9	0.13±0.08	0.6	47	
02192+5821	S Per	127.4±109.7	0.15±0.13	19.0	−38	$\Delta\phi = 0.01$–0.5 (Lekht et al. 2005)
02404+2150	YY Ari	...	...	2.6	−39	
02420+1206	RU Ari	...	...	1.3	20	
03597+1115	NML Tau	47.7± 14.2	0.10±0.03	11.9	35	
04255+1003	R Tau	250.9± 23.7	0.78±0.07	18.0	32	
04280+2722	V779 Tau	...	...	6.2	−5	
04355+0814	RX Tau	4.5± 22.0	0.01±0.07	2.2	−44	
05027−2158	T Lep	44.9± 11.3	0.12±0.03	4.8	−28	
05151+6312	BW Cam	...	...	11.5	50	
05365−1404	RW Lep	...	...	8.0	−58	
05443+2707	AW Tau	...	...	5.2	−14	
05528+2010	U Ori	174.7± 11.1	0.47±0.03	7.7	−45	
06300+6058	AP Lyn	...	...	17.6	−30	
06363+5954	U Lyn	208.6± 87.3	0.48±0.20	1.4	−9	
06500+0829	GX Mon	...	...	10.0	−10	
07209−2540	VY CMa	...	...	17.0	18	
07304−2032	Z Pup	70.7± 16.7	0.14±0.03	5.1	3	
07399−1435	QX Pup	...	...	13.8	29	
07400+2334	S Gem	41.8± 7.8	0.14±0.03	1.1	95	
08138+1152	R Cnc	40.1± 20.5	0.11±0.06	3.0	13	
09069+2527	W Cnc	111.3± 27.1	0.28±0.07	4.6	32	
09331−1428	X Hya	106.4± 11.7	0.35±0.04	4.9	27	
09425+3444	R LMi	110.3± 37.0	0.30±0.10	6.8	−4	
10411+6902	R UMa	87.0± 3.7	0.29±0.01	4.8	38	
10521+7208	VX UMa	27.3± 20.0	0.53±0.05	2.6	−50	
10580−1803	R Crt	...	...	6.1	10	
11252+1525	AF Leo	...	...	9.7	4	
11501−0719	S Crt	...	...	3.8	38	
11577−0954	SV Vir	114.2± 12.2	0.39±0.04	0.8	−3	
12341+5945	T UMa	0.5± 65.1	6.41±0.25	0.0	−88	
12449+3838	U CVn	112.7± 21.7	0.33±0.06	0.1	−23	
13001+0527	RT Vir	1.3± 65.2	0.01±0.42	8.6	15	
13462−2807	W Hya	69.4± 13.3	0.19±0.04	2.7	42	$\Delta\phi = 0.0$–2.1 (Pashchenko & Rudnitskii 1999)
14086−2839	RU Hya	67.7± 16.4	0.20±0.05	8.8	2	
14219+2555	RX Boo	232.9± 48.5	0.69±0.14	18.9	−14	
14247+0454	RS Vir	50.1± 11.1	0.14±0.03	2.1	−14	$\Delta\phi = 0.05$–0.35 (Lekht et al. 2001)
15060+0947	FV Boo	...	...	5.5	−7	
15090−0549	Y Lib	20.8± 20.1	0.08±0.07	3.7	15	
15193+3132	S CrB	57.9± 8.9	0.16±0.03	4.9	−1	
15193+1429	S Ser	322.7± 22.3	0.87±0.06	1.9	22	
15255+1944	WX Ser	47.4± 21.5	0.11±0.06	8.1	7	
15298+0348	WW Ser	...	...	1.3	21	
15576−1212	FS Lib	...	...	7.8	−12	
16235+1900	U Her	125.6± 27.9	0.34±0.07	4.5	−15	
16306+7223	R UMi	252.1±152.6	0.77±0.47	2.3	−7	
16325+6651	R Dra	88.1± 13.1	0.36±0.05	2.5	−120	
17119+0859	V2108 Oph	...	...	21.6	5	
17229−0301	AH Oph	...	...	1.2	53	
17256+0504	V2296 Oph	...	...	0.5	26	

Table 4. (Continued)

IRAS name	Alternative designation	Δt (d)	$\Delta\phi$	V_{exp} ($km\,s^{-1}$)	V_{sys}* ($km\,s^{-1}$)	Note
17501−2656	V4201 Sgr	...	...	19.8	−4	
18050−2213	VX Sgr	638.4± 89.8	0.87±0.12	34.7	−11	$\Delta\phi = 0.0$–1.0 (Berulis et al. 1998)
18204−1344	IRC−10414	...	...	16.0	40	
18349+1023	V1111 Oph	...	...	20.9	−40	
18413+1354	V837 Her	...	...	19.1	−9	
18436+4334	RW Lyr	21.3± 74.7	0.04±0.15	3.3	−23	
19039+0809	R Aql	51.3± 11.5	0.18±0.04	3.9	49	
19059−2219	V3880 Sgr	...	...	23.5	11	
19243+7135	YZ Dra	46.7± 20.8	0.13±0.06	5.9	15	
19356+1136	RT Aql	91.8± 26.1	0.28±0.08	5.7	−33	
19550−0201	RR Aql	86.6± 21.6	0.22±0.06	5.0	26	$\Delta\phi = 0.2$–0.5 (Pashchenko & Rudnitskii 1999)
20047+1248	SY Aql	96.5± 7.2	0.27±0.02	2.7	−50	
20350+5954	V778 Cyg	...	...	17.4	−34	
...	NML Cyg	...	...	24.6	−19	
20440+0412	BR Del	27.4± 10.4	0.08±0.03	3.4	−52	
20529+3013	UX Cyg	54.4± 28.3	0.10±0.05	7.8	2	
21120+0736	...	...	...	7.9	29	
21286+1055	UU Peg	...	...	12.9	24	
22516+0838	KZ Peg	...	...	5.8	2	
23041+1016	R Peg	60.8± 13.1	0.16±0.04	1.7	23	
23176+4658	EU And	...	...	4.0	−30	
23182+3920	RY And	362.4± 34.2	0.92±0.09	3.9	−2	
23416+6130	PZ Cas	147.9± 91.3	0.16±0.10	1.3	−43	
23558+5106	R Cas	34.8± 24.7	0.08±0.06	4.4	21	$\Delta\phi = 0.2$–0.3 (Pashchenko & Rudnitskiĭ 2004)

* Systemic LSR velocity cited from Benson et al. (1990).
† From Bujarrabal, Gómez-González, and Planeas (1989).

Table 3 gives the parameters obtained in a sine function fitting. We thus obtained 42 and 37 maser sources with good fitting solutions and 4 and 9 maser sources with bad fitting solutions in the optical emission and the H_2O maser data, respectively; 35 maser sources have good fitting solutions in both of the H_2O and optical emission data. The good identification fraction of the periodic variation in the H_2O maser sources (37/85) is smaller than, but comparable to, those found in SiO and 1612 MHz OH masers.

In order to derive the relative time and phase lags of the periodic variation between the H_2O maser and the optical stellar emission, we assume that the former variation has a positive time delay with respect to the latter variation ($\Delta t_{light} < \Delta t_{H_2O}$). We then obtain the time and phase lags, Δt and $\Delta\phi$, respectively, as

$$\Delta t = \Delta t_{H_2O} - \Delta t_{light} \geq 0 \quad \text{and} \quad \Delta\phi = \frac{\Delta t}{P}. \tag{3}$$

Table 4 gives the obtained time and phase lags for the 37 maser sources. We find that all time lags, except for the semiregular variable, VX Sgr, are shorter than 400 d, corresponding to phase lags smaller than 0.5. The latter is roughly equal to those found between the SiO maser and the optical emission (0.1–0.3, e.g., Hjalmarson & Olofsson 1979; Lane 1982; Nyman & Olofsson 1986; Le Bertre 1993; Alcolea et al. 1999; Pardo et al. 2004). Note that H_2O masers are located at larger distances from the central star than are SiO masers. The obtained time lags may have an nP ambiguity ($\Delta\phi_{true} = \Delta\phi_{obs} + nP$), where $n \geq 0$ in an integer. This possibility is discussed in subsections 3.2 and section 4. In fact, some phase lags were larger than 0.5 in the present work. Modulation of the periods of the H_2O maser flux variation should also be taken into account, which has been pointed out by previous observations (e.g., Berulis et al. 1998; Rudnitskii et al. 1999; Pashchenko & Rudnitskii 1999; Pashchenko & Rudnitskiĭ 2004; Lekht et al. 2005; Rudnitskiĭ & Pashchenko 2005). However, this cannot be discussed in the present paper because the present observations span only three years.

3.2. *Expansion Velocities of the Circumstellar Envelopes*

In order to compare the derived time and phase lags mentioned above with other physical parameters of the CSEs, we estimated one of the physical parameters, an expansion velocity of each CSE projected in the line of sight, V_{exp}, from the maximum LSR velocity offset and from the systemic or stellar LSR velocity, V_{sys}, cited from Benson et al. (1990) (table 4). Most of the derived expansion velocities are smaller than 15 $km\,s^{-1}$, but note that they are underestimated in the case where there are a few peaks or less in the spectra. In addition, different from spectra of 1612 MHz OH masers, an H_2O maser spectrum often has brighter components near the systemic or stellar velocity, as well as blueshifted and redshifted components that better reflect the CSE expansion velocity. The former may reflect that the maser components

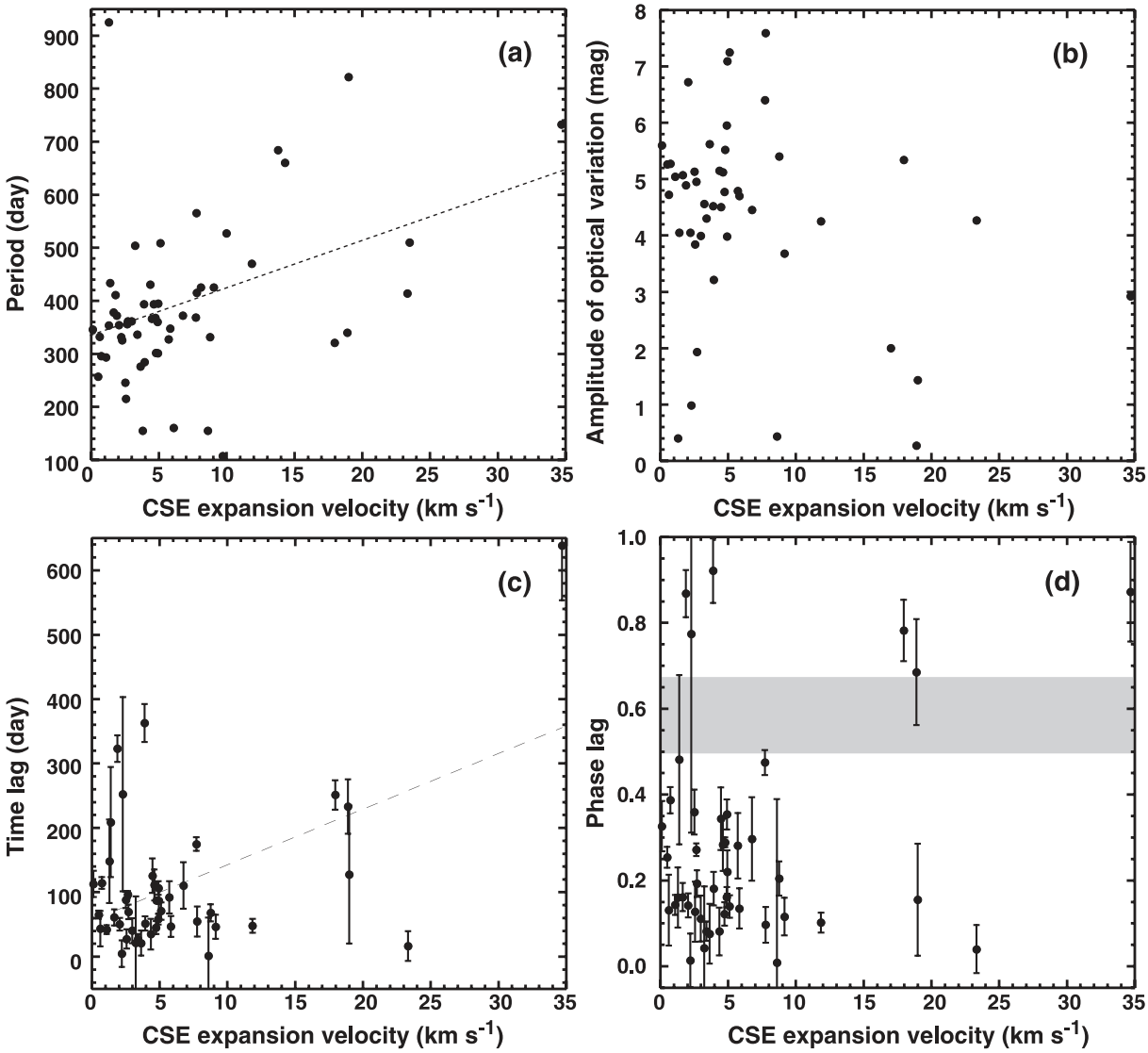

Fig. 1. CSE expansion velocity against (a) period of the maser flux and optical magnitude variation, (b) amplitude of the optical magnitude variation, (c) time lag between the H_2O maser flux and optical magnitude variations, and (d) phase lag between the H_2O maser flux and optical magnitude variations, respectively. A dashed line indicates a slope of the linear fit made for the correlation investigation. A gray shadow in the sub-panel d indicates the gap in the phase lags mentioned in the main text.

are moving on the celestial sphere, rather than along the line of sight (cf. Takaba et al. 1994, 2001). Nevertheless, the derived expansion velocities are still physically meaningful when discussing only the dynamical and physical conditions of the H_2O maser regions in CSEs. Table 4 also gives the estimated CSE expansion velocities. Figure 1 plots the periods and the amplitudes of the optical light curves and time/phase lags of the H_2O and optical variations, P, $\Delta m_{\rm light}$, Δt, and $\Delta\phi$, respectively, against the expansion velocity, $V_{\rm exp}$. We find a weak correlation between P and $V_{\rm exp}$ (a correlation coefficient $\rho_{\rm corr} = 0.41$). It is difficult to find any correlation between $\Delta m_{\rm light}$ and $V_{\rm exp}$($\rho_{\rm corr} = 0.28$). A weak correlation between Δt and $V_{\rm exp}$ ($\rho_{\rm corr} = 0.51$) is also found. The slope of the linear fit has a gradient of $8.6\,{\rm d}\,({\rm km\,s^{-1}})^{-1}$ and a zero-expansion-velocity period of 56 d. The phase lag $\Delta\phi$ seems to be constant in the range of $\Delta\phi < 0.5$ ($\rho_{\rm corr} = 0.30$) against $V_{\rm exp}$. No correlation is found between $\Delta\phi$ and P.

However, as mentioned in subsection 3.1, nP ambiguities in the time and phase lags have to be taken into account. Figure 2a shows Δt against P. Although the correlation between the two parameters is quite weak ($\rho_{\rm corr} = 0.30$) in all of the original data points we can roughly see two slopes in the Δt–P plot. The time lag increases with the period in the first slope, while it is roughly constant against the period in the second slope. We find that there is a gap at $\Delta\phi = 0.5$–0.7 in the phase-lag distribution (figure 1d), and that the second slope is composed of data points with $\Delta\phi < 0.5$. By adding one light-curve cycle days to the original time lag for the data points with $\Delta\phi < 0.5$, we newly found a much better correlation ($\rho_{\rm corr} = 0.92$) between Δt and P (figure 2b). This time-lag shift well unifies the two slopes. There is no gap in the phase lag by larger than 0.1 in the range $0.7 \leq \Delta\phi \leq 1.5$ (figure 3b). In this case, a weak correlation between Δt and $V_{\rm exp}$ is marginally found, but the correlation coefficient is only 0.17 (figure 3a).

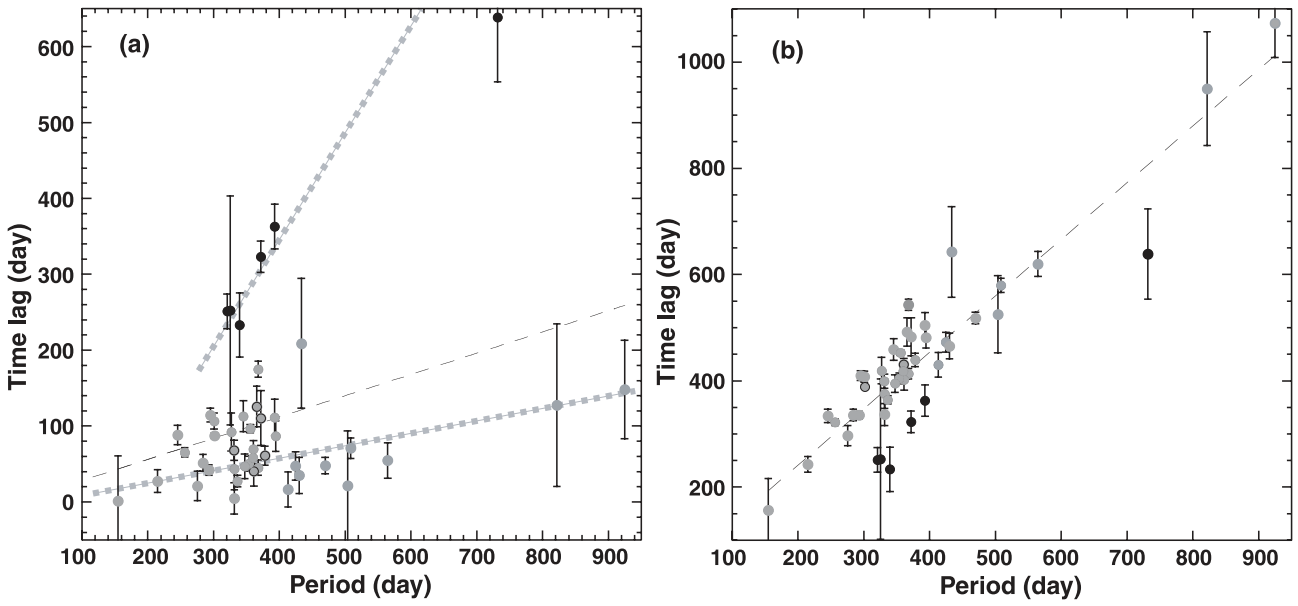

Fig. 2. Time lag between the H_2O flux and optical magnitude variations against the period of the variation. A black thin-dashed line indicates slope of the linear fit to the plot. (a) Original plot ($\Delta t = 0.28P$, $\rho_{\rm corr} = 0.35$). The possible two slopes mentioned in the main text are drawn by gray thick-dashed lines. (b) A light-curve period is added to the original time lag for the data points that have phase lags, $\Delta\phi < 0.5$, and denoted by gray filled circles ($\Delta t = 1.06P + 28$, $\rho_{\rm corr} = 0.92$).

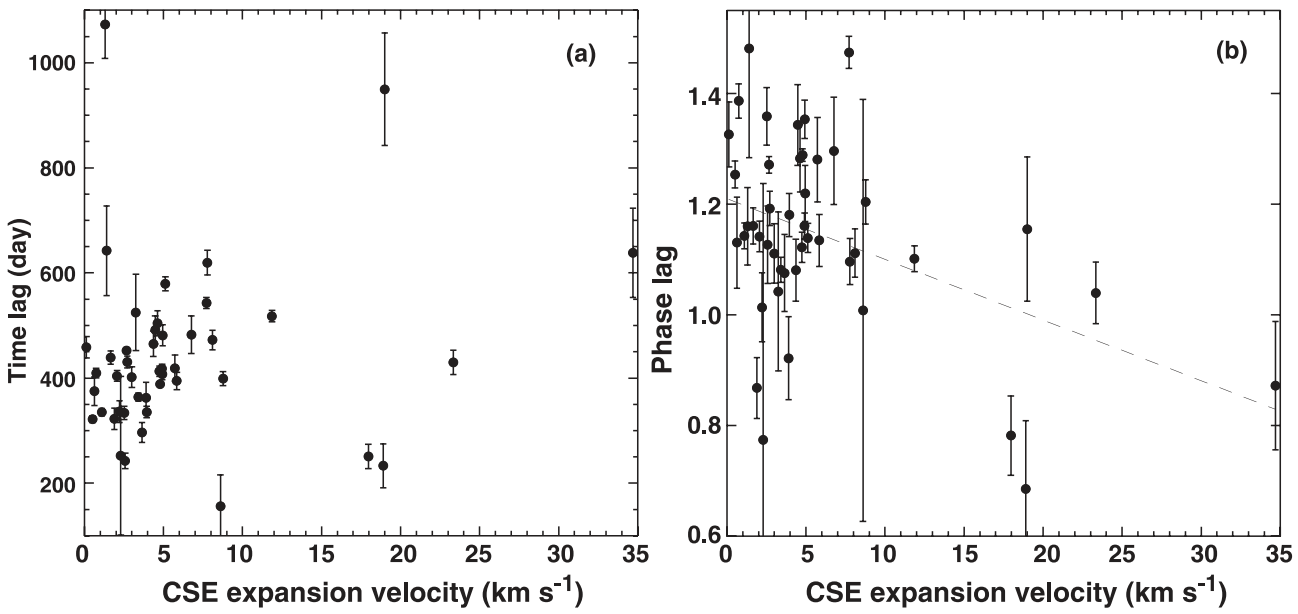

Fig. 3. (a) Same as figure 1c but for the case in which a light-curve period is added to the original time lags for the data points where $\Delta\phi < 0.5$. (b) Same as (a) but for the phase lags calculated from the modified time lags. A dashed line indicates the slope of a linear fit made for a correlation investigation ($\rho_{\rm corr} = 0.43$).

A better correlation between $\Delta\phi$ and $V_{\rm exp}$ is found ($\rho_{\rm corr} = 0.43$) (figure 3b).

3.3. Line-of-Sight Velocity Drifts

We identified H_2O spectral peaks detected at almost the same LSR velocities (within $\sim 0.2\,{\rm km\,s^{-1}}$) at two successive epochs as the same maser component. The velocity variation in each of the peaks was sometimes well fitted to a linear velocity drift during specific epochs. An expansion velocity projected in the line of sight was also calculated at each of H_2O maser gas clumps, corresponding to each of the spectral peaks with such linear velocity drifts. Table 5 gives the parameters of the linear fit, the velocity drift and the expansion velocity of each spectral peak. We find by eye that 135 out of 282 identified spectral peaks exhibit periodic variations in the flux density and in the velocity with a period roughly equal to that in the optical light curve (see column 9 of table 5 and figure 8 in page 1112). In this case, the derived velocity drift gives its mean value through

Table 5. Linear LSR velocity drifts with time seen in the maser spectra.

IRAS name	Alternative designation	ID*	$\dot{V}$ (10^6 km yr^{-2})	V_{max}†	V_{min}‡ (km s^{-1})	$T a_{max}$§	$T a_{min}$‖ (K)	Note#
00007+5524	Y Cas	1	−1.08 ± 2.29	−18.3	−19.8	3.6	0.1	Y
		2	9.01 ± 2.59	−17.3	−17.6	4.2	0.1	N
		3	1.86 ± 1.45	−16.5	−17.0	0.5	0.1	N
00050−2546	SY Scl	1	−0.53 ± 0.24	21.3	21.2	2.3	0.5	Y
		2	−3.35 ± 1.44	23.1	22.2	1.0	0.1	Y
		3	−1.47 ± 1.57	23.8	23.2	0.7	0.2	N
		4	3.27 ± 1.47	24.8	24.3	0.8	0.2	N
00428+6854	V524 Cas	1	−5.51 ± 1.88	−25.6	−26.3	0.8	0.2	Y
		2	−1.72 ± 1.08	−23.8	−24.5	0.9	0.2	N
		3	2.06 ± 2.77	−22.9	−23.9	0.5	0.1	N
01037+1219	WX Psc	1	−8.34 ± 0.64	−2.7	−3.7	6.9	0.2	Y
		2	−6.81 ± 1.28	−1.1	−2.4	1.6	0.1	Y
		3	1.78 ± 5.76	−0.4	−2.1	0.8	0.1	N
		4	13.50 ± 1.97	22.7	21.0	2.4	0.2	Y
		5	10.40 ± 1.71	23.8	22.4	3.7	0.3	Y
02168−0312	*o* Cet	1	−1.24 ± 0.44	47.6	47.4	3.3	0.2	N
02192+5821	S Per	1	3.14 ± 1.33	−56.5	−56.9	1.6	0.1	N
		2	11.00 ± 1.20	−47.2	−48.3	7.7	3.1	N
		3	−5.70 ± 1.08	−46.7	−47.2	6.8	2.0	N
		4	6.33 ± 1.16	−45.2	−46.1	3.2	0.7	N
		5	0.15 ± 0.93	−41.7	−42.1	2.2	0.4	N
		6	−20.60 ± 4.31	−37.8	−38.9	5.3	1.1	N
		7	14.90 ± 2.45	−37.7	−38.1	2.8	1.7	N
		8	−5.76 ± 0.86	−36.2	−36.8	7.1	3.5	N
		9	23.50 ± 1.46	−32.8	−34.9	1.7	0.4	N
		10	11.20 ± 0.59	−30.9	−31.9	2.2	0.4	N
		11	2.27 ± 0.28	−29.3	−29.5	2.6	0.7	N
02404+2150	YY Ari	1	−5.77 ± 0.76	−41.4	−41.6	0.8	0.2	N
02420+1206	RU Ari	1	0.99 ± 0.23	20.3	20.2	2.7	0.6	Y
03597+1115	NML Tau	1	−20.70 ± 1.86	24.4	23.1	3.1	0.2	Y
		2	−33.00 ± 2.36	24.5	23.5	4.3	0.1	N
		3	−8.25 ± 3.56	25.8	25.1	2.4	0.3	N
		4	−12.90 ± 3.32	27.2	26.1	1.4	0.3	Y
		5	−8.08 ± 0.55	28.8	27.8	5.6	0.2	Y
		6	4.50 ± 1.39	40.9	40.2	2.1	0.1	Y
04255+1003	R Tau	1	2.28 ± 0.12	14.2	14.0	16.4	1.0	N
04280+2722	V779 Tau	1	−3.18 ± 2.73	1.2	−0.3	1.0	0.1	Y
04355+0814	RX Tau	1	21.40 ± 3.47	−44.4	−44.6	8.2	0.8	N
		2	−40.10 ± 5.90	−41.7	−43.6	11.5	0.3	Y
04396+0647	BZ Tau	1	4.84 ± 2.75	14.1	13.5	0.8	0.2	N
		2	5.37 ± 2.18	14.7	13.8	0.6	0.2	N
		3	−5.52 ± 1.83	15.5	15.0	0.5	0.2	N
		4	2.20 ± 0.68	16.3	16.1	0.7	0.1	N
05027−2158	T Lep	1	5.01 ± 0.94	−29.4	−30.2	8.8	0.4	Y
		2	9.60 ± 1.00	−26.7	−26.9	4.8	0.2	N
		3	−15.30 ± 5.93	−24.4	−24.8	3.1	0.3	N
		4	−44.40 ± 6.54	−23.2	−23.8	1.6	0.2	N
05151+6312	BW Cam	1	−4.34 ± 0.66	40.4	40.0	0.8	0.1	N
		2	7.32 ± 1.16	42.1	41.6	1.1	0.2	N
		3	−3.72 ± 1.21	44.9	44.4	2.0	0.1	N
		4	−8.70 ± 1.54	45.9	45.4	2.2	0.2	N
		5	2.08 ± 0.93	61.5	61.2	1.8	0.3	N
05365−1404	RW Lep	1	2.60 ± 2.57	−63.6	−64.5	1.0	0.2	N
		2	5.82 ± 0.83	−58.6	−59.1	3.8	0.5	N

Table 5. (Continued)

IRAS name	Alternative designation	ID*	$\dot{V}$ (10^6 km yr^{-2})	V_{max}†	V_{min}‡ (km s^{-1})	Ta_{max}§	Ta_{min}‖ (K)	Note#
05443+2707	AW Tau	1	−7.47 ± 3.71	−8.8	−9.4	4.0	0.4	Y
05528+2010	U Ori	1	2.05 ± 1.26	−40.3	−40.7	1.8	0.2	Y
		2	−1.06 ± 0.90	−38.3	−38.7	7.0	0.4	Y
		3	−6.37 ± 0.74	−37.3	−38.1	4.5	0.6	Y
06300+6058	AP Lyn	1	−10.20 ± 1.65	−33.8	−33.9	0.5	0.1	N
		2	−31.40 ± 2.50	−30.0	−30.4	0.7	0.4	N
		3	0.23 ± 0.51	−27.8	−28.1	2.9	0.1	Y
		4	6.26 ± 3.00	−23.6	−24.0	0.6	0.1	N
		5	−5.43 ± 0.82	−22.8	−23.5	1.3	0.2	N
		6	3.48 ± 0.86	−21.7	−22.4	1.2	0.2	N
		7	8.92 ± 1.41	−18.2	−19.3	0.8	0.1	N
		8	3.33 ± 0.62	−15.5	−16.1	2.3	0.4	Y
		9	7.66 ± 2.53	−14.1	−14.6	0.7	0.2	N
		10	1.43 ± 1.24	−13.8	−13.9	1.4	0.5	Y
		11	16.10 ± 5.18	−12.4	−12.6	0.5	0.3	N
06363+5954	U Lyn	1	0.99 ± 1.13	−9.7	−10.4	0.5	0.1	Y
		2	2.80 ± 2.24	−8.8	−9.8	0.6	0.1	N
06500+0829	GX Mon	1	−5.18 ± 1.98	−19.5	−19.9	1.4	0.0	N
07209−2540	VY CMa	1	−12.40 ± 0.55	2.1	1.0	66.7	11.4	Y
		2	−5.96 ± 3.06	3.6	3.3	1.4	0.5	N
		3	0.57 ± 0.36	5.6	5.3	35.6	5.2	Y
		4	4.17 ± 0.27	6.7	6.4	29.1	5.5	N
		5	−10.40 ± 0.57	10.9	10.0	90.9	7.7	Y
		6	−5.68 ± 0.43	12.8	12.2	19.9	4.3	N
		7	−2.40 ± 0.30	13.5	13.2	18.3	3.7	Y
		8	1.92 ± 0.10	15.3	15.1	35.2	7.8	N
		9	2.11 ± 0.60	17.3	17.0	136.9	52.4	N
		10	1.11 ± 0.19	18.1	17.9	366.4	39.6	Y
		11	−4.65 ± 0.38	21.5	21.0	27.8	8.3	Y
		12	−4.49 ± 1.19	22.3	21.9	22.1	16.1	Y
		13	0.79 ± 0.69	23.2	23.0	16.5	2.7	N
		14	0.71 ± 0.82	25.4	25.0	8.0	1.6	Y
		15	3.51 ± 0.72	27.9	27.6	0.8	0.4	N
		16	2.39 ± 0.16	30.7	30.5	25.5	6.4	N
		17	2.89 ± 0.10	32.8	32.5	8.6	1.8	N
07304−2032	Z Pup	1	−5.29 ± 1.98	1.9	1.3	1.0	0.1	N
		2	−6.51 ± 1.55	3.1	2.2	2.6	0.3	N
		3	2.44 ± 1.74	4.5	4.0	1.2	0.3	N
		4	3.69 ± 2.21	5.1	4.5	1.7	0.2	N
		5	9.47 ± 2.27	7.1	5.9	0.9	0.2	N
07399−1435	QX Pup	1	−1.95 ± 0.55	26.3	25.8	1.2	0.5	N
		2	2.10 ± 1.51	27.0	26.3	1.1	0.4	N
		3	2.01 ± 2.88	41.9	41.2	0.5	0.1	N
		4	0.04 ± 1.65	42.8	42.0	0.4	0.1	N
07400+2334	S Gem	1	15.30 ± 0.74	95.7	94.8	1.6	0.2	Y
08138+1152	R Cnc	1	−9.44 ± 3.80	14.6	14.2	2.2	0.1	N
		2	2.99 ± 1.57	16.0	15.5	1.5	0.2	N
09069+2527	W Cnc	1	5.48 ± 0.75	35.5	35.2	0.9	0.2	N
09331−1428	X Hya	1	5.61 ± 2.11	25.5	24.6	1.6	0.1	N
		2	−3.74 ± 1.38	26.8	25.8	4.1	0.4	N
09425+3444	R LMi	1	1.70 ± 1.09	0.7	−0.1	0.6	0.2	Y
		2	0.41 ± 6.72	2.4	1.7	0.5	0.1	Y
10411+6902	R UMa	1	0.63 ± 0.24	39.2	38.9	8.0	0.3	Y
		2	2.52 ± 2.08	40.0	39.8	1.5	0.2	N

Table 5. (Continued)

IRAS name	Alternative designation	ID*	$\dot{V}$ (10^6 km yr^{-2})	V_{max}†	V_{min}‡ (km s^{-1})	$T a_{max}$§	$T a_{min}$‖ (K)	Note#
		3	4.15 ± 1.84	42.8	42.7	4.9	0.2	N
10521+7208	VX UMa	1	−1.04 ± 0.68	−49.1	−49.8	1.3	0.1	N
		2	−21.40 ± 3.56	−47.4	−49.1	0.7	0.1	N
10580−1803	R Crt	1	12.30 ± 1.83	4.3	4.0	9.7	2.1	N
		2	6.90 ± 2.16	5.2	4.6	31.4	4.6	Y
		3	0.55 ± 3.43	6.0	5.8	24.1	4.4	N
		4	−1.71 ± 1.86	7.1	6.3	14.9	0.6	N
		5	9.28 ± 2.43	7.8	7.1	14.3	0.7	N
		6	−0.43 ± 2.46	9.7	9.0	4.6	1.4	Y
		7	18.10 ± 5.35	9.2	8.9	3.0	1.5	N
		8	−1.34 ± 7.69	10.5	10.0	11.3	2.2	N
		9	54.90 ± 13.10	11.1	10.4	5.3	0.8	N
		10	8.05 ± 3.40	11.7	11.0	6.6	1.6	N
		11	−11.10 ± 2.58	12.2	12.0	19.9	1.8	N
		12	5.59 ± 1.29	13.1	12.2	8.6	1.2	Y
		13	−2.08 ± 2.83	15.0	14.1	12.0	1.1	Y
		14	10.60 ± 1.37	15.5	14.9	14.6	0.2	N
11252+1525	AF Leo	1	−3.27 ± 1.22	5.1	4.7	0.6	0.1	N
		2	−3.79 ± 1.11	7.3	6.4	5.5	0.2	Y
		3	−17.50 ± 5.88	8.7	7.5	2.1	0.2	Y
		4	12.70 ± 3.76	9.3	8.5	0.8	0.1	Y
		5	−15.70 ± 1.16	11.8	10.1	8.8	0.2	N
		6	26.20 ± 13.70	13.7	13.1	1.5	0.5	N
11501−0719	S Crt	1	9.66 ± 0.89	35.2	34.2	18.8	0.3	Y
		2	4.39 ± 2.65	35.4	34.9	1.2	0.3	N
		3	5.06 ± 1.57	39.1	38.2	1.5	0.3	N
		4	38.40 ± 10.10	39.2	38.5	3.6	1.0	N
		5	3.25 ± 1.50	40.4	39.4	2.3	0.5	Y
		6	−31.60 ± 4.50	41.2	40.7	1.0	0.3	N
11577−0954	SV Vir	1	1.28 ± 0.97	−2.2	−2.8	0.6	0.1	N
12341+5945	T UMa	1	1.04 ± 0.67	−87.9	−88.5	2.1	0.2	Y
12449+3838	U CVn	1	1.00 ± 0.36	−22.9	−23.1	1.7	0.5	Y
13001+0527	RT Vir	1	−2.44 ± 0.85	11.4	10.6	89.4	1.1	Y
		2	−0.28 ± 1.19	12.9	12.5	19.0	3.1	N
		3	−4.25 ± 0.81	13.2	12.6	13.8	2.4	N
		4	−5.82 ± 6.71	14.0	13.2	18.1	1.1	Y
		5	5.95 ± 1.23	15.0	14.3	3.6	0.4	N
		6	−2.54 ± 1.21	16.6	15.7	6.0	0.4	Y
		7	−4.20 ± 1.32	18.2	17.8	14.3	2.1	Y
		8	−20.30 ± 1.66	19.1	17.3	29.6	0.9	Y
		9	10.20 ± 3.54	19.2	18.8	5.2	0.8	N
		10	−21.20 ± 6.41	20.3	19.9	1.2	0.3	N
		11	−10.30 ± 1.31	22.1	20.8	21.0	0.2	Y
		12	0.51 ± 2.14	23.6	23.0	6.8	0.2	Y
13462−2807	W Hya	1	4.51 ± 2.18	39.5	39.3	7.0	1.1	N
		2	−8.67 ± 1.37	40.7	39.8	103.2	0.7	Y
		3	−5.77 ± 0.68	41.7	40.8	71.9	2.7	Y
14086−2839	RU Hya	1	−1.67 ± 7.80	−4.1	−4.7	3.4	0.3	N
14219+2555	RX Boo	1	2.88 ± 3.43	2.7	1.1	1.1	0.2	Y
		2	−8.67 ± 0.95	3.9	2.7	8.6	0.3	Y
		3	6.62 ± 1.59	4.9	4.0	2.1	0.2	N
14247+0454	RS Vir	1	−4.81 ± 1.33	−15.0	−16.1	1.6	0.2	N
		2	1.43 ± 0.24	−13.6	−13.9	12.9	0.6	Y
15060+0947	FV Boo	1	−1.49 ± 1.18	−10.8	−11.3	1.2	0.2	N

Table 5. (Continued)

IRAS name	Alternative designation	ID*	$\dot{V}$ (10^6 km yr^{-2})	V_{max}† (km s^{-1})	V_{min}‡ (km s^{-1})	Ta_{max}§ (K)	Ta_{min}‖ (K)	Note#
15090−0549	Y Lib	1	−28.60 ± 9.77	11.9	11.4	4.8	0.6	N
		2	2.78 ± 0.34	14.6	14.2	2.3	0.0	Y
		3	3.90 ± 3.20	16.2	15.2	0.6	0.0	N
15193+3132	S CrB	1	1.38 ± 0.93	1.5	0.7	6.1	0.4	Y
15193+1429	S Ser	1	−1.38 ± 3.46	21.8	21.0	5.9	0.1	N
		2	−1.32 ± 0.67	23.9	23.5	8.7	0.2	N
15255+1944	WX Ser	1	−4.61 ± 0.25	2.7	2.2	2.2	0.2	Y
		2	−9.25 ± 1.61	4.0	3.0	1.1	0.2	Y
		3	2.85 ± 1.12	8.5	7.8	2.3	0.1	Y
15298+0348	WW Ser	1	−2.29 ± 0.97	22.3	21.8	2.0	0.2	N
15576−1212	FS Lib	1	−2.00 ± 0.61	−4.2	−4.6	1.8	0.1	Y
16235+1900	U Her	1	1.28 ± 1.44	−16.3	−17.1	2.3	0.1	N
		2	0.92 ± 0.49	−15.1	−15.4	7.2	0.9	Y
		3	2.84 ± 1.03	−14.1	−14.5	7.5	0.8	N
16306+7223	R UMi	1	2.61 ± 2.46	−8.0	−8.9	0.4	0.1	N
		2	−5.13 ± 1.31	−7.1	−7.6	2.8	0.0	N
		3	−5.62 ± 3.10	−6.3	−6.9	0.8	0.0	N
16325+6651	R Dra	1	1.15 ± 0.72	−119.7	−119.9	1.3	0.3	N
17119+0859	V2108 Oph	1	−22.50 ± 2.37	5.0	3.8	0.5	0.1	N
		2	−14.20 ± 4.72	6.1	4.9	1.1	0.2	Y
		3	−16.00 ± 3.15	10.1	9.2	2.4	0.2	N
		4	7.55 ± 1.19	19.8	19.0	1.0	0.1	Y
		5	12.00 ± 1.67	23.3	22.6	1.5	0.1	Y
		6	9.39 ± 1.81	26.6	26.0	2.5	0.3	N
17256+0504	V2296 Oph	1	−2.06 ± 1.88	26.5	25.7	0.4	0.2	N
17501−2656	V4201 Sgr	1	−12.20 ± 0.98	−22.5	−23.8	2.0	0.1	Y
		2	−11.90 ± 1.44	−21.1	−22.4	2.4	0.5	Y
		3	−21.80 ± 1.44	−18.0	−20.0	4.8	0.2	Y
		4	−8.05 ± 2.17	−17.6	−18.4	1.5	0.7	N
		5	−9.96 ± 2.30	−16.4	−17.4	0.9	0.4	N
		6	−5.95 ± 1.12	−14.6	−15.3	4.2	0.2	Y
		7	−7.40 ± 1.42	−12.0	−12.8	0.5	0.1	N
		8	−6.42 ± 1.20	−10.6	−11.5	0.8	0.2	N
18050−2213	VX Sgr	1	−2.44 ± 0.48	−1.0	−1.3	16.9	7.5	N
		2	0.93 ± 1.28	1.2	0.9	7.1	3.5	N
		3	−0.60 ± 0.23	7.3	7.2	46.0	12.1	N
		4	−1.43 ± 0.19	10.3	10.1	5.4	1.8	N
		5	−2.32 ± 0.44	16.7	16.4	22.6	2.4	N
		6	10.60 ± 1.29	20.6	19.4	6.2	2.5	N
		7	7.87 ± 0.78	22.0	21.2	9.3	7.1	N
18204−1344	IRC −10414	1	2.64 ± 0.39	31.0	30.7	8.6	1.8	Y
		2	−0.06 ± 0.50	33.9	33.8	4.1	0.5	Y
		3	1.78 ± 1.40	34.6	34.1	4.1	0.5	N
		4	−4.79 ± 0.63	36.8	36.5	6.2	2.9	Y
		5	−5.89 ± 0.74	37.7	37.1	2.8	1.5	Y
		6	−5.37 ± 0.35	40.3	39.7	8.2	2.5	Y
		7	−0.38 ± 0.26	42.1	41.9	1.7	0.7	N
		8	2.53 ± 2.91	44.2	43.5	0.5	0.2	N
		9	0.17 ± 0.38	49.2	49.1	3.0	0.9	N
		10	0.98 ± 1.14	50.3	50.0	0.7	0.3	N
		11	0.58 ± 1.88	54.8	54.3	1.8	0.1	N
		12	−8.13 ± 1.58	56.0	55.4	2.4	0.4	Y
18349+1023	V1111 Oph	1	−1.09 ± 1.20	−20.2	−20.5	2.4	0.5	N
		2	−4.03 ± 1.42	−19.1	−19.7	2.7	0.5	N

Table 5. (Continued)

IRAS name	Alternative designation	ID*	$\dot{V}$ (10^6 km yr^{-2})	V_{max}† (km s^{-1})	V_{min}‡ (km s^{-1})	$T a_{max}$§ (K)	$T a_{min}$‖ (K)	Note#
18413+1354	V837 Her	1	−4.38 ± 1.79	−16.1	−16.7	0.7	0.1	N
		2	2.88 ± 0.13	−15.5	−15.7	1.9	0.4	N
		3	−1.70 ± 0.83	−12.9	−13.2	1.3	0.2	N
18436+4334	RW Lyr	1	1.27 ± 2.32	−20.1	−20.8	0.9	0.2	N
19039+0809	R Aql	1	2.37 ± 2.71	47.0	45.1	38.5	0.3	Y
		2	−6.08 ± 5.03	49.1	46.3	9.3	0.3	Y
19059−2219	V3880 Sgr	1	−3.30 ± 0.58	13.3	13.0	2.8	0.4	N
		2	−4.57 ± 0.61	14.6	14.2	2.0	0.7	N
19243+7135	YZ Dra	1	4.69 ± 1.05	13.6	13.0	9.5	0.2	N
		2	4.66 ± 2.30	15.0	14.3	0.4	0.2	N
19312+1950	...	1	6.53 ± 1.41	17.5	16.8	2.1	0.7	N
19356+1136	RT Aql	1	−0.49 ± 0.33	−28.7	−28.9	6.0	0.9	Y
		2	3.41 ± 2.82	−27.3	−27.8	2.1	0.2	N
19550−0201	RR Aql	1	4.04 ± 1.39	27.8	27.0	4.8	0.2	N
		2	1.38 ± 0.53	29.3	29.0	21.0	0.4	Y
		3	3.92 ± 1.50	31.0	30.5	4.3	0.3	N
20047+1248	SY Aql	1	0.11 ± 0.24	−47.3	−47.5	5.5	0.7	Y
20194+1707	UW Del	1	−0.98 ± 0.88	28.2	28.0	0.4	0.2	N
20350+5954	V778 Cyg	1	3.84 ± 0.47	−16.6	−17.0	3.7	0.4	Y
...	NML Cyg	1	−2.84 ± 0.23	−21.4	−21.6	24.2	15.1	N
		2	−3.43 ± 0.51	−17.9	−18.2	0.9	0.5	N
		3	−5.36 ± 0.42	−16.7	−17.1	2.8	0.9	N
		4	8.40 ± 1.58	2.4	1.7	0.6	0.2	N
		5	0.77 ± 0.58	5.6	5.5	6.1	2.9	N
20440+0412	BR Del	1	0.64 ± 1.08	−50.0	−50.1	0.6	0.1	N
20529+3013	UX Cyg	1	6.28 ± 1.72	−4.7	−5.2	1.0	0.1	N
		2	3.26 ± 1.80	−2.5	−3.2	1.1	0.3	Y
		3	−6.42 ± 1.70	3.7	2.6	0.7	0.1	Y
21120+0736	...	1	−13.10 ± 2.93	23.0	22.1	0.4	0.1	N
21286+1055	UU Peg	1	9.03 ± 0.76	36.9	36.0	0.8	0.1	Y
22134+5834	...	1	−5.20 ± 1.53	−16.6	−17.2	18.8	0.6	N
22480+6002	IRC +60370	1	3.41 ± 0.82	−58.0	−58.2	2.9	0.6	N
		2	−1.00 ± 2.55	−54.4	−54.8	0.6	0.2	N
		3	9.19 ± 1.69	−51.9	−52.5	8.0	0.4	N
		4	2.91 ± 2.25	−48.6	−48.9	1.4	0.6	N
22516+0838	KZ Peg	1	−1.49 ± 3.28	7.6	6.9	0.6	0.1	N
23004+5642	...	1	8.91 ± 1.64	−60.8	−61.8	2.3	0.2	N
		2	31.50 ± 4.88	−52.8	−56.2	10.0	0.2	Y
		3	9.59 ± 2.98	−50.0	−51.6	1.4	0.2	N
23041+1016	R Peg	1	2.08 ± 0.88	24.7	24.2	1.2	0.3	Y
23176+4658	EU And	1	−2.87 ± 1.12	−33.6	−34.0	1.6	0.1	N
23182+3920	RY And	1	−0.25 ± 1.17	0.5	−0.1	3.1	0.2	N
		2	−2.37 ± 1.66	1.9	1.6	0.5	0.2	N
23416+6130	PZ Cas	1	−3.33 ± 0.87	−41.3	−41.7	2.5	1.0	N
23558+5106	R Cas	1	5.32 ± 0.97	25.4	24.8	1.3	0.1	N

* Idenfified spectral peak.
† Maximum LSR velocity in the emission peak.
‡ Minumum LSR velocity in the emission peak.
§ Maximum antenna temperature in the emission peak.
‖ Minumum antenna temperature in the emission peak.
#Y/N indicates whether the velocity and flux density variations look periodic, which was confirmed by eye.

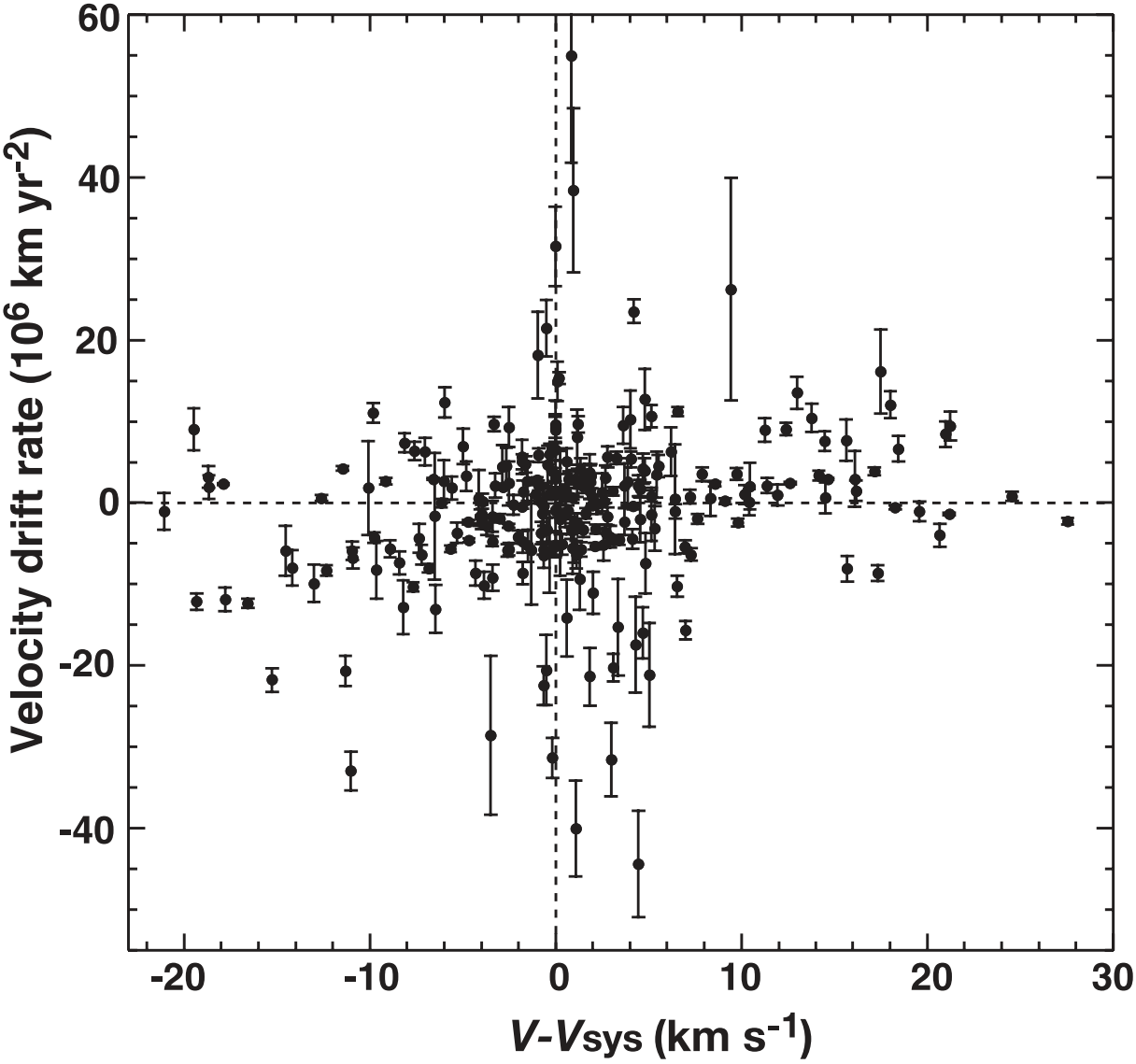

Fig. 4. LSR velocity drift against the LSR velocity of the maser spectral peak.

the appearance of a peak. The origin of such a periodic variation of the peak velocity is discussed in subsection 4.3. VLBI maps show that some of velocity peaks in the H_2O spectra are often composed of a few maser features or gas clumps with slightly different peak velocities. In this case, their different time variations in flux density may cause an apparent velocity drift in the spectrum. To identify true acceleration motions, either coherent velocity drifts among multiple spectral peaks in the same stellar object or some statistical trend of the velocity drifts in many stellar objects should be found. The latter case may be more feasible than the former one because there are usually a few spectral peaks in each stellar object.

Figure 4 shows the velocity drift rate of the peak against its expansion velocity. We find that the $(V - V_{\rm sys}, \dot{V})$ points with large amplitudes of acceleration ($|\dot{V}| \geq 10^7\,{\rm km\,yr^{-2}} \simeq 0.32\,{\rm km\,s^{-1}\,yr^{-1}}$) are concentrated in the first and third quadrants, in which the velocity drift is in the same sense as the radial acceleration. This implies that the individual maser features corresponding to the spectral peaks are gradually accelerating outwards, although each of the maser clumps may be accelerated and decelerated periodically, as mentioned above. The plot points located around the plot origin ($|V - V_{\rm sys}| \lesssim 5\,{\rm km\,s^{-1}}$, $|\dot{V}| \lesssim 10^7\,{\rm km\,yr^{-2}}$) may indicate turbulence in CSEs, as observed in the maser feature proper motions (e.g., Marvel 1997; Imai et al. 2003). The plot points located in the second and fourth quadrants may indicate deceleration, but those with large amplitudes of acceleration ($|\dot{V}| \geq 10^7\,{\rm km\,yr^{-2}}$) are biased to the fourth quadrant. Some of them may be caused by a periodic variation in the peak velocity, as mentioned above, but the reason for the bias is still in an open question.

4. Discussion

We have confirmed 37 stellar H_2O maser sources that exhibit periodic behavior in the maser emission which has a good correlation with the optical light curves. Thus, together with

SiO and OH maser emission, H_2O maser emission also reflects the stellar pulsation and the dynamical change of the CSEs affected by the pulsation. The origin of the periodic variation in H_2O maser emission is expected to be shock waves that are periodically generated and propagating outwards in the CSE. A collisional pumping scheme is expected as being the mechanism of H_2O maser excitation, in which H_2O masers are excited in a mass-loss flow from the AGB star by an interaction with the ambient circumstellar thick gas envelope (e.g., Cooke & Elitzur 1985; Elitzur 1992a). Such an interface may correspond to the shock wave mentioned here, in which the kinematic energy of the flow is released and a physical condition suitable for H_2O maser excitation ($n_{H_2} \geq 10^6 \mathrm{cm}^{-1}$, $T_{\mathrm{gas}} = 400$–$1000\,\mathrm{K}$) is provided. If the speed of shock-wave propagation is larger than the outward speed of the maser gas clump, then the gas clump is decelerated at first, and then accelerated outwards before and after passage of the shock wave, respectively. This hypothesis well explains the periodic variation in the velocity of the H_2O maser spectral peak. Taking into account maser amplification in a velocity-coherent path, a growth of maser flux is expected at the transition from acceleration to deceleration of the maser clump. Such a correlation between the maser flux and the acceleration/deceleration of a gas clump is often found, as shown in subsection 3.3. Not only these periodic variations in H_2O maser emission are observational evidence for the existence of shock waves in the CSEs. In some of V_r–θ diagrams obtained from interferometric observation data, one can see a few (not only one) chains of maser spots exhibiting individual expanding thin shells in the CSEs. Here V_r and θ are the relative line-of-sight velocity of the maser feature with respect to the stellar velocity and the angular distance from the star, respectively. This implies that one shock wave after another are generated from the central star (e.g., Bowers et al. 1993; Bowers & Johnston 1994; Yates & Cohen 1994; Richards & Yates 1998; Bains et al. 2003). Here, we demonstrate the detection of *propagation* of pulsation-driven shock waves from evolved stars, and discuss the propagation speed of shock waves through the present work.

4.1. *Possible Time and Phase Lags of Periodic Variation between H_2O Maser and Optical Stellar Emission*

At first, the possible ranges of the time and phase delays of the periodic variation between the H_2O maser and the optical stellar emission are discussed.

The thin shells found in the H_2O maser regions are located at 5–50 AU from the central star, and moving outwards with velocities in the range of ~ 5–$20\,\mathrm{km\,s}^{-1}$ (Bowers et al. 1993; Bowers & Johnston 1994). Theoretical models and the detection of acceleration motions of individual maser features suggest that the speed of propagation of shock waves (up to $50\,\mathrm{km\,s}^{-1}$: Höfner et al. 1995) is comparable to, or larger than, that of the mass-loss flow. The travel time for a gas clump in the mass-loss flow from the stellar surface to the H_2O maser region is estimated to be as long as 10 yr. The detection of "super-periods" ($P > 10\,\mathrm{yr}$) in the H_2O maser flux variation supports that the time delays of the variation in the H_2O maser flux with respect to that in the stellar optical magnitude have such a long time scale (e.g., Pashchenko & Rudnitskii 1999). A smooth variation of the phase lag [e.g., $\Delta\phi = 0.0$–2.1 for W Hya, Rudnitskii et al. (1999), see also notes in table 4] also supports such a long time lag. These facts suggest that the time and phase lags that we observed should have an nP ambiguity, as pointed out in subsection 3.1, where n should be a large positive integer.

However, such a smooth phase-lag variation is observed in only the H_2O masers around semiregular variables, such as W Hya, VX Sgr, and RR Aql, in which the passage of shock waves may also semi-regularly occur. Furthermore, the longer time lag requires a larger distance to the H_2O maser region from the central star, while the speed of the mass-loss flow and shock waves should be faster at the larger distance, and approach the terminal velocity observed in 1612 MHz OH masers (e.g., Bains et al. 2003). Therefore, the time lags may be shorter ($\Delta t \leq 5\,\mathrm{yr}$), suggesting an upper limit to the integer $n < 2$–3. Also, suppose a good correlation between the time lag and the period of the flux variation (figure 3b), which suggests a strong convergence of the integer ($n = 0$ or 1). With the larger number, the time lags should be much more scattered for the H_2O maser regions in the CSEs with specific thicknesses. Furthermore, there always exist only one or two maser feature chains exhibiting thin shells in interferometric maps of H_2O masers (Bowers et al. 1993; Bowers & Johnston 1994; Richards et al. 1996; Bains et al. 2003; Imai et al. 2003).

At the same time, the phase lags in the H_2O maser flux variation that have been previously reported ($\Delta\phi = 0.2$–0.5: Lekht et al. 1999; Pashchenko & Rudnitskiĭ 2004; Rudnitskiĭ & Pashchenko 2005) are supposed to be underestimated. The reported phase-lag range is almost equal to that found in the SiO maser flux variation (0.1–0.3: e.g., Hjalmarson & Olofsson 1979; Lane 1982; Nyman & Olofsson 1986; Le Bertre 1993; Alcolea et al. 1999; Pardo et al. 2004), misleadingly implying that H_2O masers are located at the same region as SiO masers. Therefore, we believe that the true phase lags should range over $0.7 \leq \Delta\phi \leq 1.5$. In this case, the relative phase lags between the SiO to H_2O maser variations are expected to be in the range of 0.4–1.4.

4.2. *The Origin of Time Lags of H_2O Maser Flux Variation*

Stellar radiation pressure on circumstellar dust accelerates the flow in the H_2O maser region. It is theoretically predicted that the shock waves mentioned above are amplified in the circumstellar dust envelopes, and are propagating outwards from the flow base, where dust formation occurs and the radiation pressure is enhanced, at a speed slightly higher than the flow velocity (e.g., Höfner et al. 1995, 1998). Stellar H_2O masers may be excited in such shocks periodically created in the CSE by stellar pulsation (e.g., Elitzur 1992a; Richards & Yates 1998; Bains et al. 2003; Imai et al. 2003). If the H_2O maser region is away from the layer where the dust-induced radiative pressure triggers such a shock wave, H_2O maser excitation may have a time lag from optical and infrared light curves. The origin of the phase lag between the variations in stellar optical and SiO maser emission is still obscure. The time lag measured in the present paper consists of the time lag seen in SiO maser emission, and a travel time for dusty molecular gas from the base of the flow to the H_2O maser region. The time lag between the SiO maser excitation and the ignition of a shock wave may be negligible, because no clear time lag has

yet been recognized between the SiO maser and the infrared emission variations.

We note that the phase-lag range of the H_2O maser emission is wider than that of SiO maser emission, suggesting that some trigger exists to change the physical condition of the CSE, possibly shock waves, as discussed here, and is propagating on a longer time scale over the wider area of the CSE for H_2O maser excitation than for SiO maser excitation. Here, suppose the velocity field of the H_2O maser region, v, as to be a function of the radius or distance from the star, $r \geq r_0$, where r_0 is the inner radius of the dust envelope or the base of the accelerated flow. For the case of acceleration of the CSE due to dust-induced radiative pressure, the velocity field is given as follows (Elitzur 1992a; Elitzur et al. 2003):

$$v^2 = v_\infty^2 \left(1 - \frac{r_0}{r}\right) \text{ and } v_\infty^2 = \frac{n_\mathrm{d}\sigma_\mathrm{d}\langle Q\rangle}{2\pi r_0 c m_\mathrm{H} n_\mathrm{H}} L_*, \tag{4}$$

where v_∞ is the terminal velocity at the outer edge of the envelope, n_d the number density of dust, σ_d the collisional cross section of a dust particle against an infrared photon, Q the efficiency coefficient of the radiative pressure to a dust particles, n_H the number density of hydrogen atoms, m_H the mass of a hydrogen atom, c the speed of light, and L_* the stellar luminosity. The shock wave discussed here should also be propagating at a similar velocity. The stellar luminosity is written using the stellar temperature and the radius, T_* and R_* respectively, as follow:

$$L_* = 4\pi R_*^2 \sigma T_*^4, \tag{5}$$

where σ is Stefan–Boltzman's constant. It is expected that the dust temperature and the kinematic temperature of molecular gas in the H_2O maser region are approximately equal, $T_\mathrm{d} = T_{\mathrm{H_2O}}$. Taking into account the dust opacity, T_d at the base of the outflow is calculated as follow (Cooke & Elitzur 1985):

$$T_\mathrm{d} = T_* \left(\frac{r_0}{R_*}\right)^{-2/5} = \left(\frac{L_*}{4\pi\sigma}\right)^{1/5} T_*^{1/5} r_0^{-2/5}. \tag{6}$$

Because H_2O masers are excited in the molecular gas with a specific temperature range, $T_{\mathrm{H_2O}} = 400$–1000 K (e.g., Elitzur 1992a), behind the base of the flow, here T_d may be roughly constant among stellar H_2O maser sources. Therefore, taking into account similar stellar spectral types (M) or stellar surface temperatures among the evolved stars, one obtains the simple relation between the stellar luminosity and the radius of the flow base,

$$r_0 \propto L_*^{1/2}. \tag{7}$$

From equations (4) and (7), one can derive the relation

$$v^2 \propto r_0 \left(1 - \frac{r_0}{r}\right) \propto L_*^{1/2} \left(1 - \frac{r_0}{r}\right). \tag{8}$$

Thus, one finds a correlation between v^2 and r_0 or L_*. One then obtains the acceleration, α:

$$\alpha = \frac{d^2 r}{dt^2} \propto \frac{L_*^{1/2} r_0}{r^2}. \tag{9}$$

According to a numerical calculation (see figure 5), the flow velocity asymptotically converges to the terminal velocity at $r_\mathrm{crit}/r_0 \sim 2$, $v_\mathrm{crit}/v_\infty \sim 0.7$, beyond which H_2O maser emission

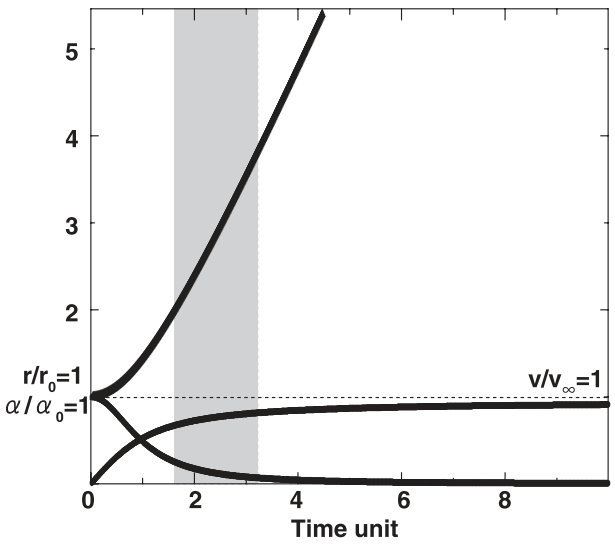

Fig. 5. Distance (r/r_0), velocity (v/v_0), and acceleration (α/α_0) where α_0 is the acceleration value at the distance r_0 in the model of a flow in a circumstellar envelope. A gray zone roughly represents a possible area of H_2O maser region in the CSE.

is well found. Beyond this critical point, the travel time from the flow base is roughly proportional to the distance from the central star, and inversely proportional to the flow expansion velocity.

Using the precise $\log P$–K-magnitude relation found in Miras in the Large and Small Magellanic Clouds (C-sequence, Ita et al. 2004),

$$K = a \log P + b, \ a = -3.5, \text{ and } b = 19.5, \tag{10}$$

one can derive the relation $L_* \propto P^{1.4}$; then,

$$v \propto P^{0.35} \left(1 - \frac{r_0}{r}\right)^{1/2}. \tag{11}$$

The observed good correlation between the H_2O maser time lag, Δt, and the period, P ($\Delta t \propto P$, figure 2b), preferably suggests the H_2O maser region distance to be $r > r_\mathrm{crit}$. There Δt approximately has a correlation with P, as follows:

$$\Delta t \gtrsim \frac{r_0}{v} \propto P^{0.35}. \tag{12}$$

In the same way, one can derive the correlation between the phase lag, $\Delta\phi$, and the CSE expansion velocity, v,

$$\Delta\phi = \frac{\Delta t}{P} \propto P^{-0.65} \propto v^{-1.86}. \tag{13}$$

In fact, a such steep decrease in the phase lag with the CSE expansion velocity is not observed (figures 1d and 3b). This suggests that the approximation adopted to derive equation (12) is not so valid for a further precise discussion. Thus, the H_2O maser region is still in the transition space to reaching the terminal expansion velocity ($r \sim 2r_0$). Also, the phase lag of the H_2O maser flux variation with respect to the stellar optical light curve still converges within a limited range ($\Delta\phi = 0.7$–1.5).

4.3. Passage of Shock Waves in the H_2O Maser Region

In addition to acceleration in the CSE, discussed in subsection 4.2, the acceleration/deceleration of individual H_2O maser

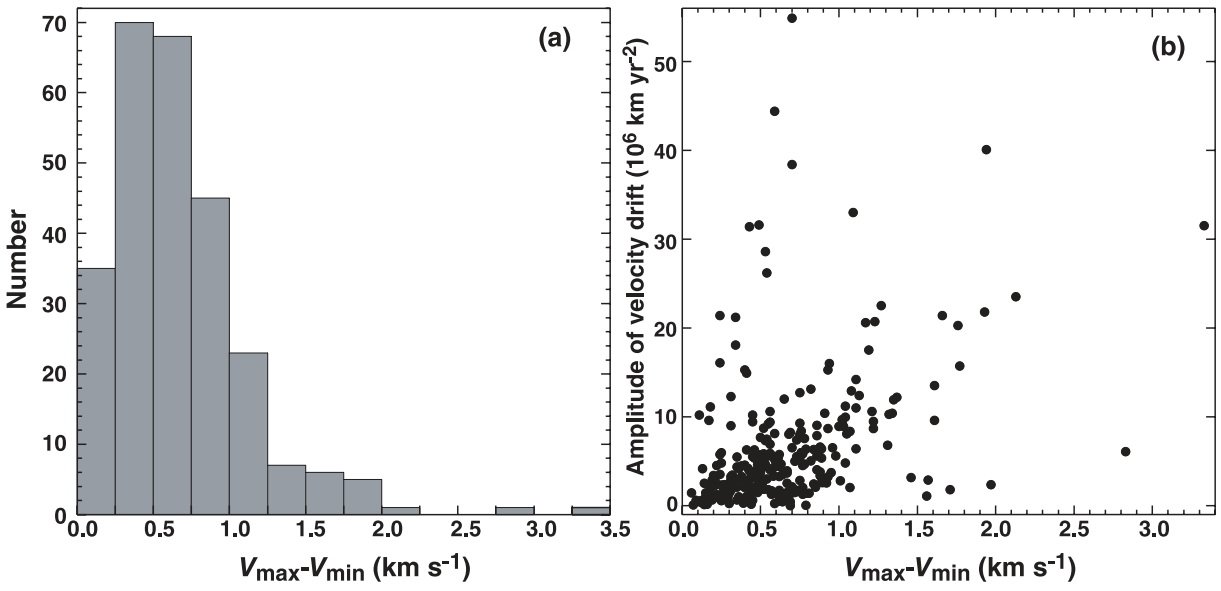

Fig. 6. (a) Histogram of velocity variations ($V_{\rm max} - V_{\rm min}$) in H_2O maser spectral peaks. (b) Amplitude of LSR velocity drift rate against the velocity variation.

gas clumps is expected to exist on a shorter time scale through the passage of shock waves.

It is notable that some of individual H_2O maser spectral peaks exhibit very similar performance to the stellar optical light curve (figure 7 in appendix 1). In particular, the former performance has the time scale of the flux growth and decay, which is almost equal to the latter time scale. This strongly supports the hypothesis that the pulsation shock waves directly affect excitation of the H_2O masers. Sometimes time lags of the flux and velocity variations are observed among different maser peaks in the same star (see appendix 2). Such time lags might be attributed to a difference in the travel times of light, which is expected in those of 1612 MHz OH masers (e.g., Herman & Habing 1985; van Langevelde et al. 1990). However, the expected time scale is negligible (within one day) for the smaller area of the H_2O maser region. They may be attributed to the difference in the travel times of the same shock wave to the maser gas clumps, reflecting the scale of the H_2O maser distribution.

It is also interesting to discuss whether the lifetimes and the physical sizes of the individual maser features around pulsating stars are controlled by shock waves. Acceleration may form a steep velocity gradient in the gas clump, while maser amplification requires velocity coherence along the amplification path. Figure 6 shows histogram of the LSR velocity variations of the H_2O maser spectral peaks ($\Delta V = V_{\rm max} - V_{\rm min}$) and their distribution against the amplitude of the velocity drift rate. The number of specific velocity variations has a peak at around $\Delta V \sim 0.5\,{\rm km\,s^{-1}}$, which may correspond to the typical line width of H_2O maser emission (e.g., Reid & Moran 1981; Elitzur 1992a). Maser features with large amplitudes of the velocity drift, which may trace the acceleration/deceleration motion, as discussed in subsection 3.3, are mainly distributed in the limited range of the velocity variation, $\Delta V \lesssim 2\,{\rm km\,s^{-1}}$. Even within this velocity variation, ($\Delta V \lesssim V_\infty/10$), a maser clump can survive from the inner to the outer layer of the H_2O maser region (see figure 5). Thus, the velocity gradients seen in the H_2O maser region do not seem to be so steep that H_2O maser emission is quenched by the passage of a shock wave. In fact, a small fraction of the maser spectral peaks exhibit large velocity drifts ($\dot{V} \geq 10^7\,{\rm km\,yr^{-2}}$). The similarity of the variations in the H_2O maser and the stellar optical emission, as discussed above, also supports the large sizes and long lifetimes of the maser gas clumps. Furthermore, previous VLBI observations report a larger size of the H_2O maser features around evolved stars than those in the star-forming region (≥ 1 AU, e.g., Imai et al. 1997a).

Note that, however, larger amplitudes of acceleration of the H_2O maser features are sometimes found. They are more observable on the celestial sphere than in the line of sight, because a velocity gradient along the line of sight is smaller in the former case (Imai et al. 2003). The detectability of large acceleration/deceleration motions may be a good parameter to understand the physical environments of O-rich CSEs. Theoretical studies have predicted that C-rich CSEs enhance stellar-pulsation shock waves more than do O-rich CSEs (e.g., Höfner et al. 1995, 1998). On the contrary, our current observational studies suggest that O-rich CSEs may also well enhance such shock waves in the H_2O maser regions. To more precisely discuss the enhancement of the shock waves, we need statistical analyses more precisely on the basis of a larger sample of monitoring observations of stellar H_2O maser sources.

5. Conclusions

The samples of H_2O maser and stellar optical emission for 46 AGB stars shown in the present paper enabled us to make statistical analyses for elucidating the physical properties of H_2O maser gas clumps and accompanying CSEs. A large fraction of stellar H_2O masers have a periodic behavior with the period being equal to that of the stellar pulsation. We found a clear correlation between the time lag of the H_2O maser flux

variation with respect to the optical magnitude variation and the stellar pulsation period, leading to a limited phase lag range of $0.7 \leq \Delta\phi \leq 1.5$. The behavior of H_2O maser emission is demonstrated by the passage of shock waves, which are propagating from the stellar surface, and are then enhanced by dust-induced radiative pressure. Radial acceleration of the CSEs is also detected through measurements of LSR velocity drifts of individual spectral peaks of H_2O maser emission. A large fraction of small amplitudes of the velocity drifts indicates that CSEs are mildly accelerated in the H_2O maser region after rapid acceleration that is triggered at the launch of the dust-induced radiative pressure.

VERA observatory is a branch of the National Astronomical Observatory, an interuniversity research institute operated by the Ministry of Education, Culture, Sports, Science and Technology. We gratefully acknowledge the AAVSO International Database, which is based on observations submitted to the AAVSO by variable-star observers worldwide. We deeply appreciate Dr. Shuji Deguchi for carefully reading the manuscript and providing critical comments. This observational study has been supported by Grant-in-Aid for Scientific Research from the Japan Society for the Promotion Science (16540224, 17340055) and by Grant-in-Aid for Young Scientists (B) from the Ministry of Education, Culture, Sports, Science and Technology (18740109).

Appendix 1. Plots of Individual H_2O Maser Sources

Figure 7 shows the time variation in the H_2O maser spectrum and the maser flux (antenna temperature) for each of the maser sources. The maximum antenna temperature and the velocity-integrated flux density at each epoch are plotted. Figure 7 also shows, if available the AAVSO light curves. Figure 8 shows variation of the LSR velocity and the antenna temperature at each peak in the maser spectrum during the monitoring observations.

Appendix 2. Comments on Individual Stellar H_2O Maser Sources

Y Cas

The long-term monitoring observations by Pashchenko & Rudnitskiĭ (2004) have revealed that the phase lag has changed in the range $\Delta\phi = 0.2$–0.4, which is inconsistent with that found in the present result ($\Delta\phi \sim 0.0$). However, the relative difference between the results with respect to the pulsation period is reduced if we adopt possible phase lags of $\Delta\phi = 1.2$–1.4 and $\Delta\phi \sim 1.0$, respectively.

WX Psc

Periodic variations in the flux density were found in both the blue-shifted and red-shifted maser peaks. The variation phase comes earlier in the red-shifted components by a relative time lag of ≈ 7.5 d than in the blue-shifted components. By multiplying the CSE expansion velocity of $\approx 14\,\mathrm{km\,s^{-1}}$ (table 4), we obtain a travel path difference of only 0.06 AU. This suggests that these components are located at the same distance from the central star. In fact, they are apparently located very close to the expected location of the star, and may be approaching and receding conponents with large inclinations from the line of sight (Inomata et al. 2007).

S Per

Lekht et al. (2005) have made long-term observations of the H_2O masers and identified the periodic flux variation with the phase lag changing in the range of $\Delta\phi = 0.01$–0.5. Bipolarity in the H_2O maser spatio-kinematical structure has been identified (Marvel 1997; Richards et al. 2004; Asaki et al. 2007). With the annual-parallax method using the VLBA, Asaki et al. (2007) measured the distance to S Per, $D = 2.51 \pm 0.09$ kpc.

NML Tau

Although this maser source does not have any suitable reference calibrator for VERA astrometry, it has been observed many times. Due to a large amplitude of the maser flux variation, it was difficult to exactly trace the time variation of the maser flux. One of the spectral peaks (ID 5) exhibits a systematic velocity drift, indicating radial acceleration for three years.

T Lep

A clear periodic variation in the velocity-integrated maser flux has been recognized. Each of spectral peaks also has a time variation in the maser peak flux synchronized with that of the velocity-integrated maser flux. The apparent radial deceleration was recognized in the spectral peaks as the maser flux decreased.

AP Lyn (IRC +60169)

Although we have obtained a nice maser light curve, we could not obtain optical light curve data for this OH/IR star, which may be invisible at optical wavelengths. Sudou et al. (2002) measured the relative proper motions of the H_2O maser features, but which exhibited a complicated kinematical structure. Instead, they found systematic change in the maser feature extent during a monitoring observation.

VY CMa

For this supergiant, although the flux variation of H_2O maser emission has been identified, it is difficult to find its periodicity. With the annual-parallax method using VERA, Choi et al. (2008) measured the distance to VY CMa; $D = 1.15 \pm 0.10$ kpc (cf. $D = 1.4 \pm 0.2$ kpc, Marvel 1997).

R Crt

Rich maser emission peaks have been found in the velocity range $3\,\mathrm{km\,s^{-1}} \leq V_{\mathrm{LSR}} \leq 17\,\mathrm{km\,s^{-1}}$. The lifetimes of most of the individual maser features seem to be relatively short ($\lesssim 300$ d). The 1665 MHz and 1667 MHz maser fluxes exhibit periodic variations with two periods of 227 d and 560 d (Etoka et al. 2001). Ishitsuka et al. (2001) found the three-dimensional expansion motion of the envelope, but could not detect any clear signature of acceleration of the H_2O maser features.

(Continued to p.1129)

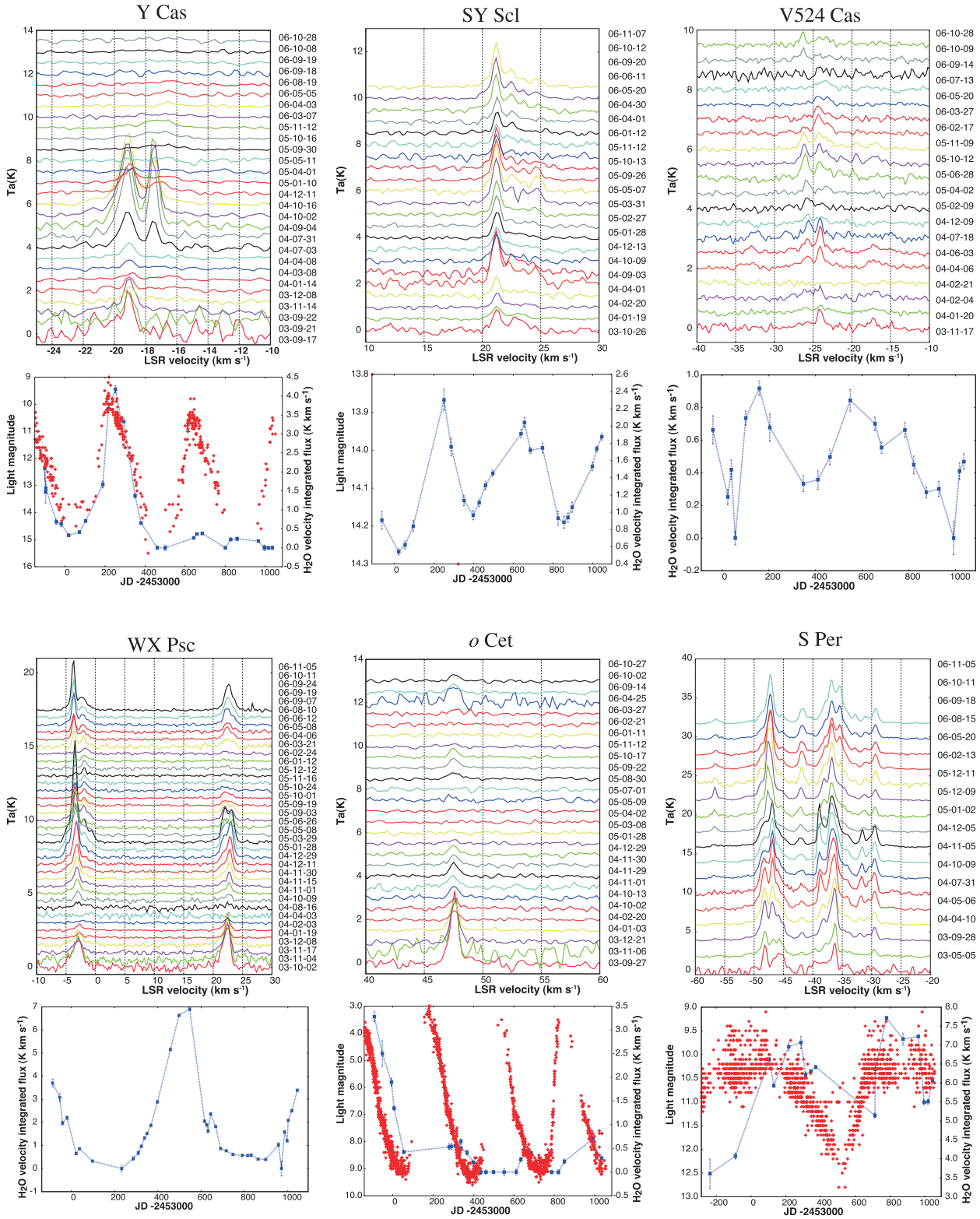

Fig. 7. Top: Time series of H_2O maser spectra in each source, advancing in time from bottom to top. The observation dates are shown in the form YY-MM-DD (year–month–day). Bottom: Time variation of the velocity integrated flux of H_2O maser emission (cross connected by a dotted line to the adjacent data point) and that of the optical magnitude, which have been obtained by AAVSO (plus, if available). A maser flux is set to zero in the case of negative detection. An error bar for the negative detection indicates the 3-σ upper limit to the flux.

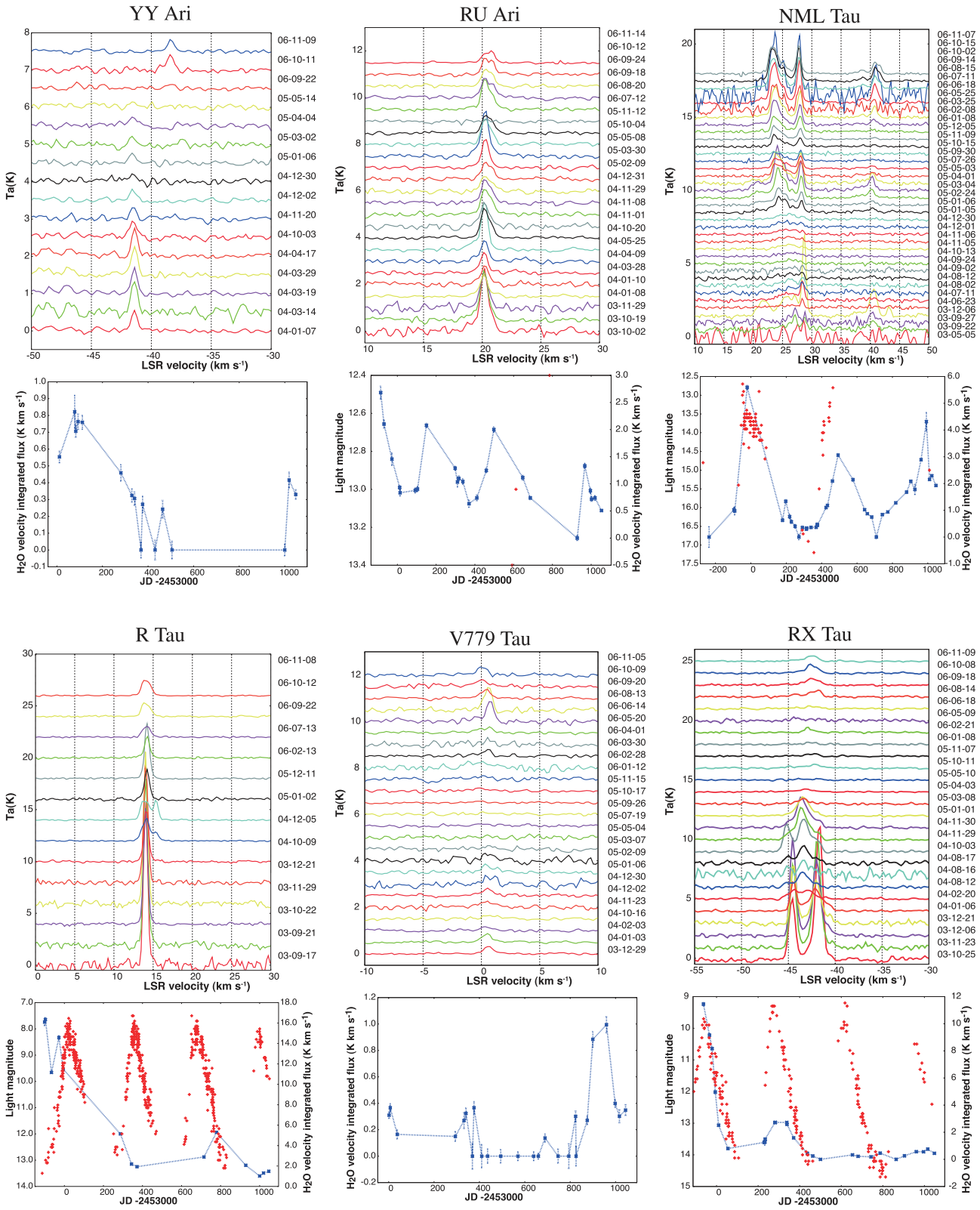

Fig. 7. (Continued)

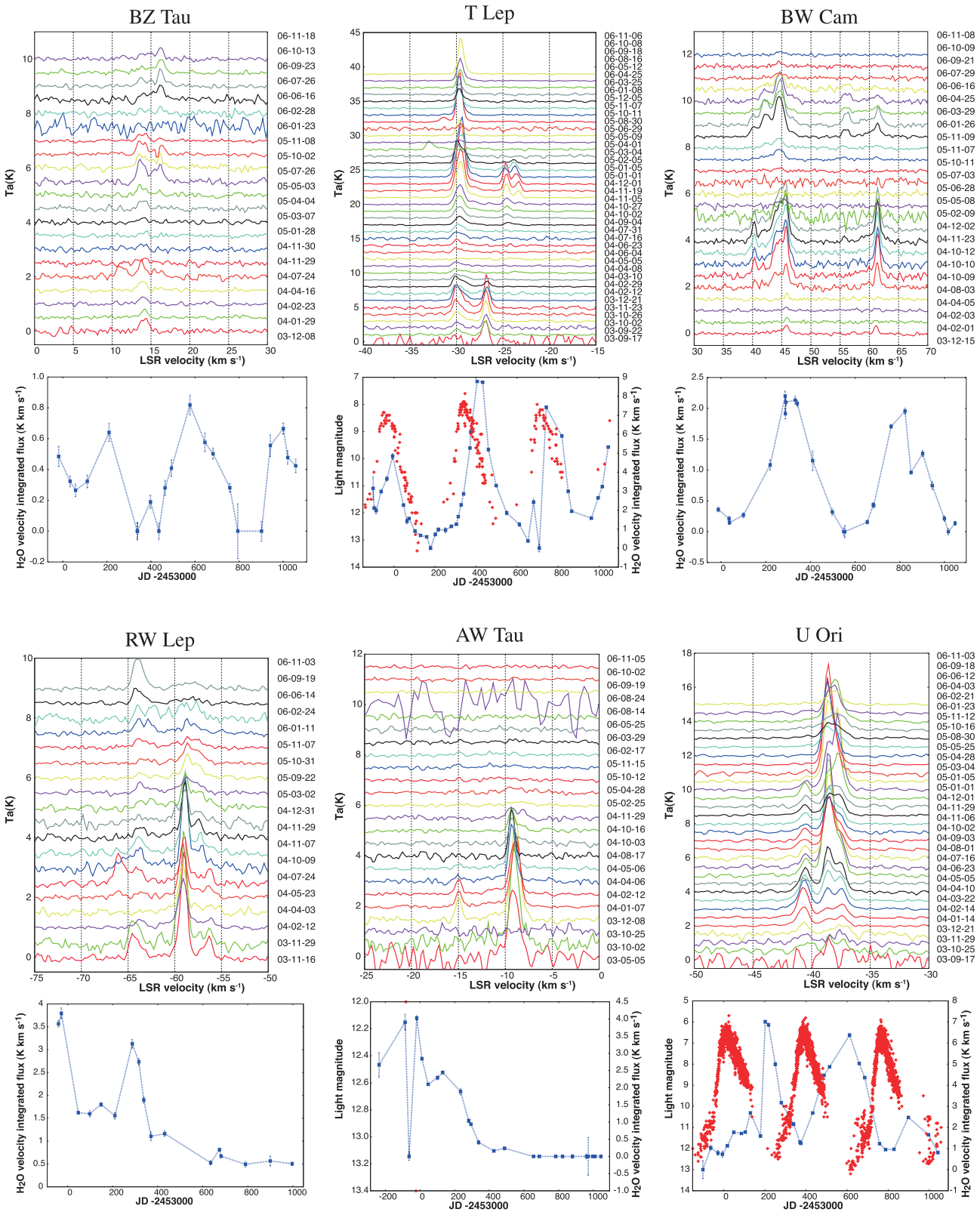

Fig. 7. (Continued)

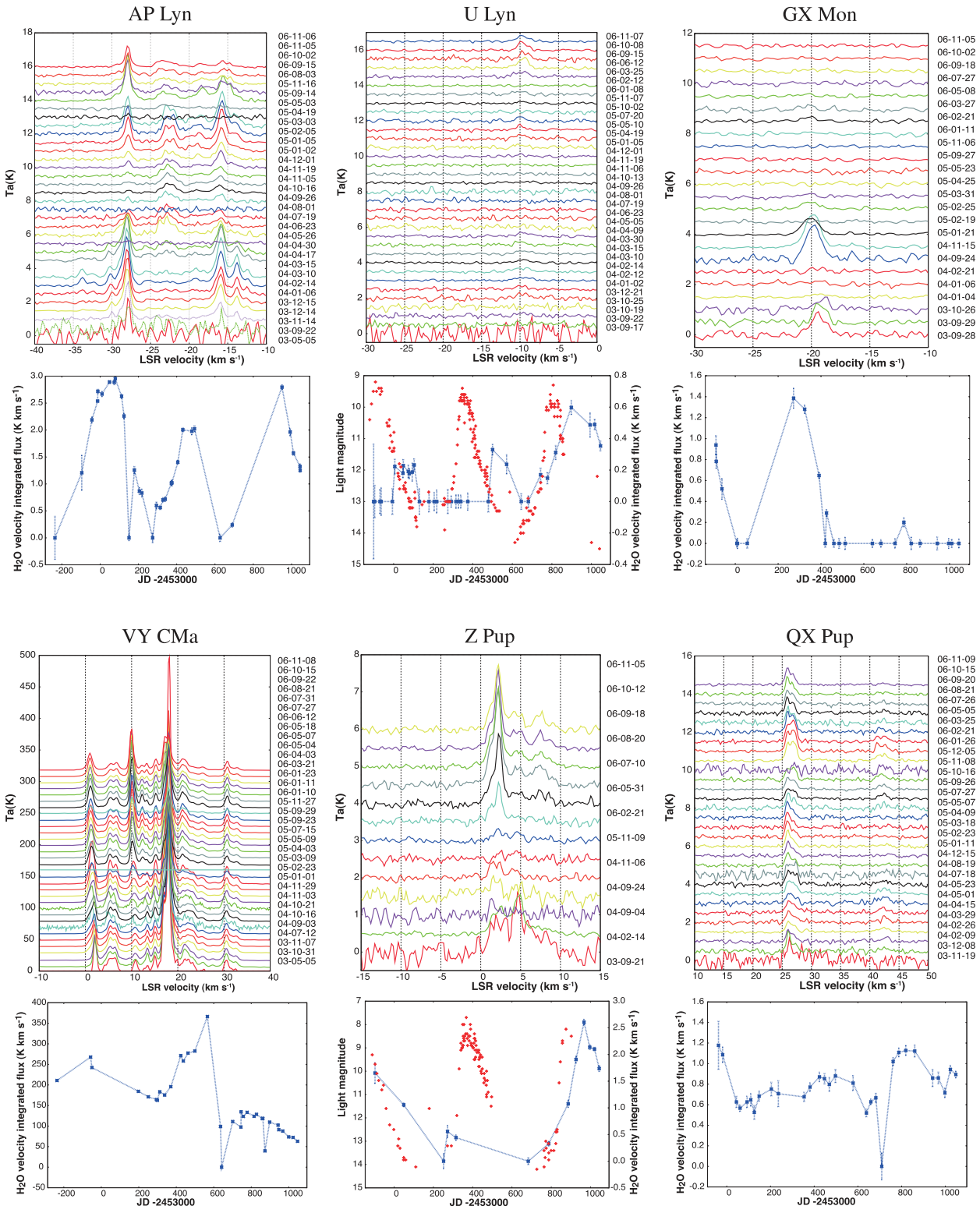

Fig. 7. (Continued)

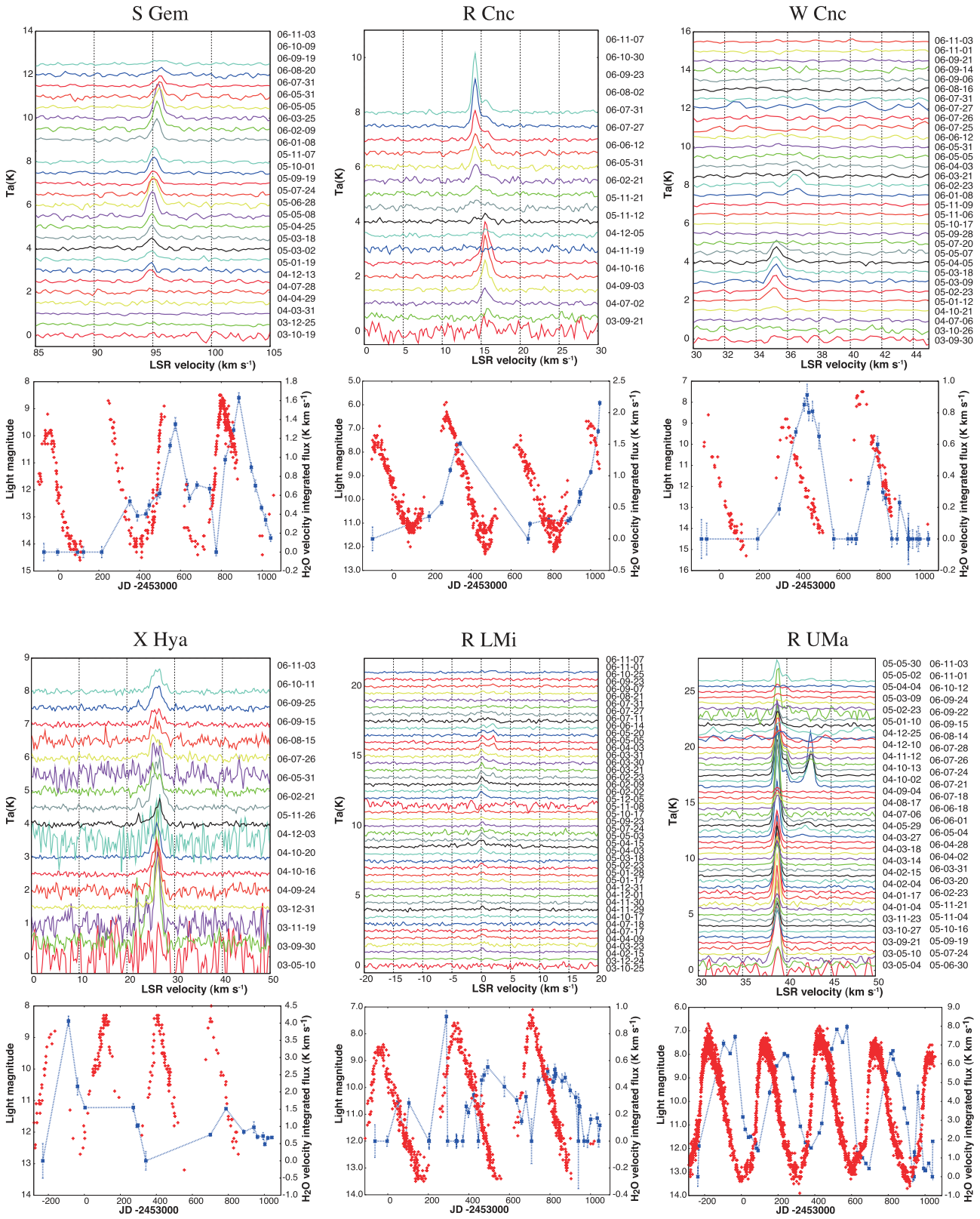

Fig. 7. (Continued)

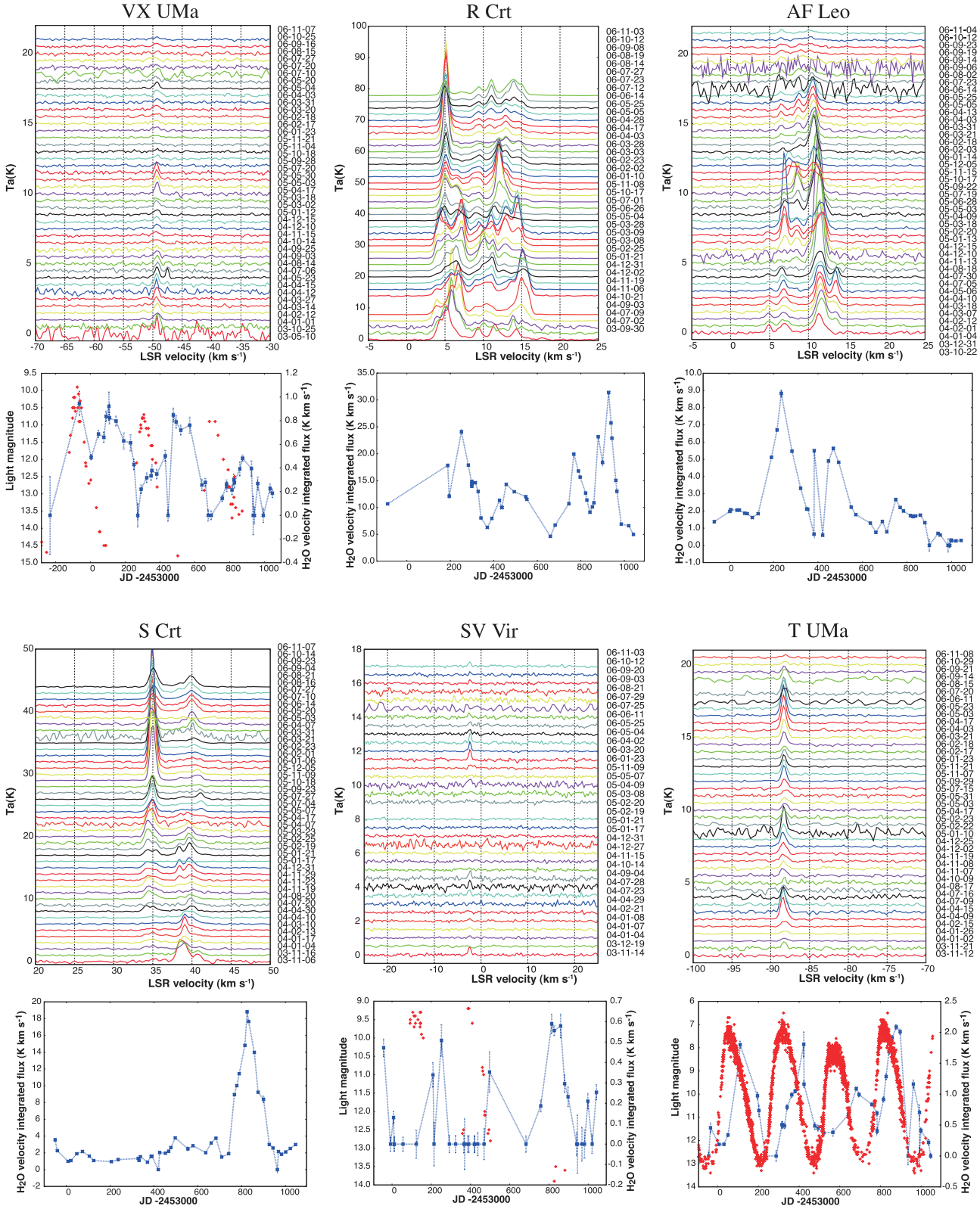

Fig. 7. (Continued)

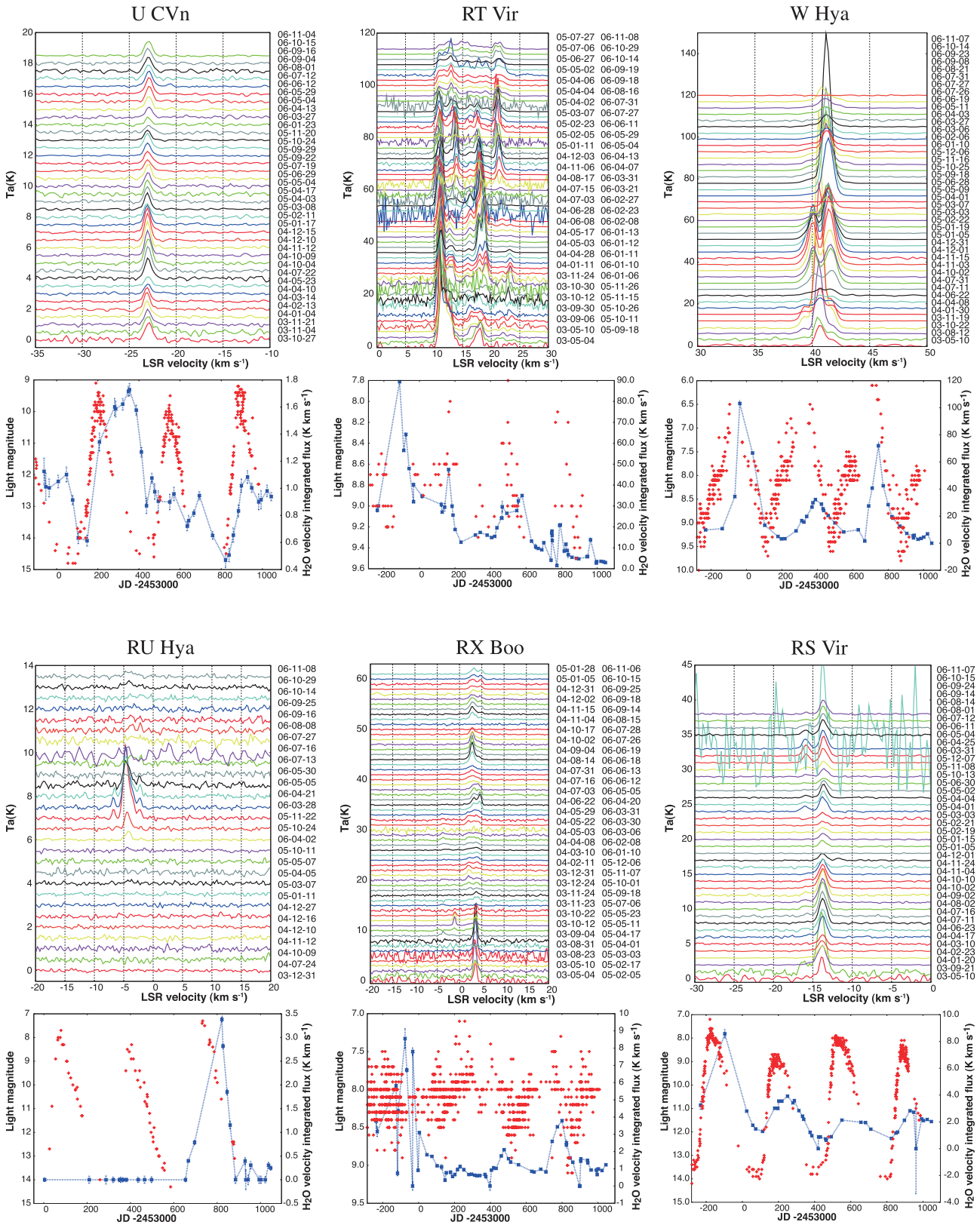

Fig. 7. (Continued)

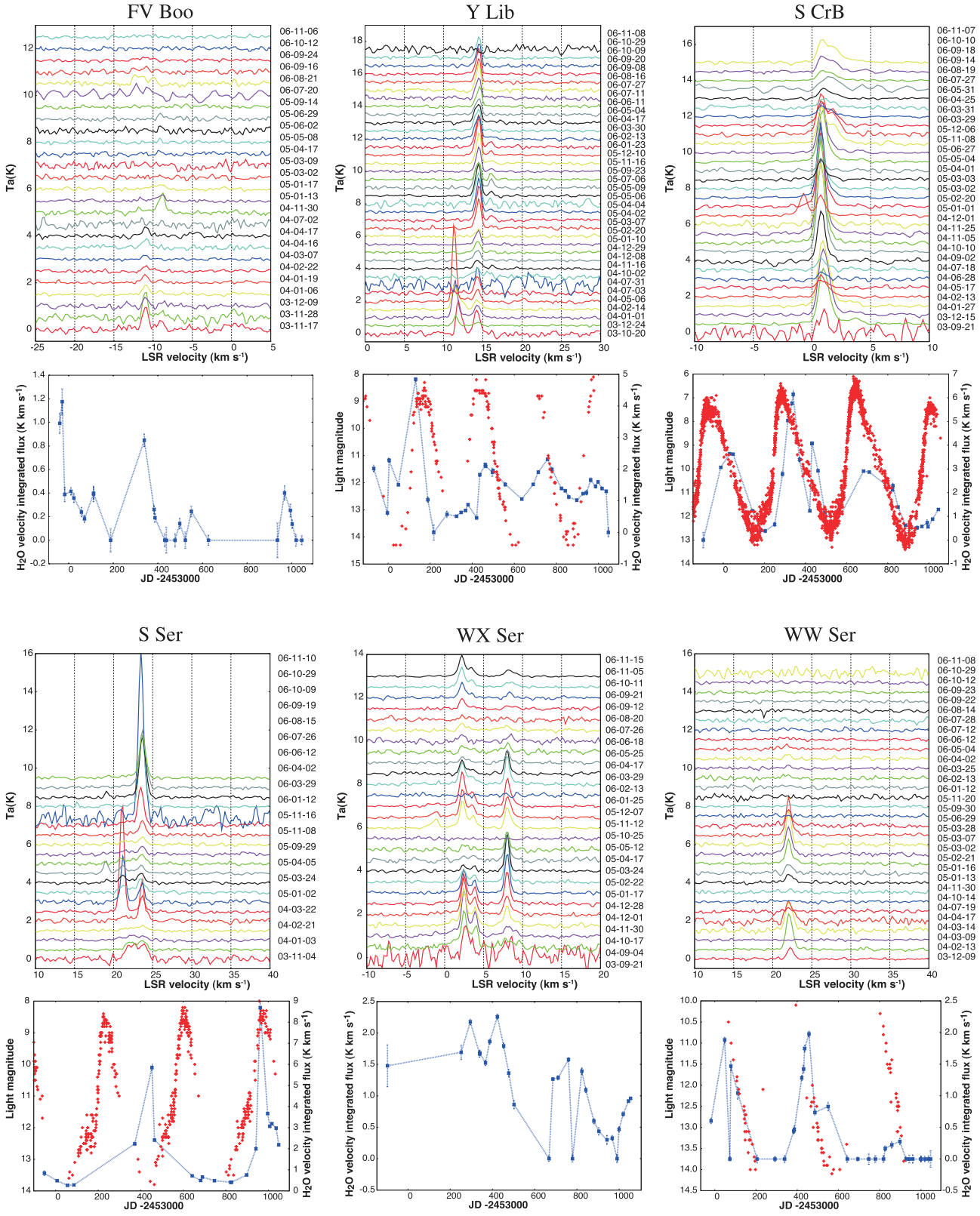

Fig. 7. (Continued)

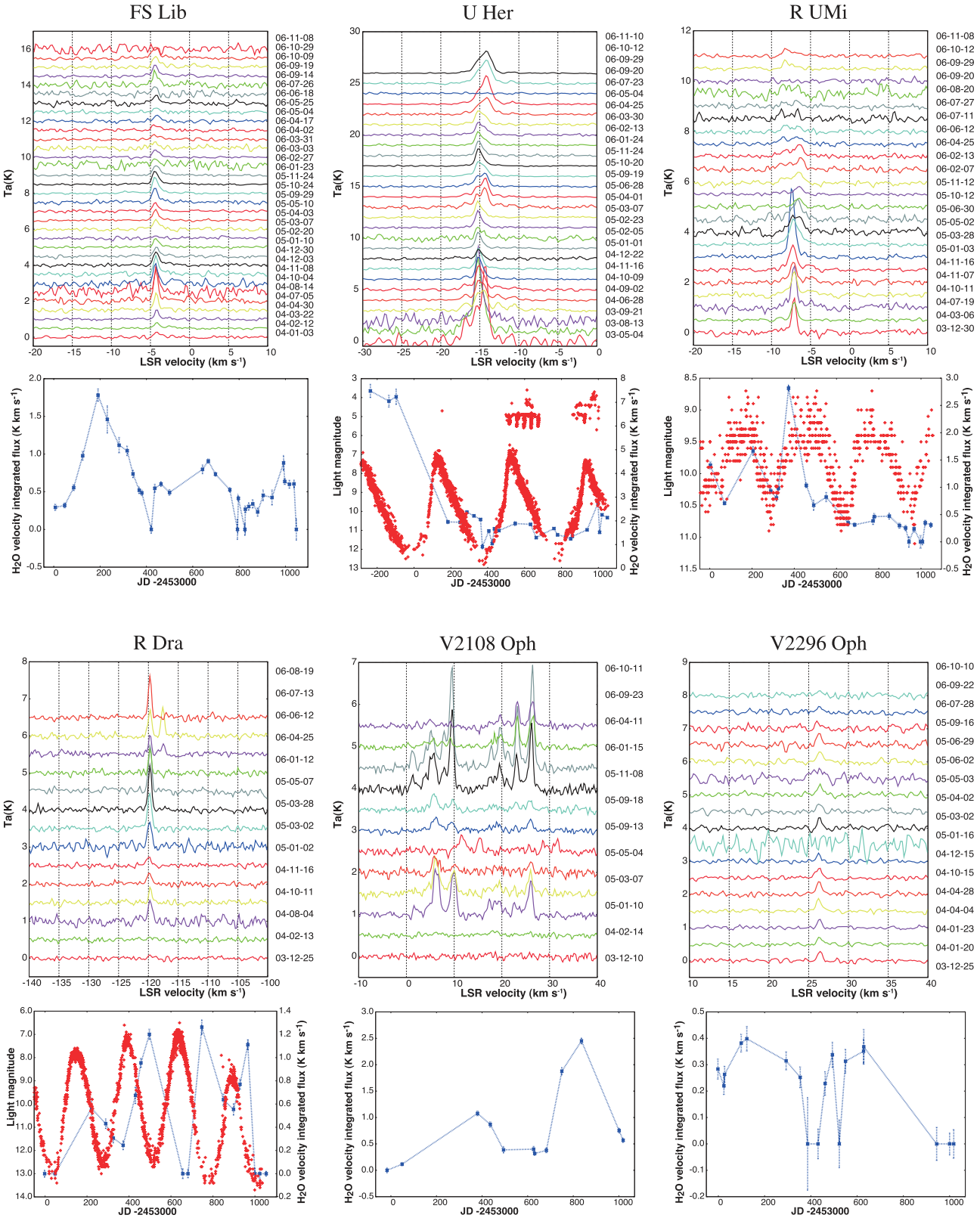

Fig. 7. (Continued)

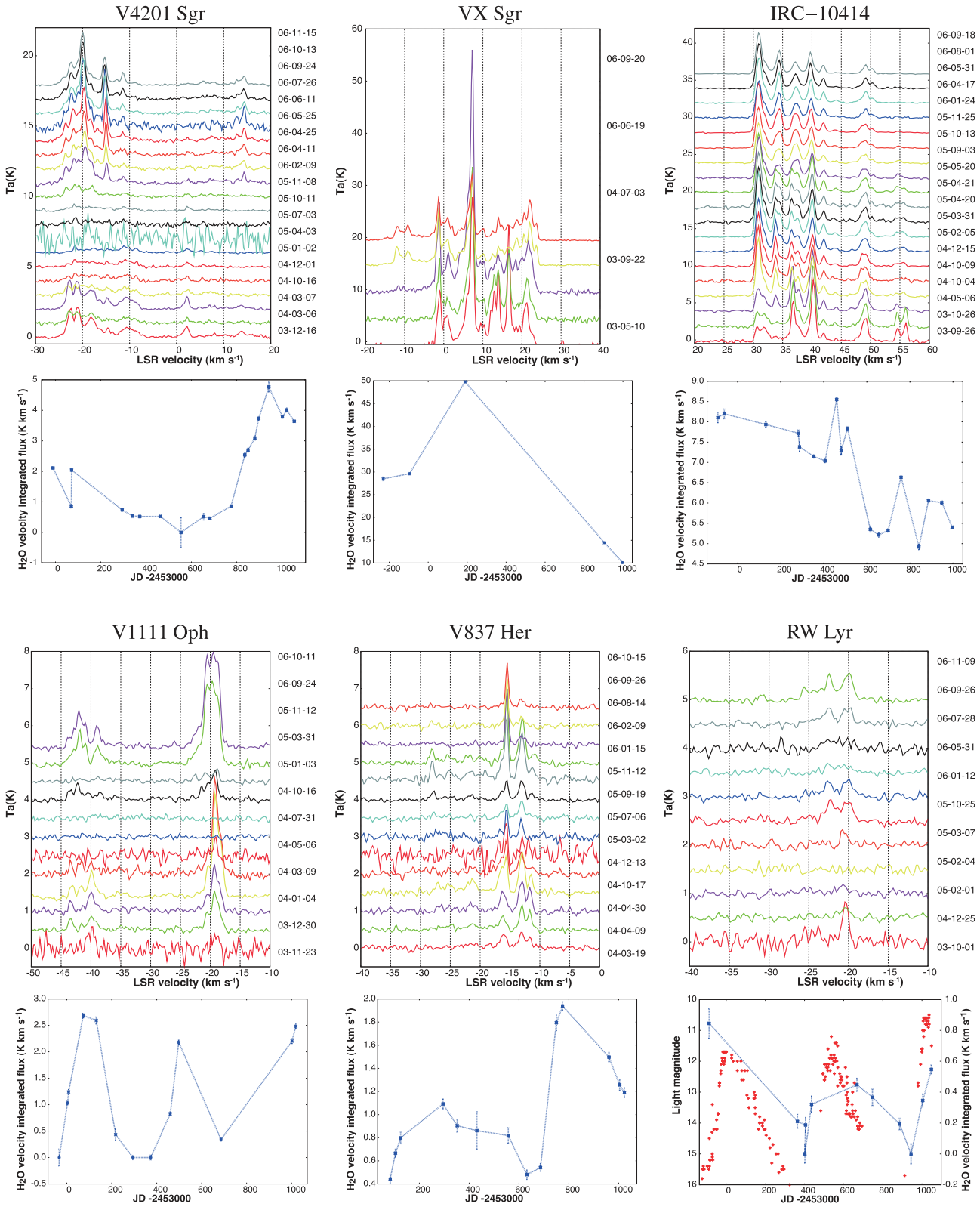

Fig. 7. (Continued)

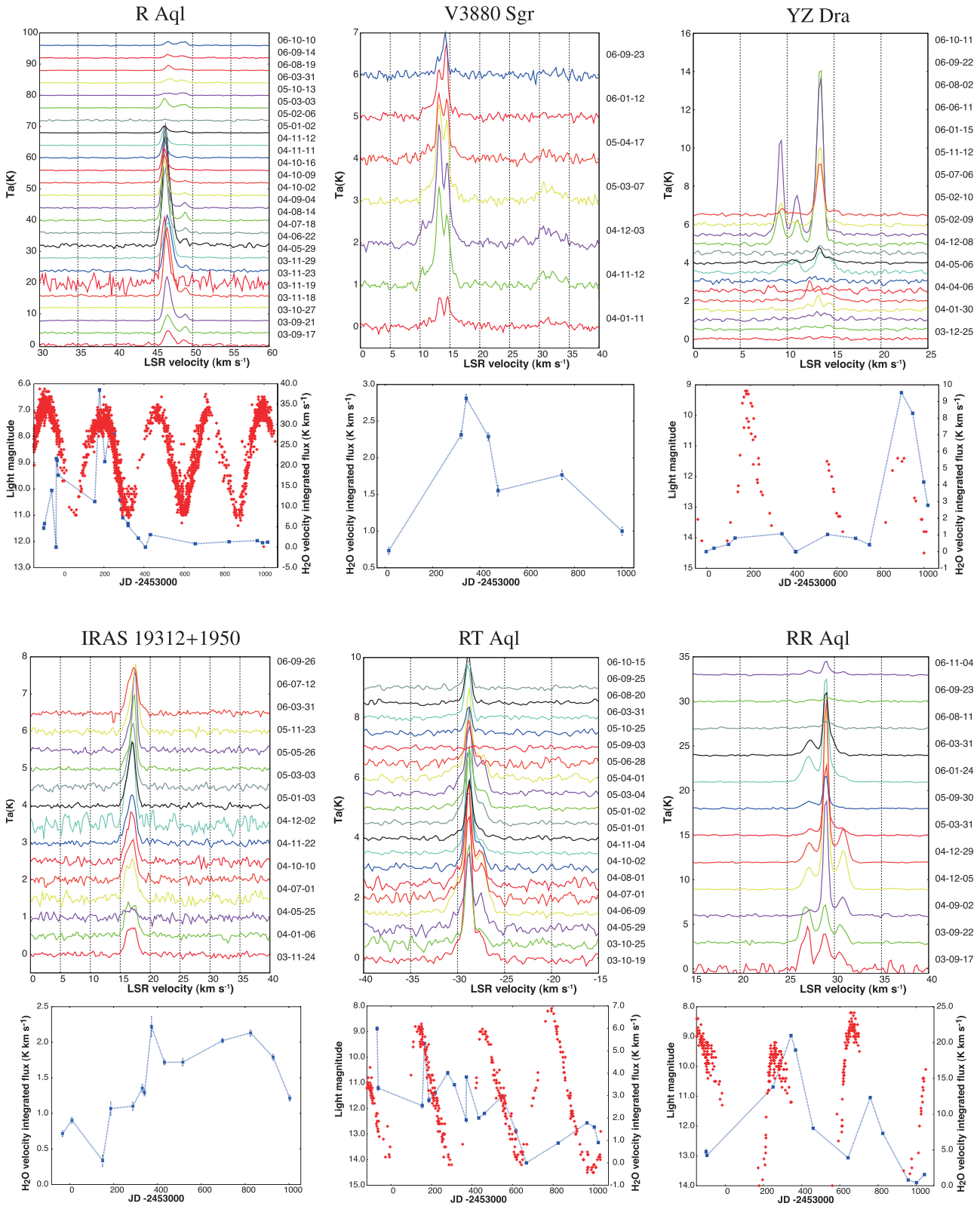

Fig. 7. (Continued)

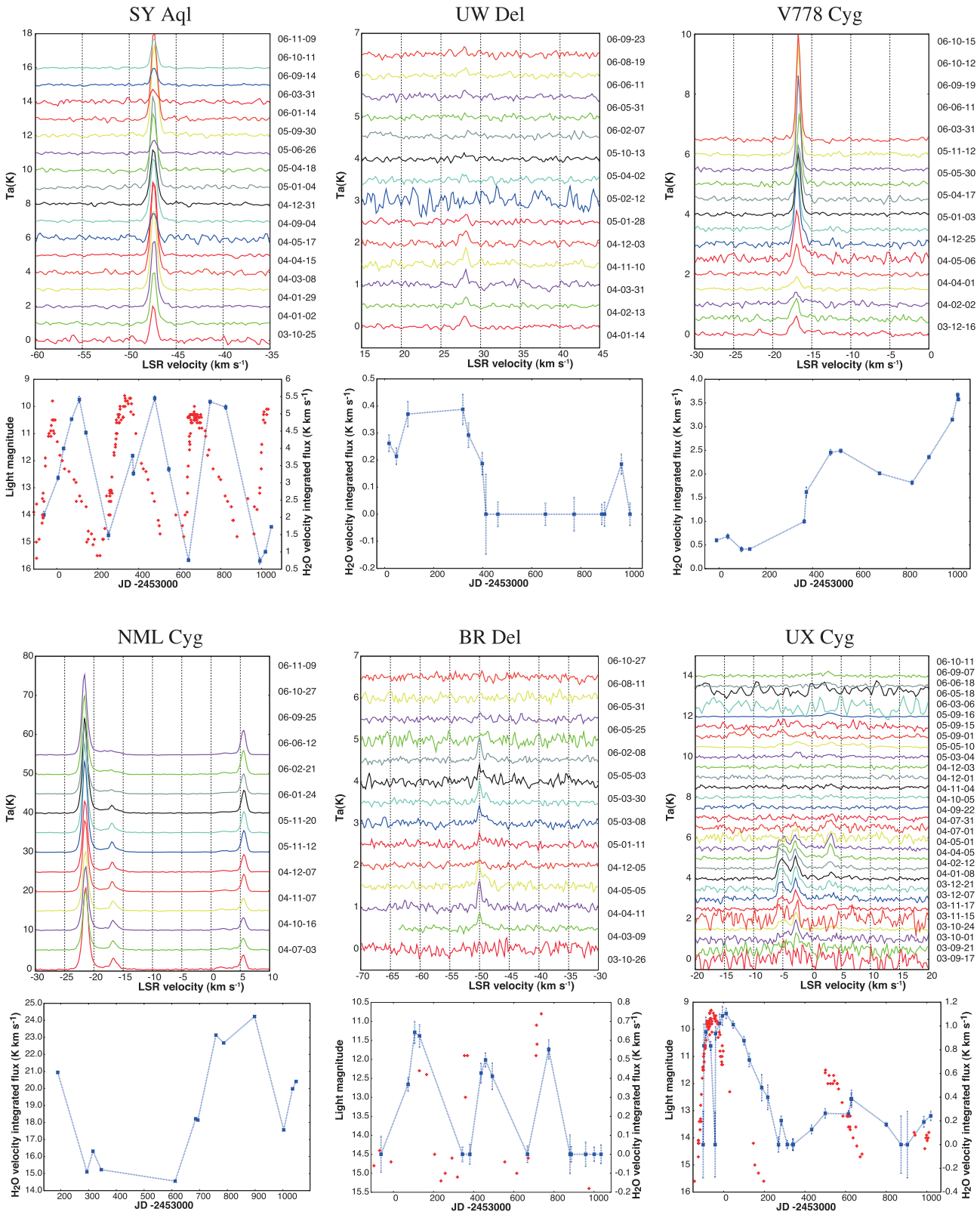

Fig. 7. (Continued)

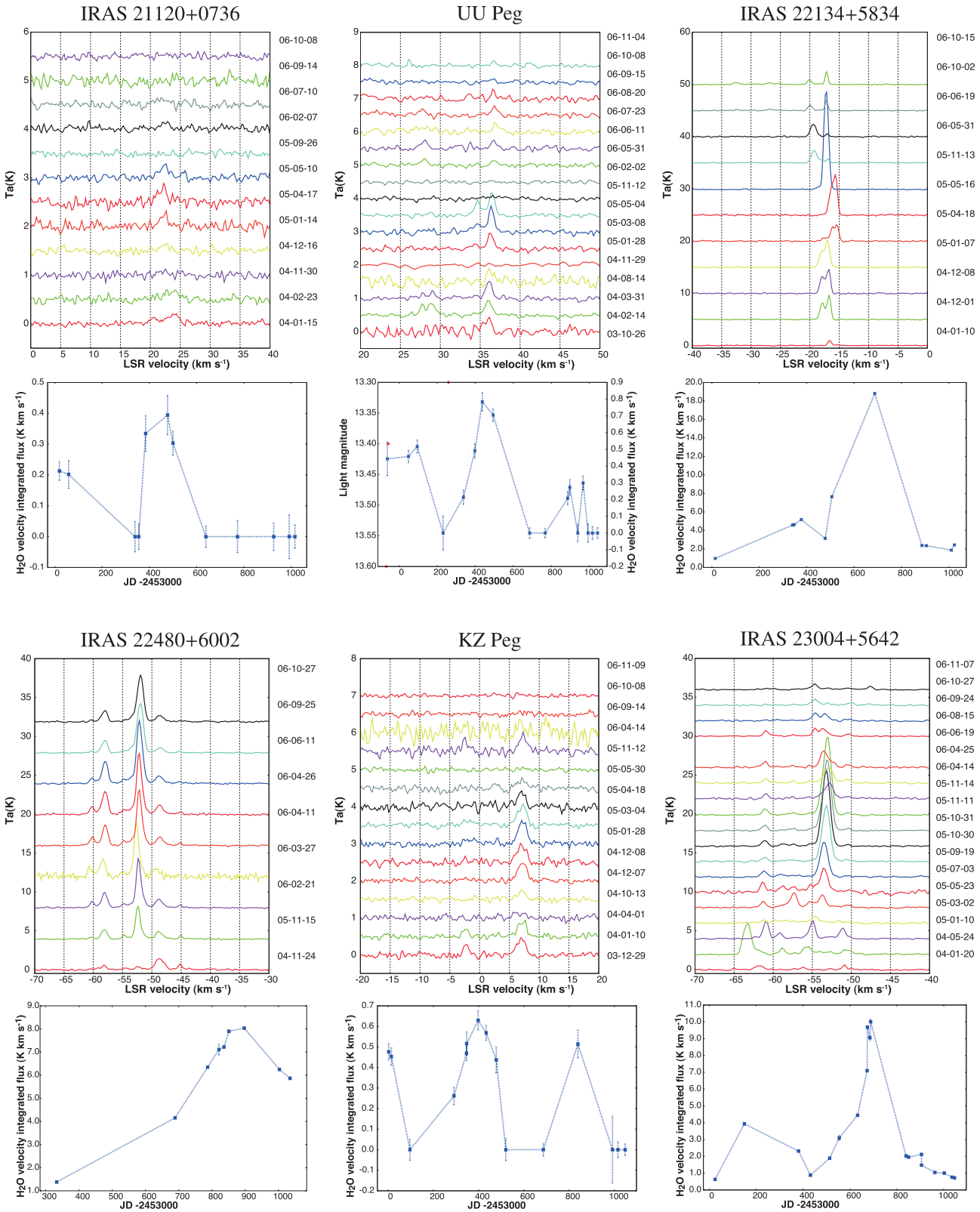

Fig. 7. (Continued)

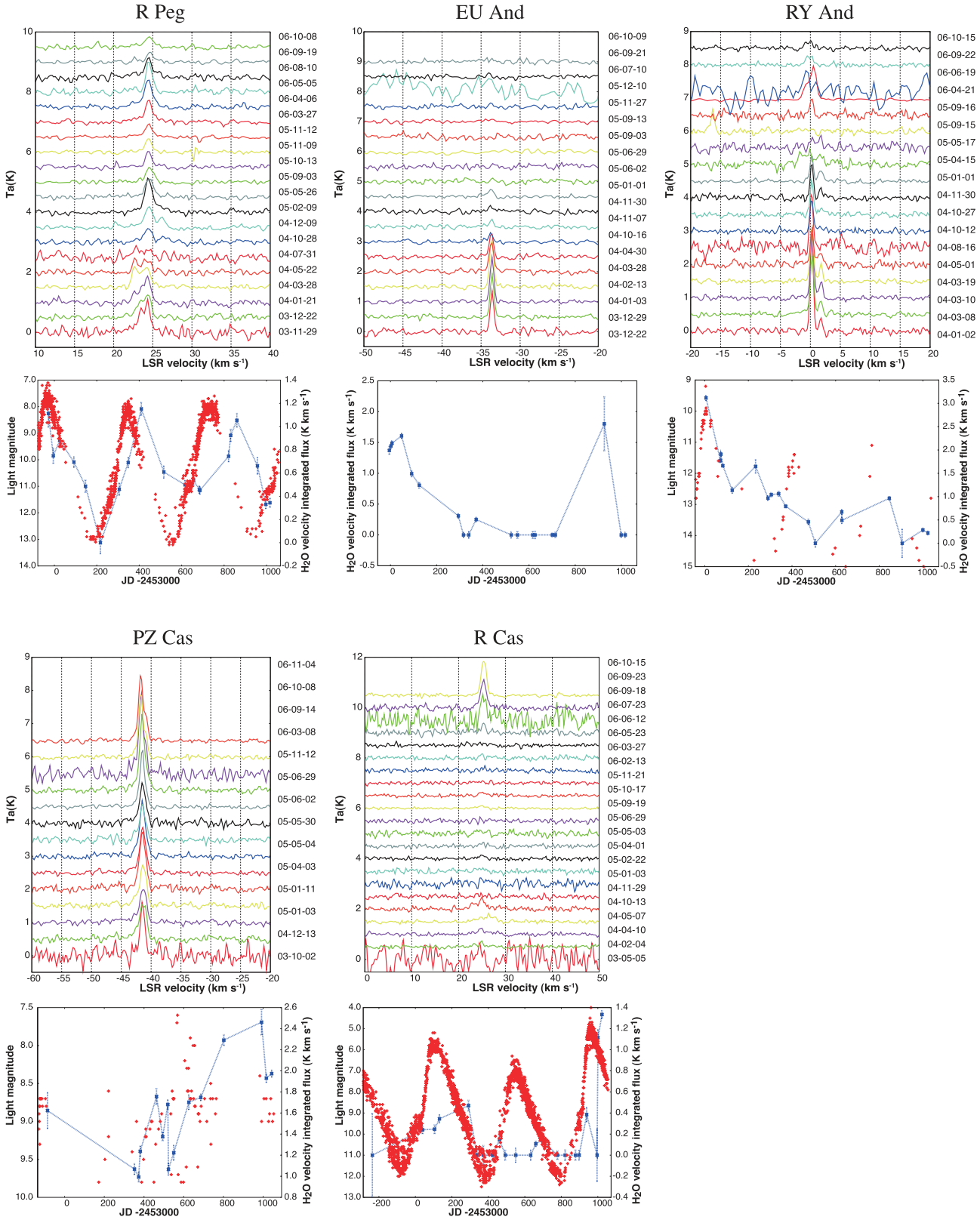

Fig. 7. (Continued)

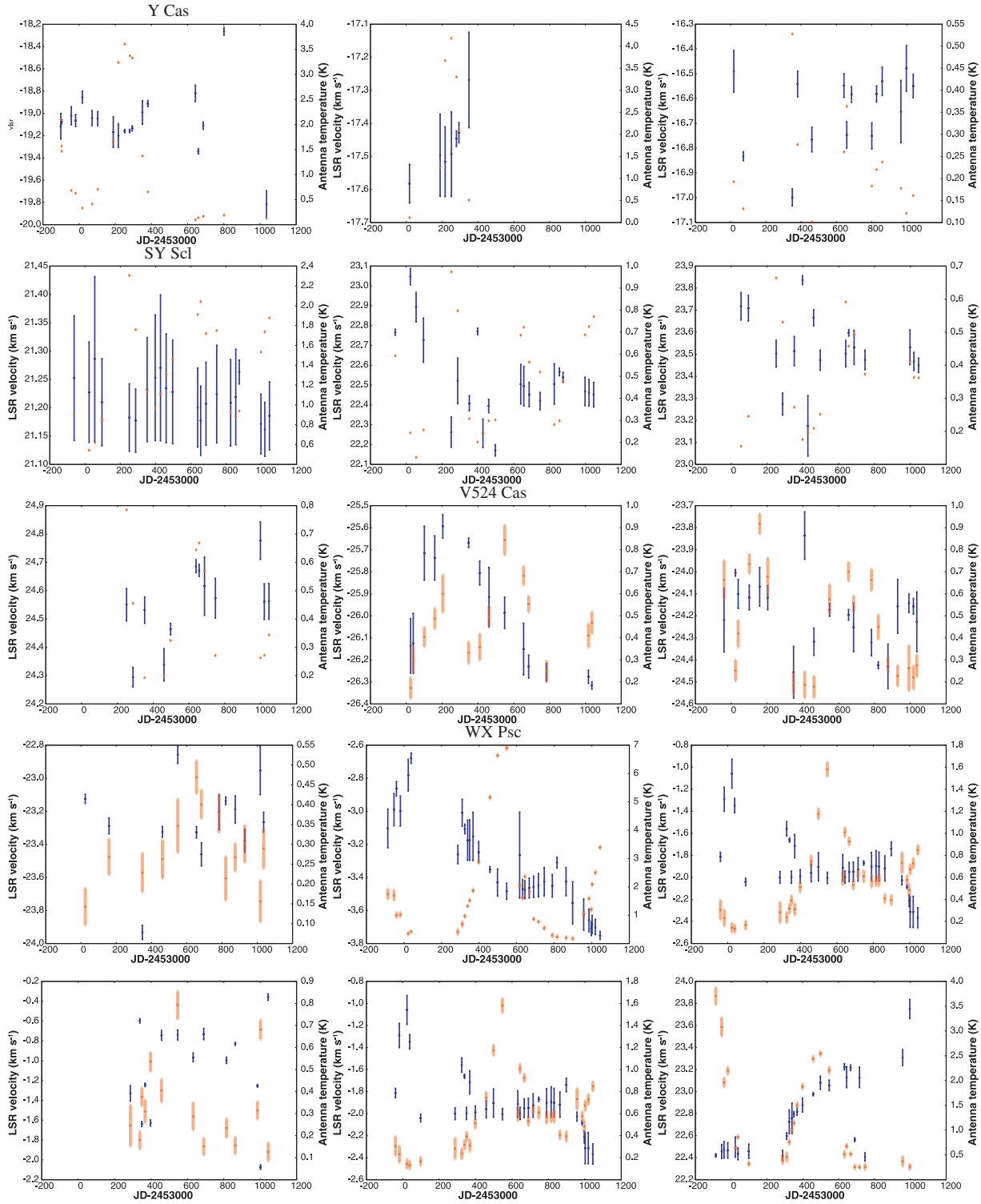

Fig. 8. Time variation of the peak antenna temperature (opened circle with a gray line error bar) and the LSR velocity at the peak (asterisk with a solid line bar) of each spectral peak. Panels for a star correspond to ID's in table 5.

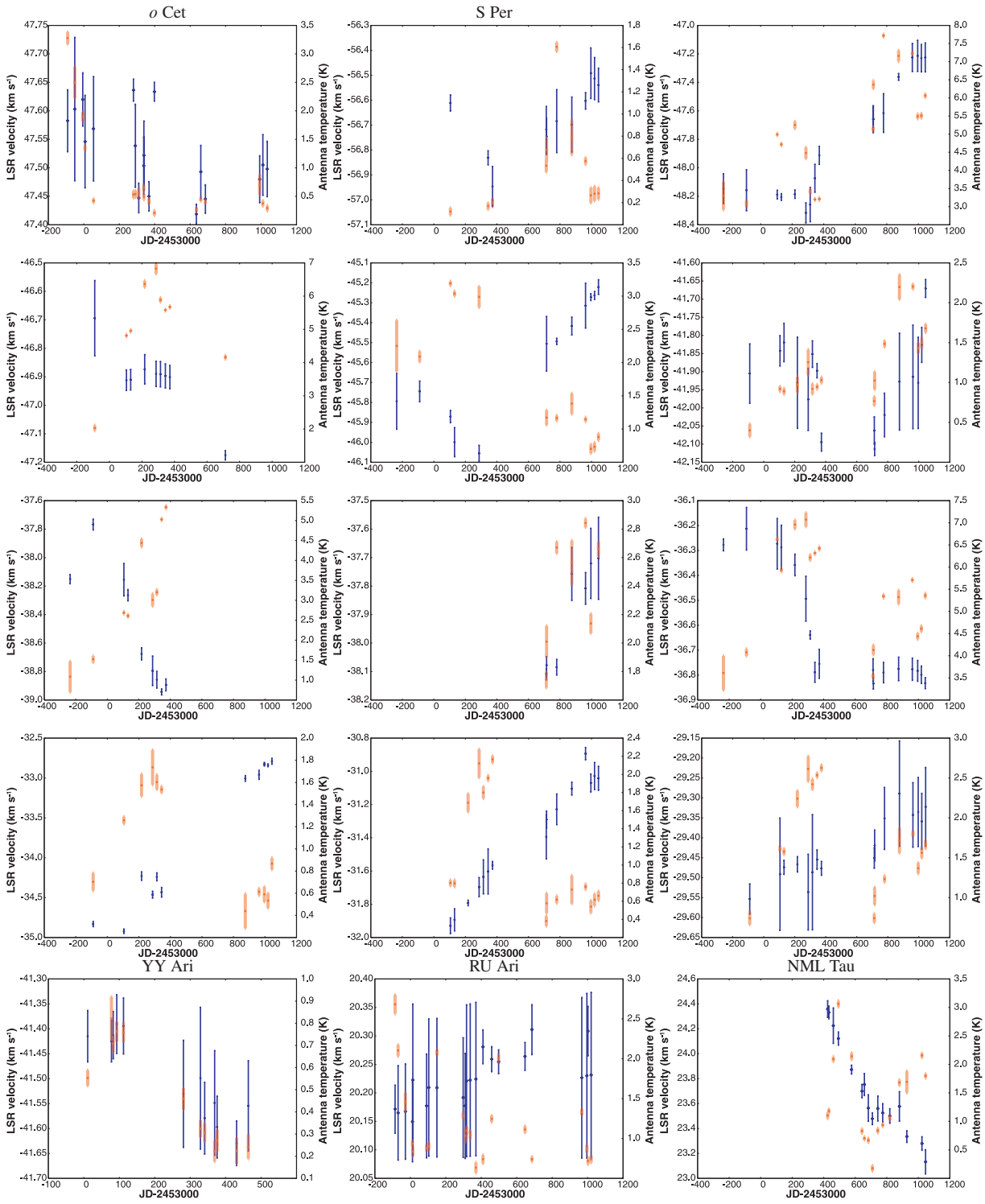

Fig. 8. (Continued)

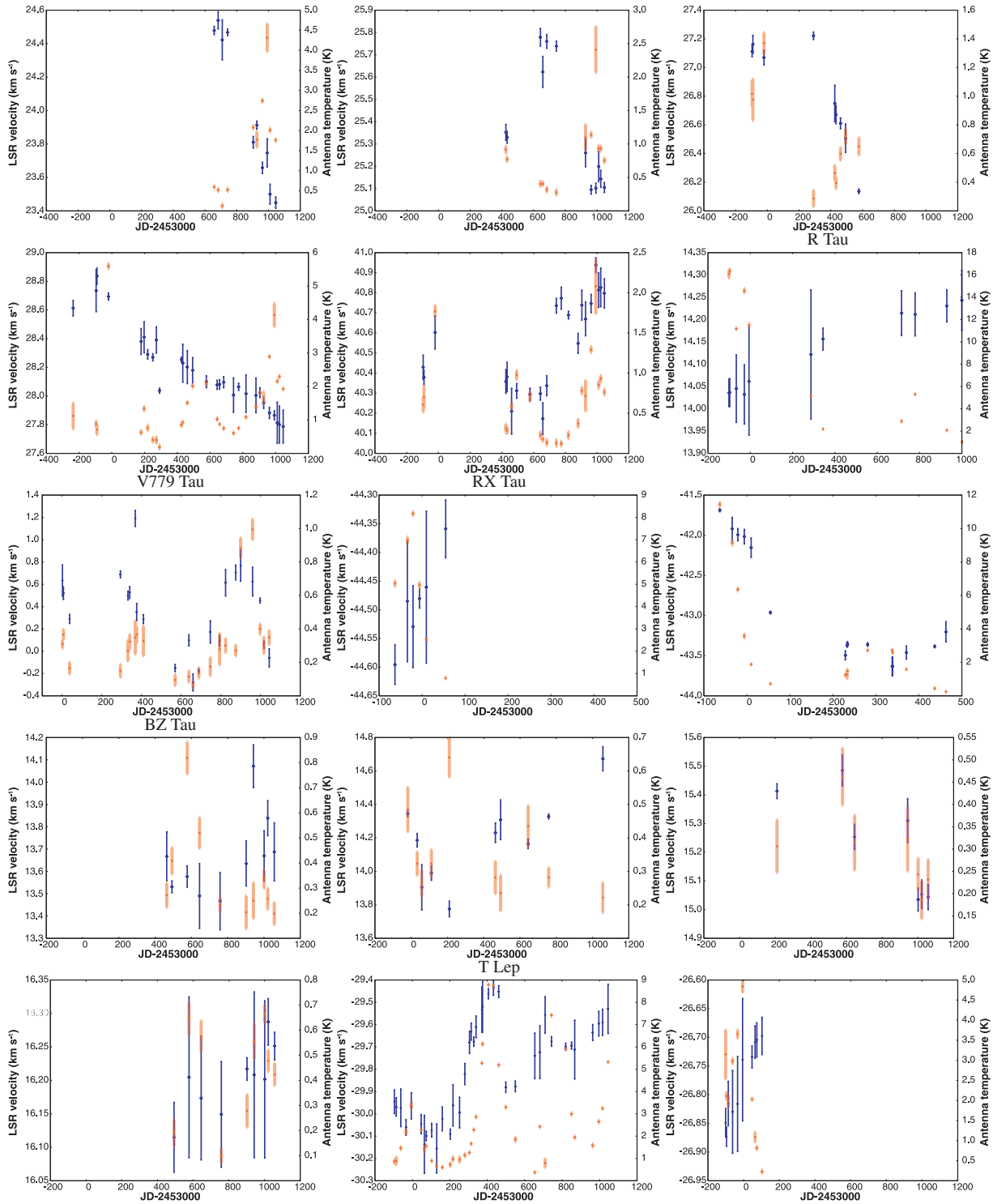

Fig. 8. (Continued)

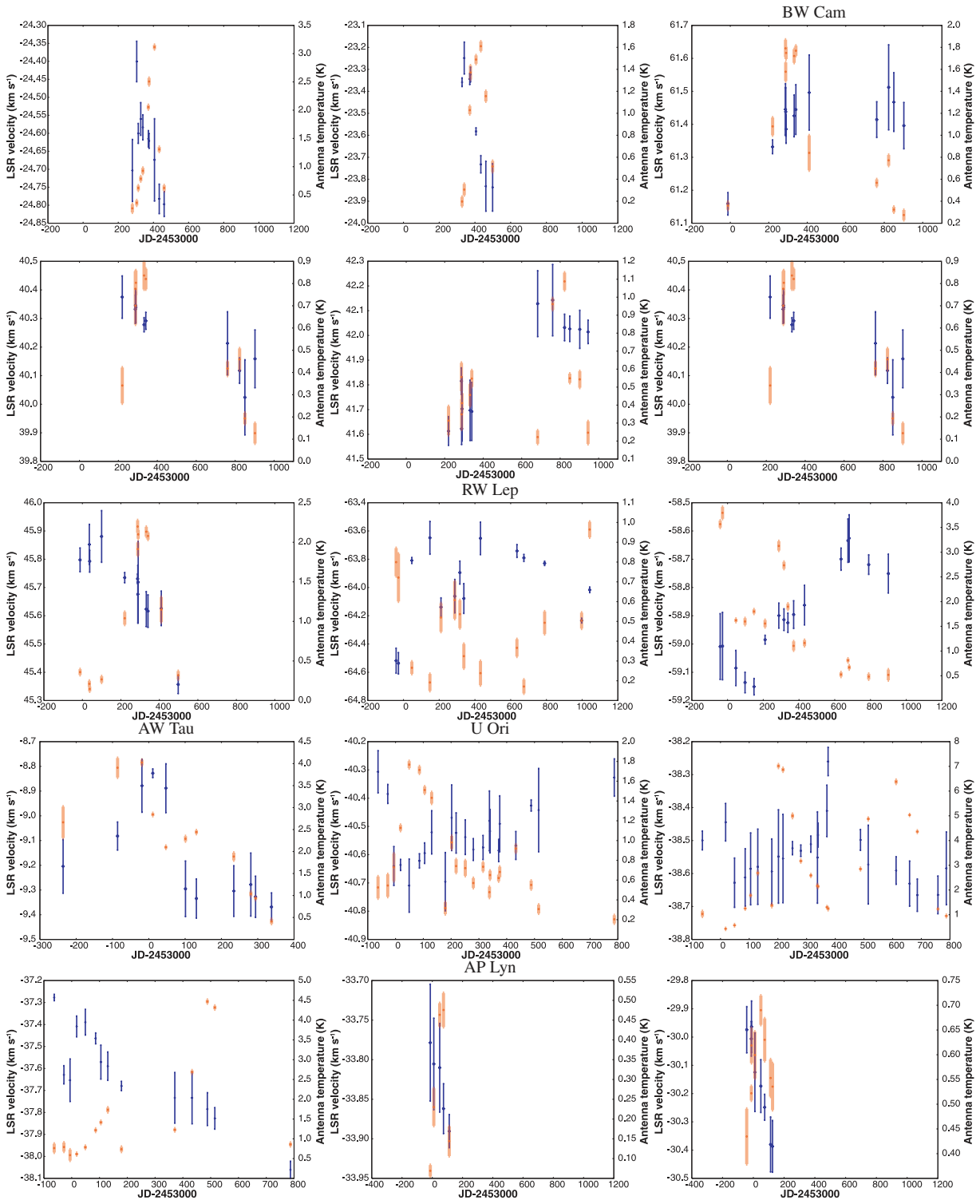

Fig. 8. (Continued)

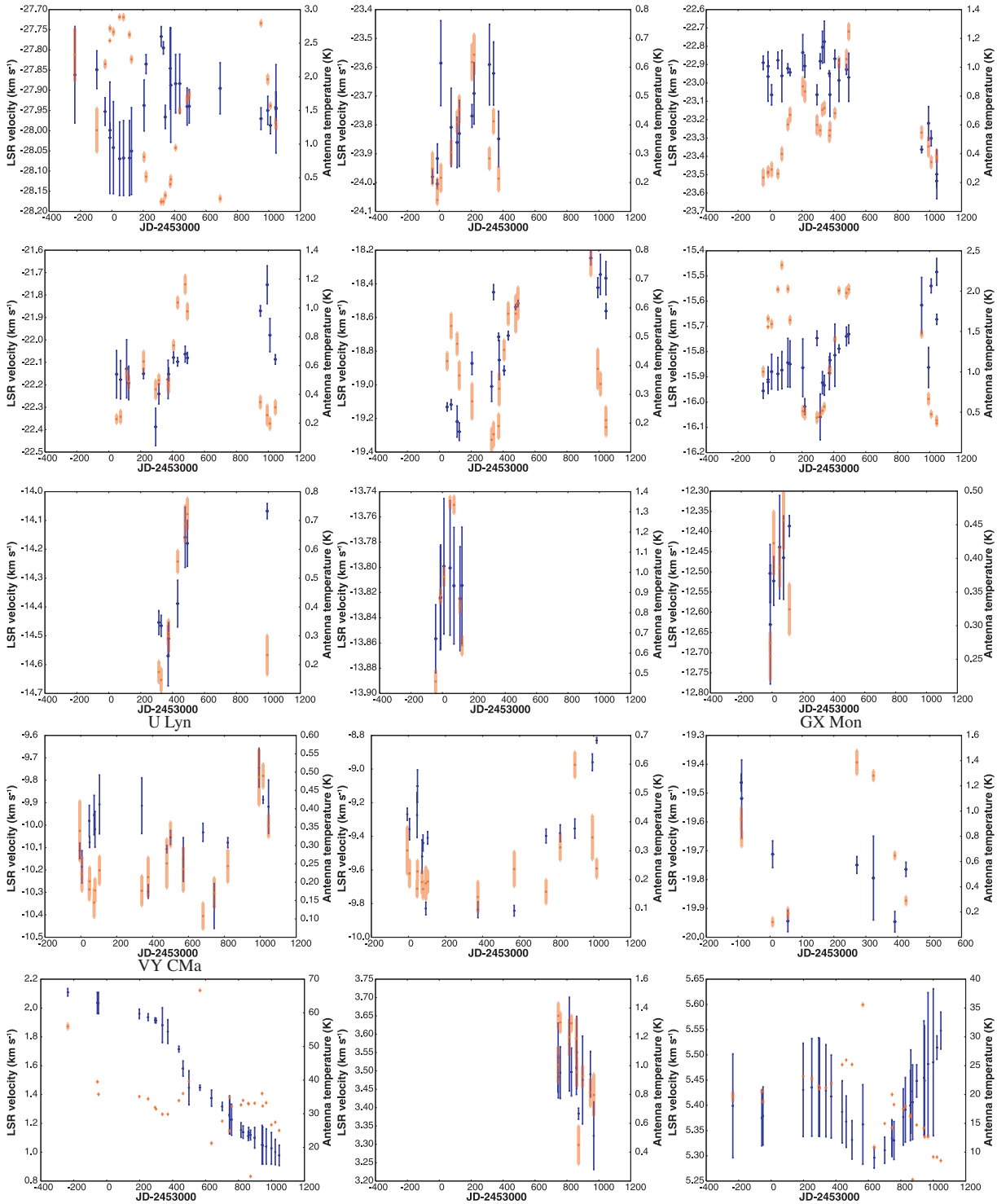

Fig. 8. (Continued)

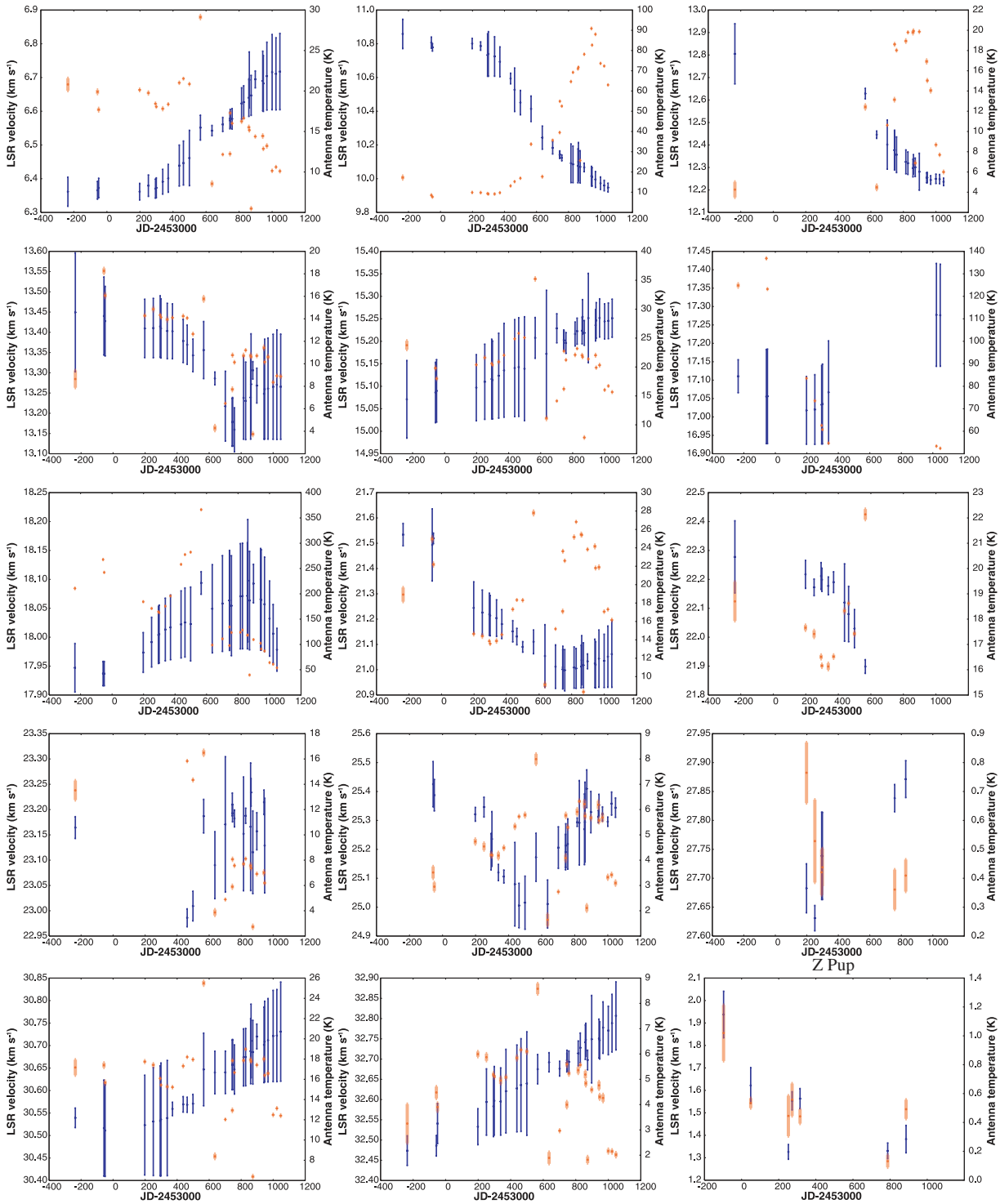

Fig. 8. (Continued)

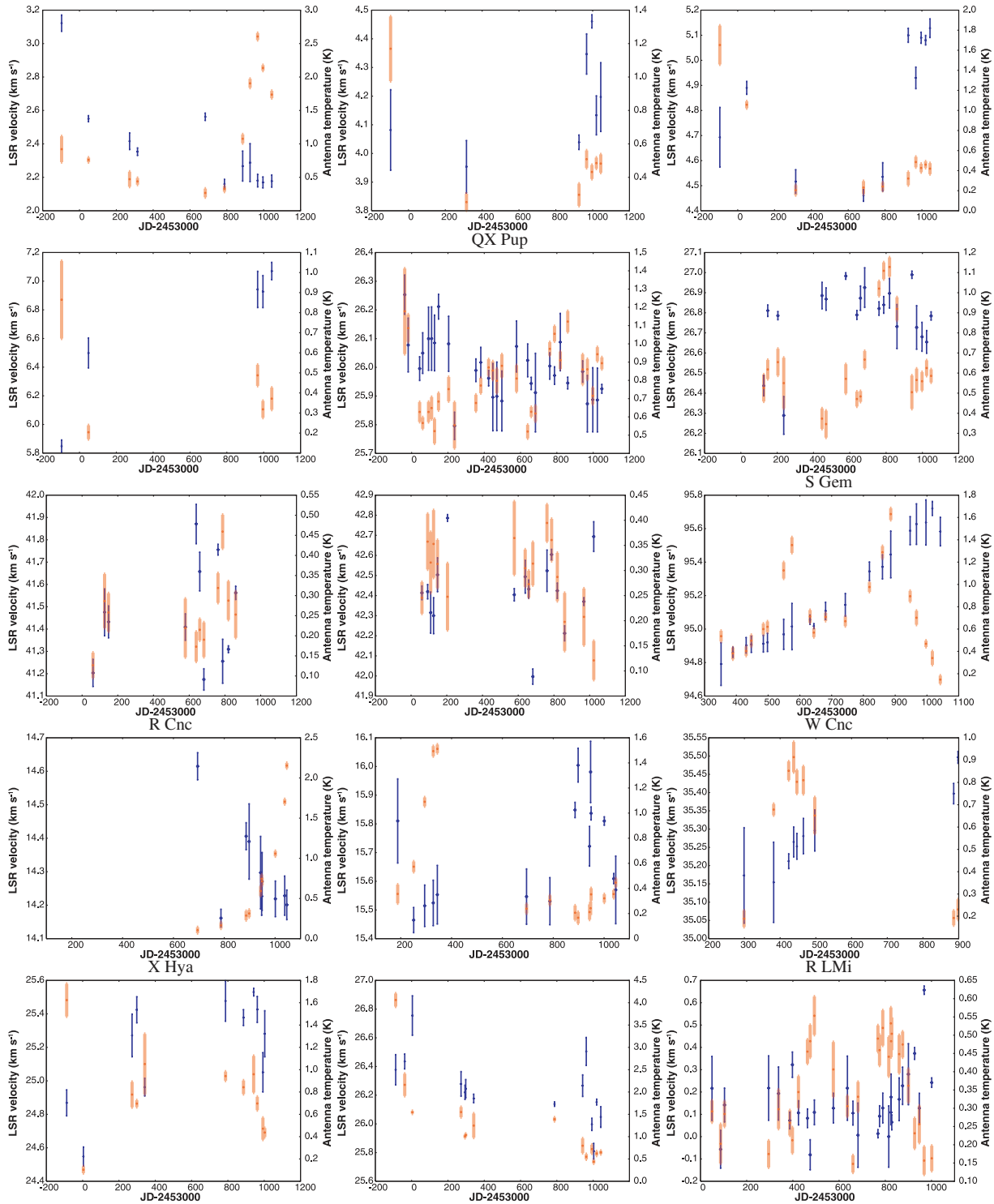

Fig. 8. (Continued)

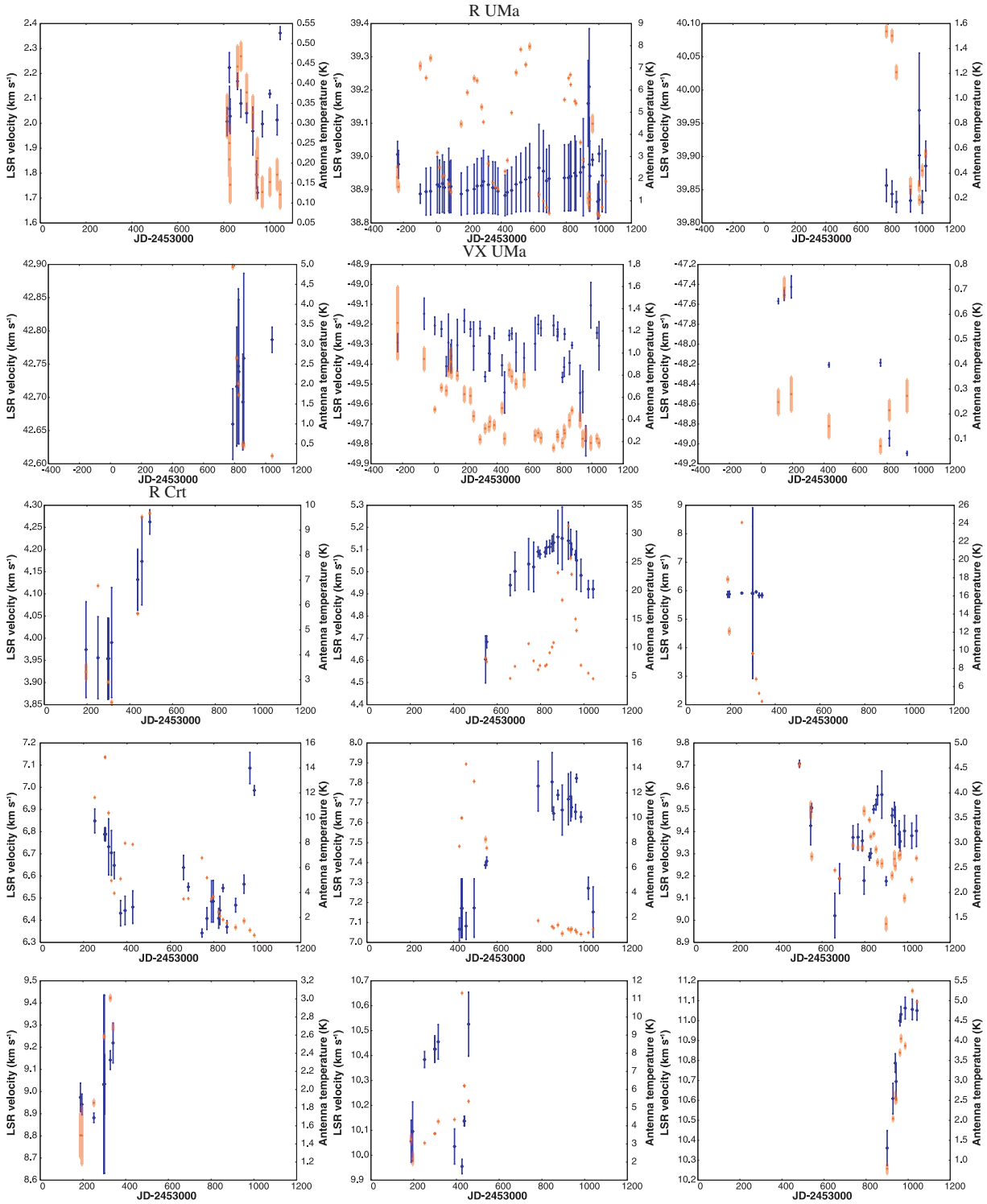

Fig. 8. (Continued)

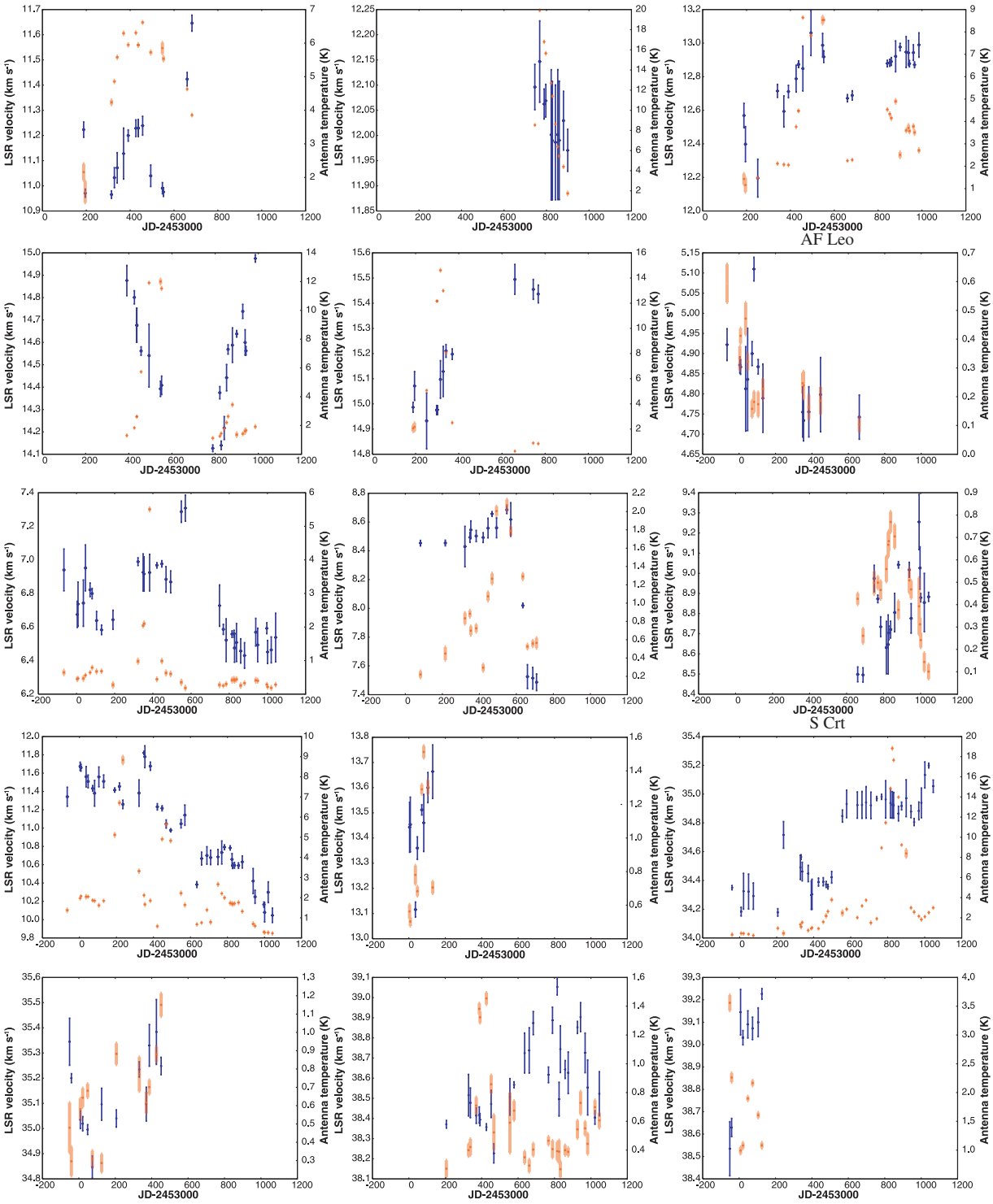

Fig. 8. (Continued)

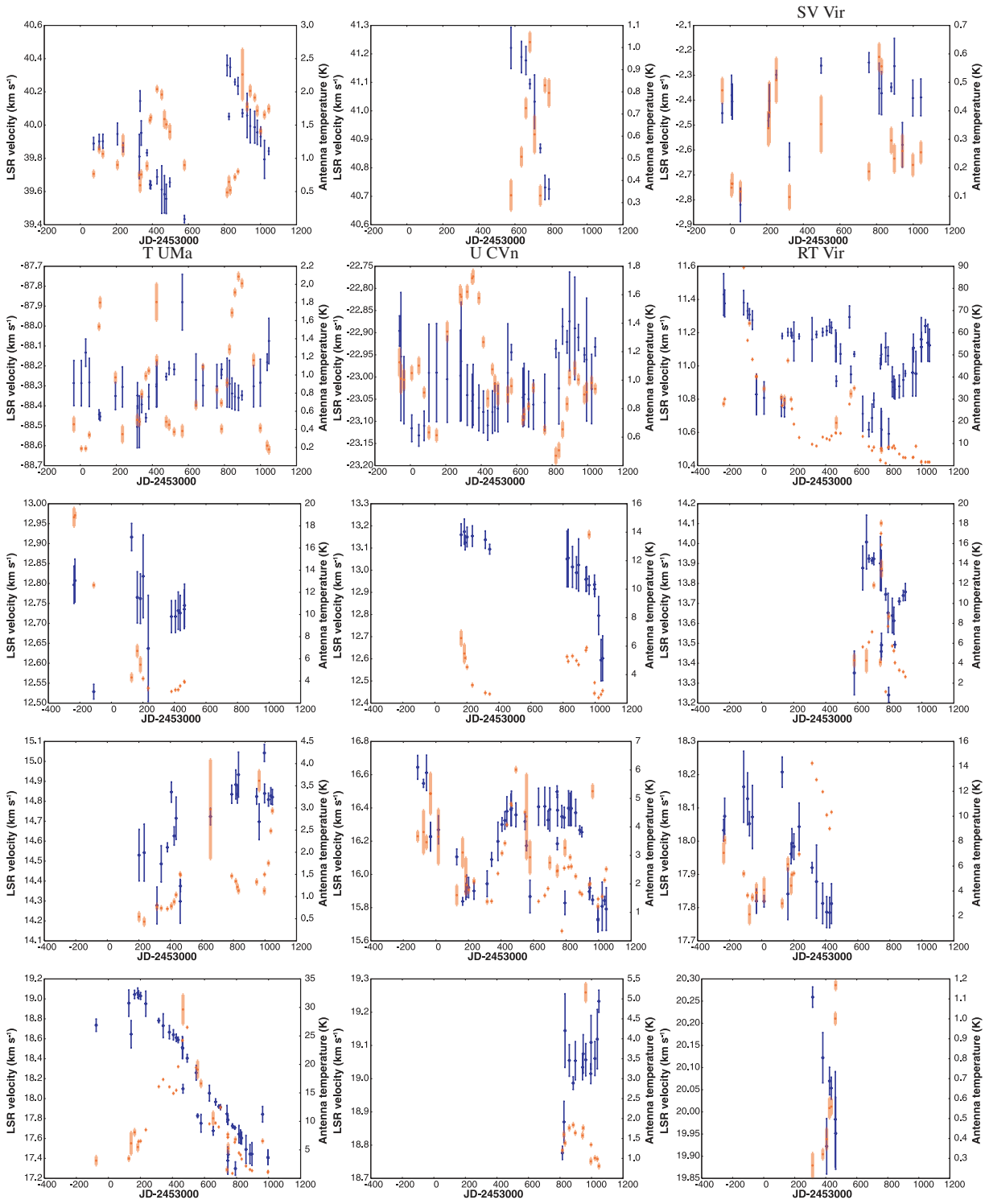

Fig. 8. (Continued)

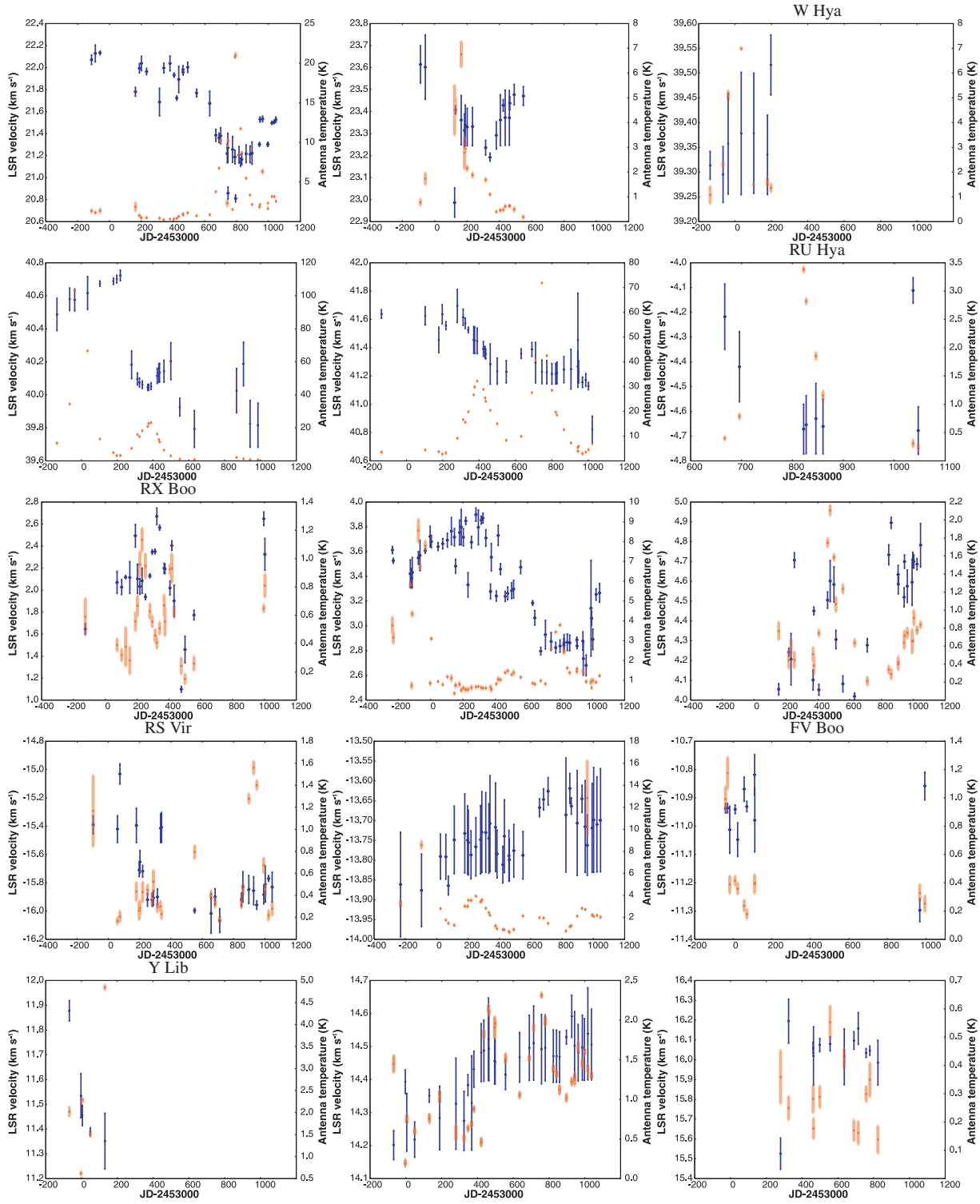

Fig. 8. (Continued)

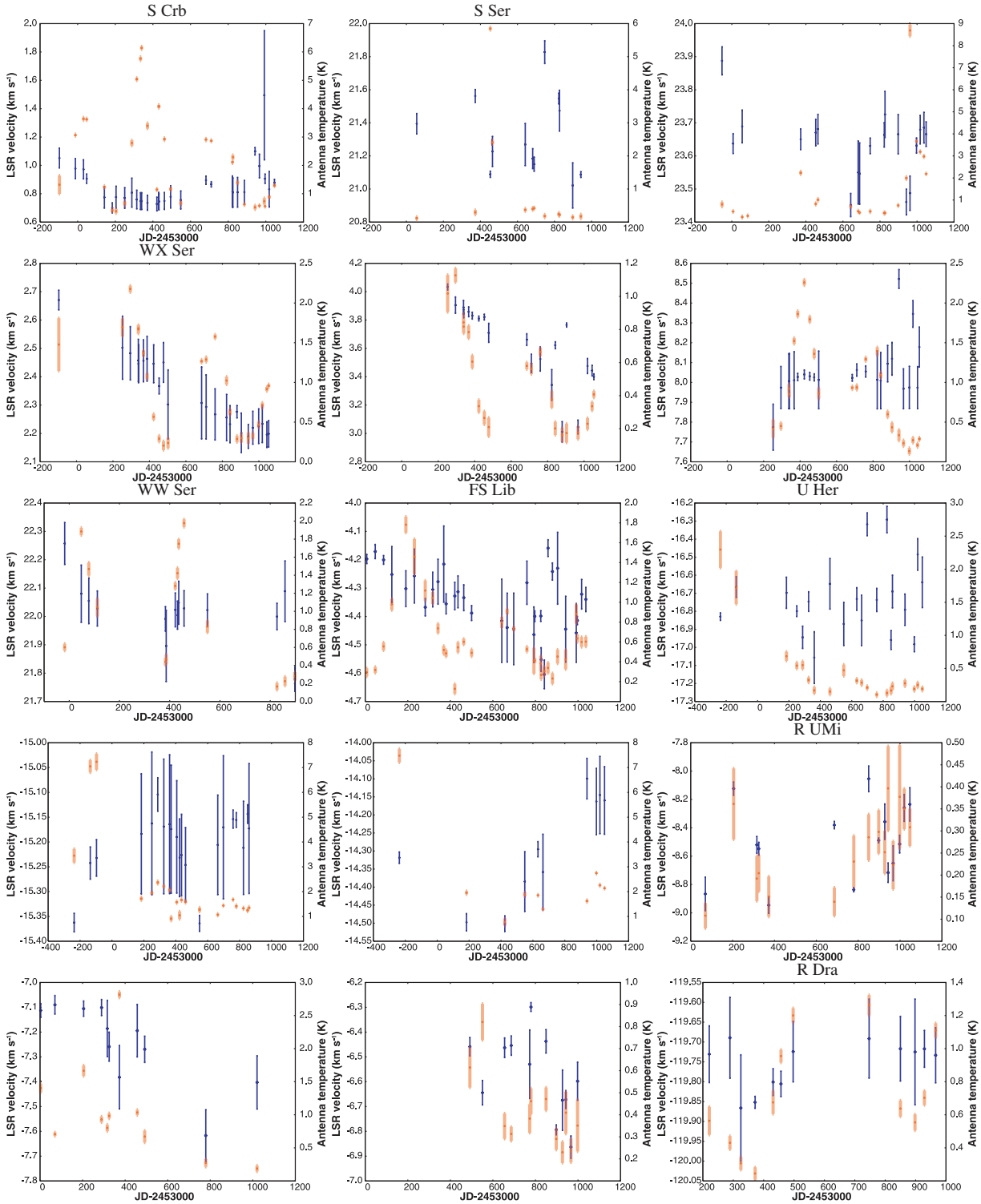

Fig. 8. (Continued)

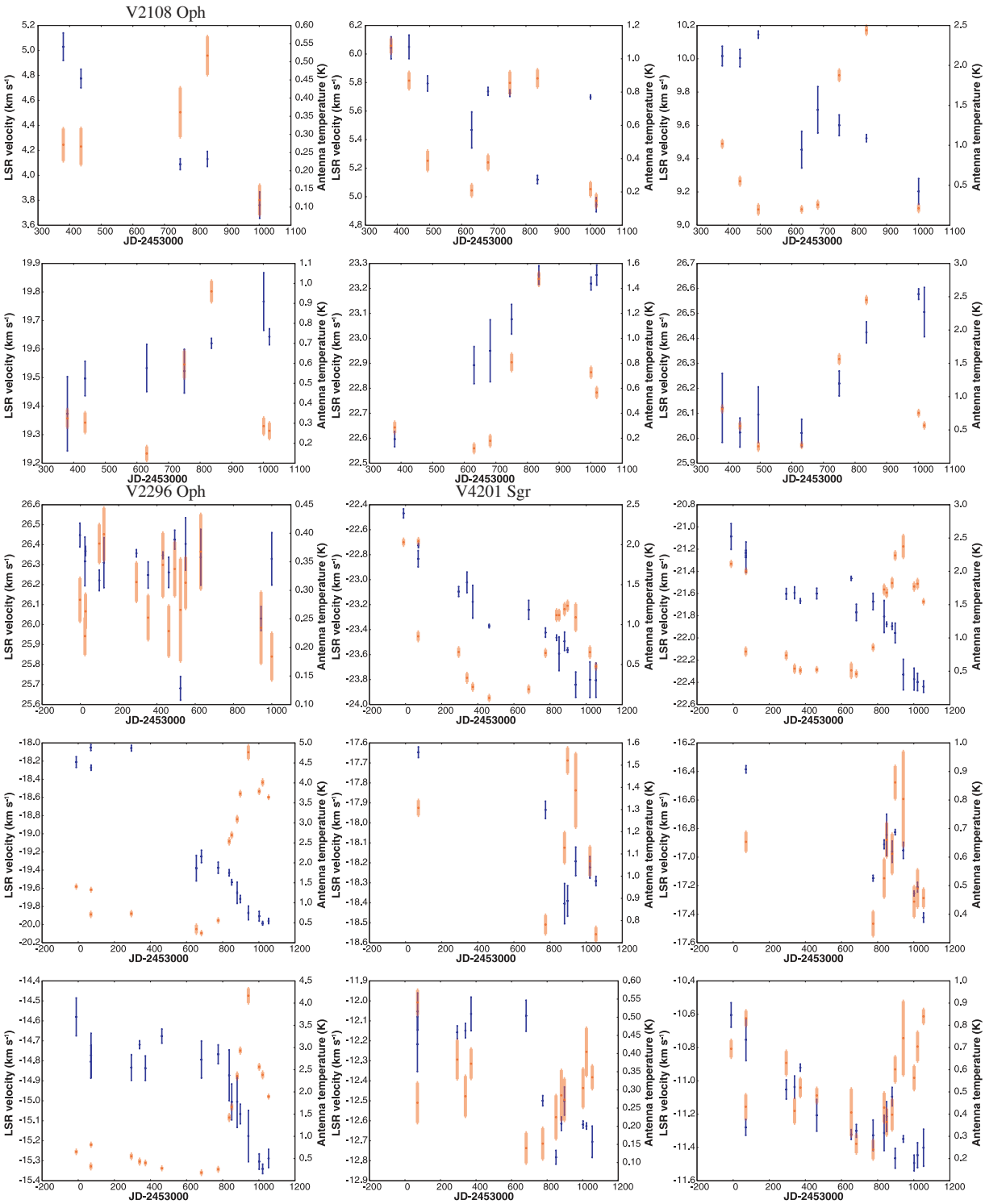

Fig. 8. (Continued)

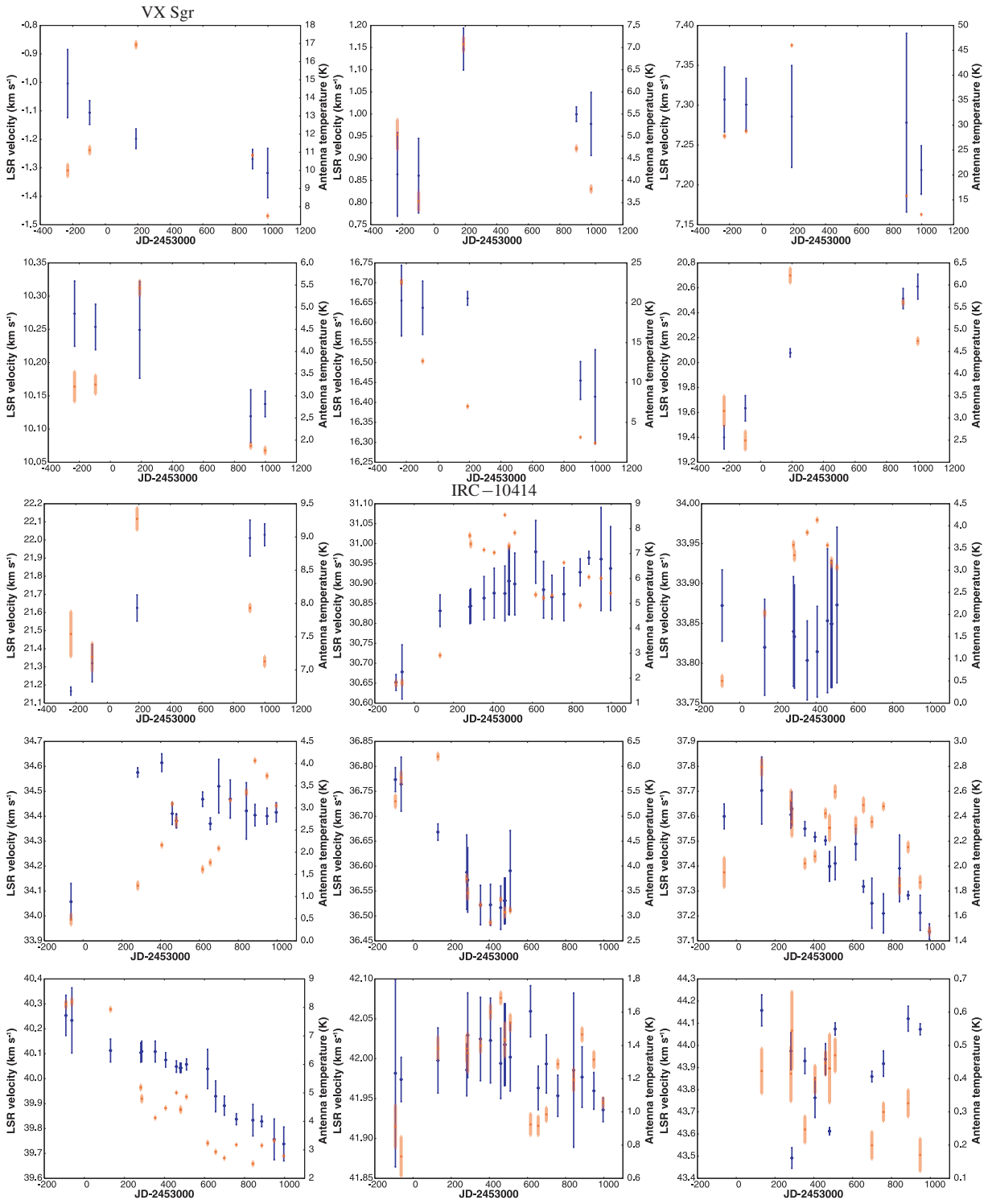

Fig. 8. (Continued)

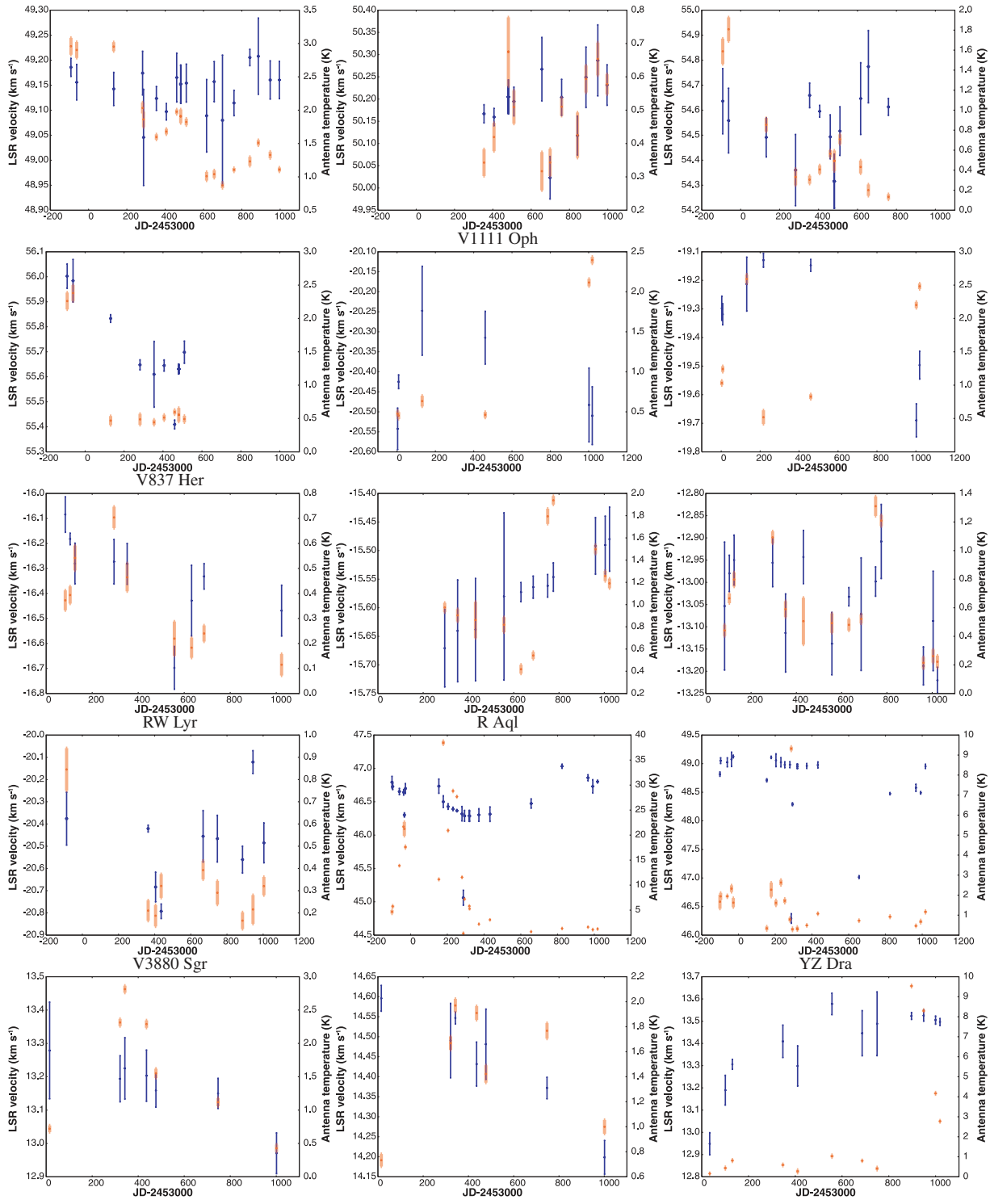

Fig. 8. (Continued)

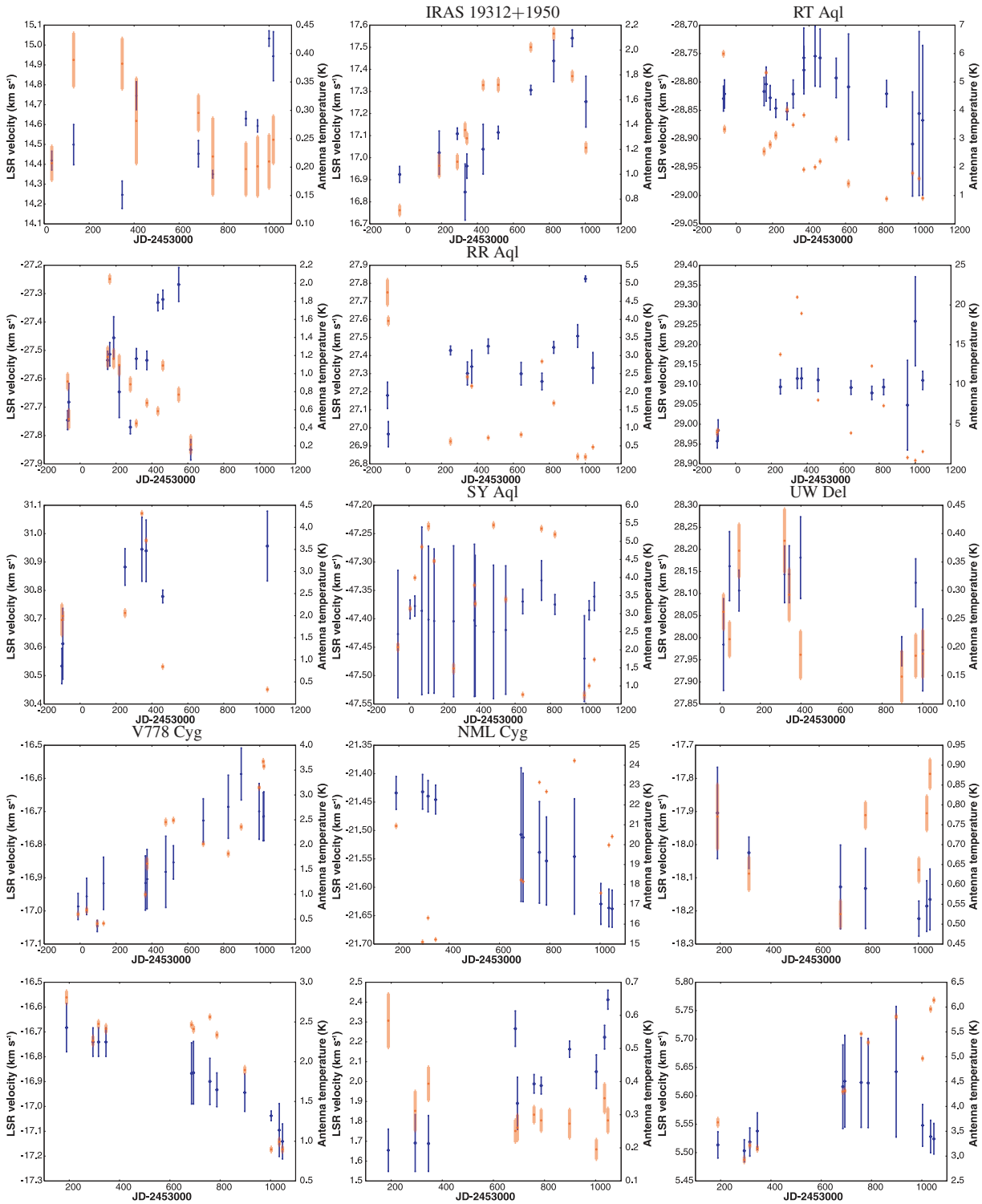

Fig. 8. (Continued)

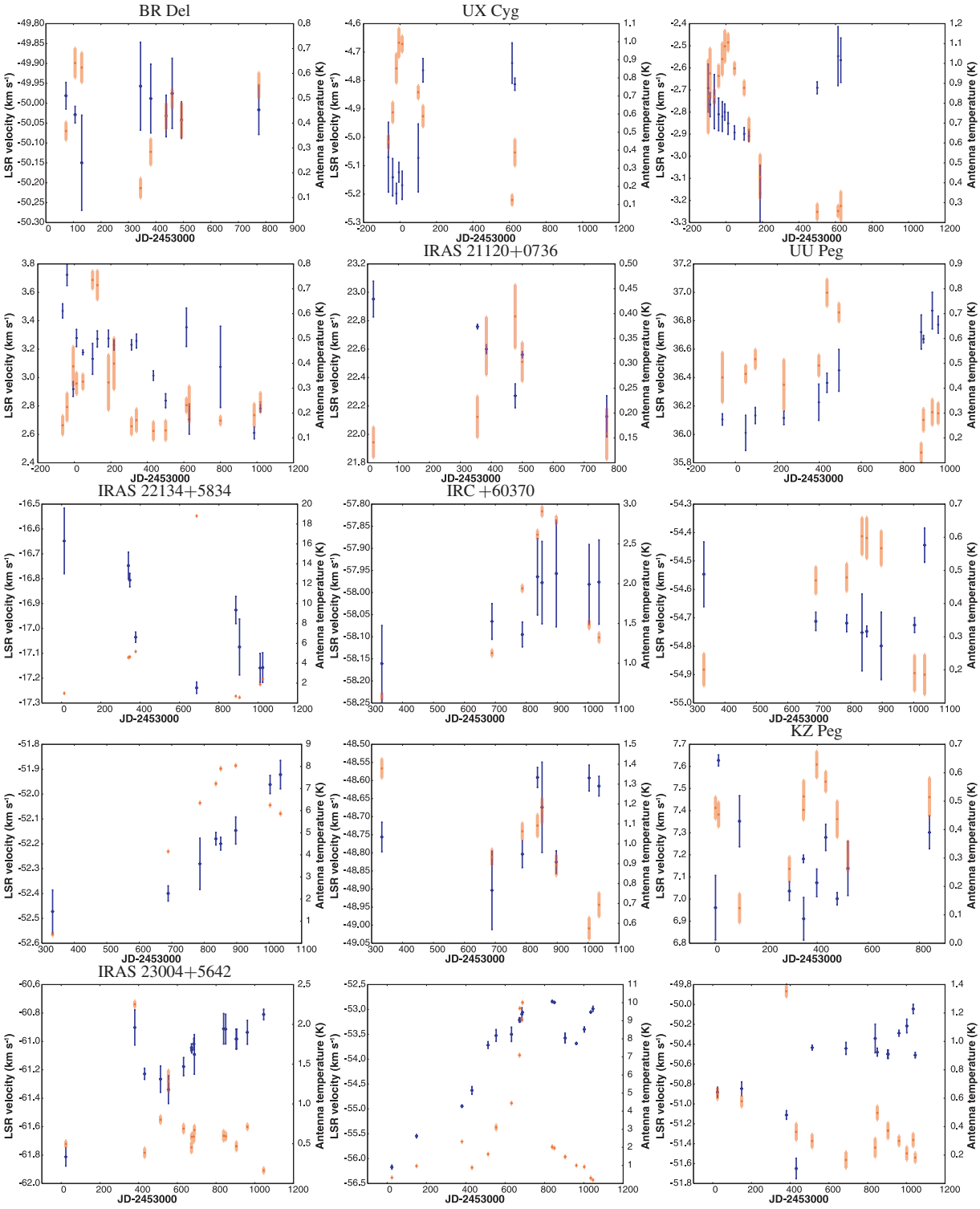

Fig. 8. (Continued)

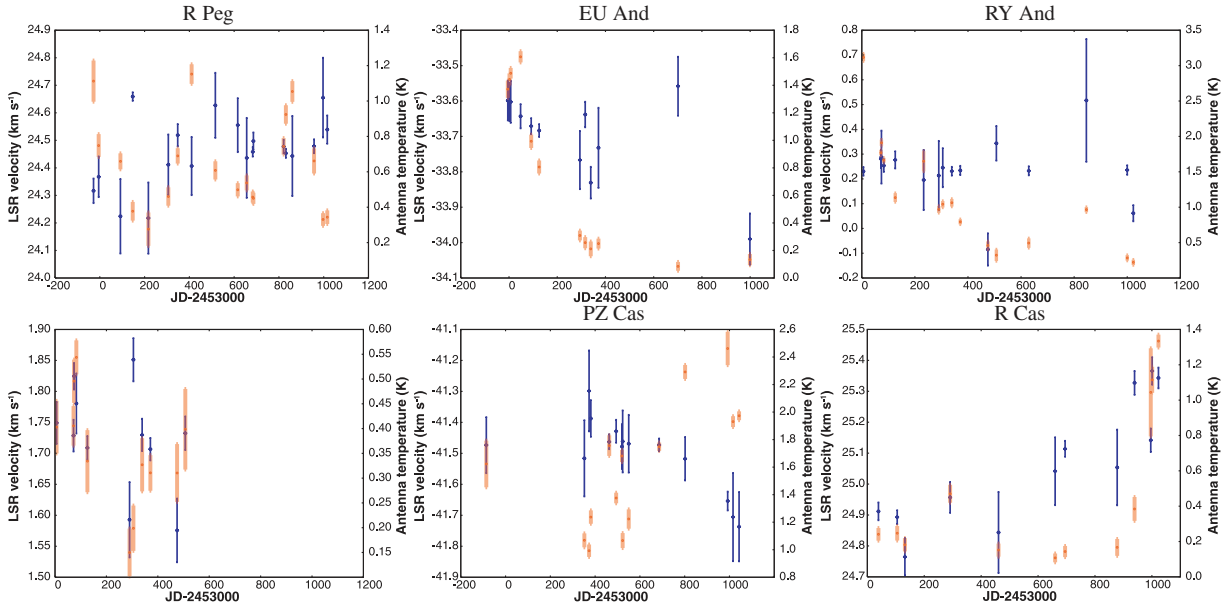

Fig. 8. (Continued)

S Crt

It was difficult to find any periodic variation in the H_2O maser flux. The brightest feature at $V_{LSR} \simeq 34.5\,km\,s^{-1}$ was the target of a measurement of the annual parallax with VERA ($\pi = 2.33 \pm 0.13$ mas and its corresponding distance of $D = 430^{+25}_{-23}$ pc, Nakagawa et al. 2008).

RT Vir

Rich maser emission peaks have been found in the velocity range $10\,km\,s^{-1} \leq V_{LSR} \leq 24\,km\,s^{-1}$, but which is slightly smaller than those previously reported. A periodic performance was found in the individual H_2O maser features with a period of ~ 300 d, rather than the adopted one (≈ 155 d). The 1612 MHz OH maser flux exhibits a periodic variation with two major periods of about 150 d and 300 d, which have small and large variation amplitudes, respectively (Etoka et al. 2003). For the case of the 1665 MHz and 1667 MHz maser fluxes, two periods of about 112 d and 170 d are found (Etoka et al. 2001). The spatio-kinematical structures of H_2O masers have been investigated in detail (Bowers et al. 1993; Bowers & Johnston 1994; Imai et al. 1997b; Bains et al. 2003; Imai et al. 2003) to show a spherically expanding gas shell with a small Doppler velocity gradient. Imai et al. (1997b) also found a systematic change in the distribution size of the maser features. Acceleration motions of the individual maser features have been found in the Doppler-velocity drifts and in the relative proper motions (Imai et al. 2003). The distance to RT Vir is estimated to be $D \simeq 220$ pc (Imai et al. 2003).

W Hya

The 1612 MHz OH maser flux exhibits a periodic variation with a period of about 330 d (Etoka et al. 2003). For the case of the 1665 MHz and 1667 MHz maser fluxes, a period of 362 d is found (Etoka et al. 2001). Although the H_2O maser emission is very bright and very close to the Sun ($D \approx 100$ pc, Vlemmings et al. 2003), the H_2O maser emission is completely resolved with VLBI baselines longer than 1000 km (Imai et al. 1997a). However, unpublished VERA data suggest the existence of compact maser features unresolved with the VERA baseline (2000 km).

S CrB

Because of the bright and stable H_2O maser emission, the maser source was believed to be one of the best targets for VERA astrometry. Unfortunately, the unpublished VERA data indicate that the maser emission is completely spatially resolved out with the VERA baselines. The distance to S CrB is estimated to be $D = 418^{+21}_{-18}$ pc (Vlemmings et al. 2003; Vlemmings & van Langevelde 2007).

U Her

A periodic variation of the maser flux has not been recognized as clearly as that found in optical emission. No clear velocity drift has been recognized. A single shell-shaped maser feature distribution was found (Bowers et al. 1993). Marvel (1997) observed these H_2O maser sources with the VLBA at three epochs, but no maser feature proper motion was reported. The distance to U Her is estimated to be $D = 266^{+32}_{-28}$ pc (Vlemmings et al. 2003; Vlemmings & van Langevelde 2007).

VX Sgr

The H_2O maser emission is bright enough to make a clear maser light curve, but no phase-reference source has been found around the maser source. Therefore, we have not monitored the maser source very tightly. A bipolar outflow has been identified in the envelope (Richards et al. 1996; Marvel 1997; Murakawa et al. 2003; Kamohara 2005).

IRAS 18176−1848 (OH 12.8−1.9)

H_2O maser emission has been detected for 20 years (Boboltz & Marvel 2005 and references therein). This H_2O maser source is recognized as being one of the "water fountain" sources (Boboltz & Marvel 2007). The H_2O maser emission is too weak to detect with the VERA 20 m telescope with the limited integration time.

IRC −10414

Rich maser spectral peaks have been found in the velocity range $30\,\mathrm{km\,s^{-1}} \leq V_{\mathrm{LSR}} \leq 57\,\mathrm{km\,s^{-1}}$. It is difficult to find any periodicy in the maser flux variation with a roughly constant decrease. Maeda et al. (2008) have found a bipolar outflow in the spatiokinematical structure of the H_2O masers, and estimated the distance to IRC −10414, in the statistical parallax method, to be $D \approx 2$ kpc, rather than the 700 pc previously adopted.

IRAS 18450−0148 (W 43 A)

This H_2O maser source is a prototype of the "water fountain" class , which has high-velocity components ($V_{\mathrm{exp}} \gtrsim 90\,\mathrm{km\,s^{-1}}$, Imai et al. 2002). It has been difficult to cover the whole LSR velocity range of the maser emission, and to make tight monitoring observations.

IRAS 19134+2131

This H_2O maser source is also one of the "water fountain" sources. In an annual parallax measurement, Imai, Sahai, and Morris (2007) estimated the distance to IRAS 19134+2131 to be $D = 8.0^{+0.9}_{-0.7}$ kpc. The H_2O maser emission is too weak to clearly find its light curve.

RR Aql

A periodic variation of the maser flux has been clearly recognized, although the number of observations is not so sufficient. The phase lag derived in the present paper ($\Delta\phi \sim 0.2$) is consistent with those previously derived ($\Delta\phi = 0.2$–0.5, Rudnitskii et al. 1999), but we expect that it may be larger by a pulsation cycle. The periodic variation of the maser feature distribution was also recognized (Bowers & Johnston 1994). The distance to RR Aql is estimated to be $D = 633^{+214}_{-128}$ pc (Vlemmings et al. 2003; Vlemmings & van Langevelde 2007).

UX Cyg

A periodic variation in the maser flux has been clearly recognized in the present work. With the annual-parallax method using the VLBA, Kurayama, Sasao, and Kobayashi (2005) measured the distance to UX Cyg; $D = 1.85^{+0.25}_{-0.19}$ kpc.

IRAS 22480+6002 (IRC +60370)

It is still difficult to recognize any periodic variation in the maser flux. The host star harboring the maser emission is expected to be an RV Tau variable (Imai et al. 2008).

R Cas

Although the weak maser emission frequently disappears, its periodic appearance is recognized. The long-term monitoring observations by Rudnitskij et al. (2000) have revealed that the phase lag has changed in the range $\Delta\phi = 0.2$–0.3, which is inconsistent with that found in the present result ($\Delta\phi \sim 0.1$). However, the relative difference between the results with respect to the pulsation period is reduced if we adopt possible phase lags of $\Delta\phi = 1.2$–1.3 and $\Delta\phi \sim 1.1$, respectively.

References

Alcolea, J., et al. 1999, A&AS, 139, 461
Asaki, Y., Deguchi, S., Imai, H., Hachisuka, K., Miyoshi, M., & Honma, M. 2007, in IAU Symp. 242, ed. J. Chapman, & W. Baan, 378
Bains, I., Cohen, R. J., Louridas, A., Richards, A. M. S., Rosa-González, D., & Yates, J. A. 2003, MNRAS, 342, 8
Benson, P. J., Little-Marenin, I. R., Woods, T. C., Attridge, J. M., Blais, K. A., Rudolph, D. B., Rubiera, M. E., & Keefe, H. L. 1990, ApJS, 74, 911
Berulis, I. I., Lekht, E. E., Munitsyn, V. A., & Rudnitskij, G. M. 1998, Astron. Rep., 42, 346
Berulis, I. I., Lekht, E. E., & Pashchenko, M. I. 1994, Astron. Lett., 20, 115
Boboltz, D. A., & Marvel, K. B. 2005, ApJ, 627, L45
Boboltz, D. A., & Marvel, K. B. 2007, ApJ, 665, 680
Bowers, P. F., Claussen, M. J., & Johnston, K. J. 1993, AJ, 105, 284
Bowers, P. F., & Johnston, K. J. 1994, ApJS, 92, 189
Brand, J., et al. 1994, A&AS, 103, 541
Bujarrabal, V., Gómez-Gonzárez, J., & Planeas, P. 1989, A&A, 219, 256
Chapman, J. M., & Cohen, R. J. 1986, MNRAS, 220, 513
Choi, Y. K., et al. 2008, PASJ, 60, 1007
Comoretto, G., et al. 1990, A&AS, 84, 179
Cooke, B., & Elitzur, M. 1985, ApJ, 295, 175
Diamond, P. J., & Kemball, A. J. 2003, ApJ, 599, 1372
Elitzur, M. 1992a, in Astrophysical Masers, ed. A. W. Clegg & G. E. Nedoluha (Berlin: Springer), 33
Elitzur, M. 1992b, ARA&A, 30, 75
Elitzur, M., Ivezić, Ž., & Vinković, D. 2003, in Mass-Losing Pulsating Stars and Their Circumstellar Matter, ed. Y. Nakada, M. Honma, & M. Seki (Dordrecht: Kluwer), 265
Esipov, V. F., Pashchenko, M. I., Rudnitskii, G. M., & Fomin, S. V. 1999, Astron. Lett., 25, 672
Etoka, S., Blaszkiewicz, L., Szymczak, M., & Le Squeren, A. M. 2001, A&A, 378, 522
Etoka, S., Le Squeren, A. M., & Gerard, E. 2003, A&A, 403, L51
Herman, J., & Habing, H. J. 1985, A&AS, 59, 523
Hjalmarson, Å., & Olofsson, H. 1979, ApJ, 234, L199
Höfner, S., Feuchtinger, M. U., & Dorfi, E. A. 1995, A&A, 297, 815
Höfner, S., Jørgensen, U. G., Loidl, R., & Aringer, B. 1998, A&A, 340, 497
Iguchi, S., Kurayama, T., Kawaguchi, N., & Kawakami, K. 2005, PASJ, 57, 259
Imai, H., et al. 1997a, A&A, 317, L67
Imai, H., et al. 1997b, A&A, 319, L1
Imai, H., et al. 2003, ApJ, 590, 460
Imai, H., Fujii, T., Omodaka, T., & Deguchi, S. 2008, PASJ, 60, 55

Imai, H., Obara, K., Diamond, P. J., Omodaka, T., & Sasao, T. 2002, Nature, 417, 829
Imai, H., Sahai, R., & Morris, M. 2007, ApJ, 669, 424
Inomata, N., Imai, H., & Omodaka, T. 2007, PASJ, 59, 799
Ishitsuka, J. K., et al. 2001, PASJ, 53, 1231
Ita, Y., et al. 2004, MNRAS, 347, 720
Kamohara, R. 2005, Ph.D. thesis, Kagoshima University
Kholopov, P. N., Samus, N. N., Durlevich, O. V., Kazarovets, E. V., Kireeva, N. N., & Tsvetkova, T. M. 1992, General catalogue of variable stars, fourth edition, Bull. Inf. Centre Donnees Stellaires, 40, 15
Kholopov, P. N., Samus, N. N., Kazarovets, F. V., & Perova, N. B. 1985–1988, Genral Catalogue of Variable Stars, 4th ed. (Moscow: Nauka Publishing House)
Kurayama, T., Sasao, T., & Kobayashi, H. 2005, ApJ, 627, L49
Lane, A. P. 1982, Ph.D. Thesis, University of Massachusetts
Lane, A. P., Johnston, K. J., Bowes, P. F., Spencer, J. H., & Diamond, P. J. 1987, ApJ, 323, 756
Le Bertre, T. 1993, A&AS, 97, 729
Lekht, E. E., Mendoza-Torres, J. E., Pashchenko, M. I., & Berulis, I. I. 1999, A&A, 343, 241
Lekht, E. E., Mendoza-Torres, J. E., Rudnitskij, G. M., & Tolmachev, A. M. 2001, A&A, 376, 928
Lekht, E. E., Rudnitskij, G. M., Mendoza-Torres, J. E., & Tolmachev, A. M. 2005, A&A, 437, 127
Maeda, T., et al. 2008, PASJ, 60, 1057
Marvel, K. B. 1997, PASP, 109, 1286
Mendoza-Torres, J. E., Lekht, E. E., Berulis, I. I., & Pashchenko, M. I. 1997, A&AS, 126, 257
Miranda, L. F., Gómez, Y., Anglada, G., & Torrelles, J. M. 2001, Nature, 414, 284
Murakawa, K., Yates, J. A., Richards, A. M. S., & Cohen, R. J. 2003, MNRAS, 344, 1
Nakagawa, A., et al. 2008, PASJ, 60, 1013
Nyman, L. A., & Olofsson, H. 1986, A&A, 158, 67
Pardo, J. R., Alcolea, J., Bujarrabal, V., Colomer, F., del Romero, A., & de Vicente, P. 2004, A&A, 424, 145
Pashchenko, M. I., & Rudnitskiĭ, G. M. 2004, Astron. Rep., 48, 380
Pashchenko, M. I., & Rudnitskii, G. M. 1999, Astron. Rep., 43, 311
Reid, M. J., & Moran, J. M. 1981, ARA&A, 19, 231
Richards, A. M. S., et al. 2004, in Proc. of the 7th European VLBI Network Symposium, ed. R. B. Bachiller, F. C. Colomer, J. F. Desmurs & P. de Vicente (Alcalá de Henares: Observatorio Astronómico Nacional), 209
Richards, A. M. S., & Yates J. A. 1998, Ir. Astron. J., 25, 7
Richards, A. M. S., Yates J. A., & Cohen, R. J. 1996, MNRAS, 282, 665
Rudnitskii, G. M., Lekht, E. E., & Berulis, I. I. 1999, Astron. Lett., 25, 398
Rudnitskiĭ, G. M., & Pashchenko, M. I. 2005, Astron. Lett., 31, 760
Rudnitskij, G. M., Lekht, E. E., Mendoza-Torres, J. E., Pashchenko, M. I., & Berulis, I. I. 2000, A&AS, 146, 385
Sjouwerman, L. O., Habing, H. J., Lindqvist, M., van Langevelde, H. J., & Winnberg, A. 2000, ESA SP 445, 519
Sudou, H., Omodaka, T., Imai, H., Sasao, T., Takaba, H., Nishio, M., Hasegawa, W., & Nakajima, J. 2002, PASJ, 54, 757
Takaba, H., Iwata, T., Miyaji, T., & Deguchi, S. 2001, PASJ, 53, 517
Takaba, H., Ukita, N., Miyaji, T., & Miyoshi, M. 1994, PASJ, 46, 629
Valdettaro, R., et al. 2001, A&A, 368, 845
van der Veen, W. E. C. J., & Habing, H. J. 1988, A&A, 194, 125
van Langevelde, H. J., van der Heiden, R., & van Schooneveld, C. 1990, A&A, 239, 193
Vlemmings, W. H. T., van Langevelde, H. J. 2007, A&A, 472, 547
Vlemmings, W. H. T., van Langevelde, H. J., Diamond, P. J., Habing, H. J., & Schilizzi, R. T. 2003, A&A, 407, 213
Yates, J. A., & Cohen, R. J. 1994, MNRAS, 270, 958